

Stellingen

behorende bij het proefschrift

Statics and Dynamics of a Natural Circulation Cooled Boiling Water Reactor

1. Hoewel de gemeten frequentieafhankelijke snelheid van verstoringen, zoals bepaald uit het faseverloop van het kruisspectrum van de signalen van twee neutronendetectors die zich in de kern van een kokend-waterreactor nabij de twee-fasenstroming bevinden, *wiskundig* te schrijven is als een gewogen gemiddelde van de plaatsafhankelijke voortplantingssnelheid van de verstoringen, is deze snelheid *fysisch* gezien geen gewogen gemiddelde.

Lübbesmeyer D. (1983) *Ann. Nucl. Energy* **10**, 421-432
Haghighat A. en Kosály G. (1989) *Nucl. Sci. Engng* **101**, 8-25

2. De door Beck en Płaskowski gegeven uitdrukking voor de systematische fout in de met de kruiscorrelatiemethode gemeten voortplantingstijd van temperatuurfluctuaties tussen twee thermokoppels ten gevolge van een verschil in tijdconstante van de thermokoppels onderschat deze fout met een factor zes.

Beck M.S. en Płaskowski A. (1987) *Cross correlation flowmeters - their design and application*, Adam Hilger, Bristol, Engeland

3. *Flashing* is een belangrijk verschijnsel in de eerste fase van het opstarten van door natuurlijke circulatie gekoelde kokend-waterreactoren.
4. Bij het modelleren en het simuleren van het gedrag van kernreactoren ligt de grootste onzekerheid bij de thermohydraulica. Verdere verschuiving van het onderzoek aan kernreactoren van de neutronica naar de thermohydraulica is derhalve wenselijk.
5. Het beoordelen van schone technologie op grond van korte-termijn economie (betaalbaarheid) is kortzichtig.

6. Het godsdienstonderwijs op de Nederlandse middelbare scholen is te veel op het christendom gericht.
7. Met meerkeuzevraagstukken wordt niet zozeer de kennis van de geëxamineerde getest, als wel de mate van overeenkomst van de denkwijzen van de geëxamineerde en van de opsteller van de vragen.
8. Slechts (56 ± 10) % van de Delftse stellingen voldoet aan de omschrijving: "niet op het onderwerp betrekking hebbende, wetenschappelijk verantwoorde en verdedigbare stelling".

College van Dekanen (1989) *Promotiereglement*, Technische Universiteit Delft, artikel 5.2

9. De bijdrage van het elektrisch vermogen dat door middel van kernenergie wordt opgewekt aan het totale in Nederland opgewekte elektrisch vermogen moet worden vergroot.
10. Vragen over het leven zijn als differentiaalvergelijkingen zonder randvoorwaarden.

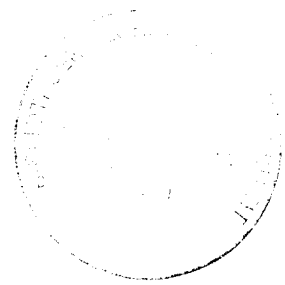
Armand J.C. Stekelenburg, 21 februari 1994

6000
3170000
TR 2337

**TR diss
2337**

Statics and Dynamics of a Natural Circulation Cooled Boiling Water Reactor

Armand J.C. Stekelenburg



Interfaculty Reactor Institute
Delft University of Technology
February 1994

CIP-GEGEVENS KONINKLIJKE BIBLIOTHEEK, DEN HAAG

Stekelenburg, Armand Jean Christian

Statics and Dynamics of a Natural Circulation Cooled Boiling Water Reactor /
Armand Jean Christian Stekelenburg. - Delft: Interfaculty Reactor Institute,
Delft University of Technology. - Thesis Delft University of Technology. - 111.
With ref. - With summary in Dutch.

ISBN 90-73861-19-5

NUGI 812

Subject headings: boiling water reactors / natural circulation

Copyright © 1994 by A.J.C. Stekelenburg

Statics and Dynamics of a Natural Circulation Cooled Boiling Water Reactor

PROEFSCHRIFT

ter verkrijging van de graad van doctor
aan de Technische Universiteit Delft,
op gezag van de Rector Magnificus Prof.Ir. K.F. Wakker,
in het openbaar te verdedigen ten overstaan van een commissie,
door het College van Dekanen aangewezen,
op maandag 21 februari 1994 te 16.00 uur
door

Armand Jean Christian STEKELENBURG

natuurkundig ingenieur
geboren te Bergen op Zoom

Dit proefschrift is goedgekeurd door de promotor:
Prof.Dr.Ir. H. van Dam

en de toegevoegd promotor: Dr.Ir. J.E. Hoogenboom



*Bear began to sigh, and then found he
couldn't because he was so tightly stuck;
and a tear rolled down his eye, as he
said: "Then would you read a Sustaining
Book, such as would help and comfort a
Wedged Bear in Great Tightness?"*

A.A. Milne, *Winnie-The-Pooh*,
Penguin Books USA Inc., New York, 1988



The research described in this thesis was performed at the Reactor Physics Department of the Interfaculty Reactor Institute, Delft University of Technology, Mekelweg 15, NL-2629 JB Delft, The Netherlands

Contents

| | |
|---|----|
| 1. Introduction | 11 |
| Natural circulation cooled boiling water reactors | 11 |
| Research on statics and dynamics | 12 |
| Scope of this study | 13 |
| The Dodewaard reactor | 15 |
| Downcomer thermocouple noise and circulation flow rate measurements | 19 |
| 2. Coolant flow rate estimation - downcomer thermocouple transit time measurements | 25 |
| Introduction | 25 |
| Transit time estimation | 26 |
| Theory | 26 |
| Example | 28 |
| Practical aspects | 29 |
| Downcomer thermocouple transit time measurements | 29 |
| Theoretical prediction and measurement of the standard deviation | 29 |
| Results of averaged transit time measurements | 32 |
| Conclusions | 33 |
| 3. Coolant flow rate estimation - numerical simulation of the downcomer flow | 35 |
| Introduction | 35 |
| Fundamentals of the computer program | 36 |
| The geometry of the downcomer channel | 37 |
| Three-dimensional calculations | 38 |
| Set-up | 38 |
| Reliability | 39 |
| Results | 41 |
| Two-dimensional calculations | 42 |
| Steady state flow | 42 |
| Simulation of transient flow | 45 |
| Validation | 49 |
| Synthesis of two- and three-dimensional calculations | 50 |
| Conclusions | 51 |

| | |
|---|-----------|
| 4. Two-phase flow monitoring by analysis of in-core detector noise signals | 53 |
| Introduction | 53 |
| Two-phase flow induced in-core detector noise | 54 |
| The response of an in-core detector to density fluctuations | 54 |
| Fluctuations in two-phase flow | 59 |
| Two-phase flow monitoring | 63 |
| Velocity measurements | 63 |
| Other techniques for monitoring two-phase flow | 65 |
| Example: distribution of the in-core neutron detector noise | 66 |
| Conclusions | 70 |
| | |
| 5. A theoretical model for the reactor dynamics | 73 |
| Introduction | 73 |
| Theoretical model | 74 |
| Introduction | 74 |
| Neutron kinetics | 76 |
| Fuel temperature dynamics | 78 |
| Lower part of the core with single-phase flow | 80 |
| Part of the core with two-phase flow | 80 |
| Riser | 83 |
| Upper plenum - carry under | 83 |
| Downcomer channel above the feedwater sparger | 85 |
| Condensation and mixing at the sparger level | 87 |
| Downcomer channel and lower plenum enthalpy transport | 87 |
| Vessel steam and water content | 88 |
| Water level | 89 |
| Pressure | 89 |
| Equation of motion of the circulation flow | 91 |
| Steam and feedwater flow rate | 91 |
| Model parameters | 92 |
| Model implementation | 98 |
| Initial conditions | 98 |
| Solving the differential equations numerically | 99 |
| The simulator program | 100 |
| Concluding remarks | 100 |

| | |
|---|------------|
| 6. Measurement and simulation of stationary reactor conditions | 101 |
| Introduction | 101 |
| Variation of power | 103 |
| Measurements and simulations | 103 |
| Discussion | 105 |
| Variation of feedwater temperature | 108 |
| Introduction | 108 |
| Simulation at fixed power | 108 |
| Simulation at fixed base reactivity | 110 |
| Variation of water level | 113 |
| Measurements and simulations | 113 |
| Discussion | 114 |
| Influence of pressure, power and feedwater temperature | 115 |
| Variation of pressure | 116 |
| Measurements and simulations | 116 |
| Discussion | 118 |
| Simulation at higher pressure, and with altered model parameters | 121 |
| System behaviour without carry under | 123 |
| Concluding remarks | 124 |
| | |
| 7. Measurement and simulation of reactor dynamics | 125 |
| Introduction | 125 |
| Transient behaviour near full-power conditions | 126 |
| Short-term response to a reactivity step | 126 |
| Steam flow valve step response | 128 |
| Long-term response to a reactivity step | 131 |
| Feedwater transients | 134 |
| Concluding remarks | 136 |
| System dynamics without carry under | 138 |
| Dynamics at low power and low pressure | 138 |
| Introduction | 138 |
| Measurements | 139 |
| Simulations | 140 |
| Concluding remarks | 142 |
| | |
| General conclusions and recommendations for future research | 143 |
| | |
| Appendix | |
| Measurements on the Dodewaard natural circulation cooled BWR | 147 |
| Measurement techniques | 147 |
| Noise measurements | 147 |
| List of measurements | 148 |

| | |
|-----------------------------------|-----|
| Summary | 149 |
| Samenvatting | 151 |
| Nomenclature | 153 |
| List of symbols | 153 |
| Superscripts | 155 |
| Subscripts | 155 |
| Operators | 157 |
| List of abbreviations | 157 |
| References | 159 |
| Dankwoord | 167 |
| Curriculum vitae | 169 |

chapter 1

Introduction

Natural circulation cooled boiling water reactors

Passivity (the ability to operate without reliance on external power sources) and *simplicity* can enhance safety. For the last decade, this has been one of the key thoughts behind the design of nuclear reactors (Van Dam, 1992).

Natural circulation of the coolant flow perfectly fits this concept. For this reason, many of the so-called advanced reactors rely on natural circulation (or convection) for the cooling of heat sources. This is strongly the case in General Electric's Simplified Boiling Water Reactor design (SBWR; McCandless and Redding, 1989), in which the core is cooled by a natural circulation coolant flow instead of a pump driven coolant flow (see, for instance, Lahey and Moody (1977) for detailed information on boiling water reactors). The Dodewaard boiling water reactor (The Netherlands) is another example in which natural circulation is applied for the cooling of the core.

The first boiling water reactor (BWR), BORAX-I (BOiling ReActor eXperiments), that was operated in 1953-1954, was a natural circulation cooled BWR (Kramer, 1958; Cohen and Zebroski, 1959). This experimental reactor showed that the BWR-concept was feasible. As this concept was attractive due to its basic simplicity, potential for higher thermal efficiency, better reliability and lower capital cost than other light water reactor systems, BORAX-I was followed by other experimental BWRs, like BORAX-II,III,IV, EBWR (Experimental Boiling Water Reactor), VBWR (Vallecitos Boiling Water Reactor), and SPERT (Special Power Excursion Reactor Test) (Kramer, 1958; Cohen and Zebroski, 1959). Some of these reactors featured forced circulation of the core coolant flow. It was observed that the forced circulation cooled BWRs were more

stable than the natural circulation cooled BWRs, due to the potential for a higher coolant flow rate in a forced circulation reactor. With the economic need for increasing the power density of the reactors, by the mid sixties, forced circulation designs were preferred to natural circulation designs. The Dodewaard reactor is one of the exceptions to the trend of the increase in the power density.

Nowadays, the natural circulation cooling concept of BWRs shows a revival. In the West, General Electric has the SBWR-design. In the former USSR, in addition to the already existing small natural circulation cooled BWRs, the construction of reactors with scaled-up reactor power is expected (Dolgov *et al.*, 1990). The Dodewaard reactor is the only operating western BWR which bridges the gap between the early-day natural circulation cooled BWRs and the modern advanced natural circulation cooled BWR designs.

Research on statics and dynamics

In text-books on BWRs, studies on both steady state operation as well as transient behaviour of BWRs are presented (see, for instance, Kramer, 1958; Lahey and Moody, 1977). In scientific journals nearly all papers on BWRs concern system dynamics. This phenomenon probably originates from the general belief in the late forties that BWRs would not be stable.

From the earliest models of BWR dynamics, much effort is put into the investigation of the purely thermal hydraulic density wave instability (see, for instance Bouré *et al.* (1973) for a review of studies on two-phase flow instabilities). Soon after the introduction of the thermal hydraulic models, neutron kinetics was incorporated in order to study the behaviour of the coupled thermal hydraulic-neutronic system. It was found that the compound system can become unstable at a frequency close to the resonance frequency of the density wave oscillation (typically 0.3-1 Hz). Much effort has been put into the development of sophisticated models and computer codes for performing stability analysis of BWRs. Tools were developed for monitoring the stability and for system identification (Kitamura *et al.*, 1977; Matsubara *et al.*, 1978; Upadhyaya and Kitamura, 1981; Mitsutake *et al.*, 1984; Kanemoto *et al.*, 1984; March-Leuba and King, 1988; Van der Hagen, 1989).

The theoretical models of BWR dynamics can be classified according to (Neal and Zivi, 1967):

- *The degree of distribution of the model parameters.* With a high degree of distribution, the geometry of the problem is divided into nodes. The conservation laws are solved for each node separately. The model with the lowest degree of

distribution of the model parameters is the lumped parameter model, in which distributed variables are represented by a single effective quantity;

- *The method used to solve the model equations.* Physical problems can be modelled by differential equations in space-time. On the one hand, the model equations can be solved analytically or numerically in the time domain. On the other hand, the model equations can be linearized by splitting up the variables in their steady state values and their time varying part. The linearized equations can be Fourier-transformed. The problem can be analyzed in the frequency domain, or responses of the system can be calculated by performing an inverse Fourier transformation. The linearization method is only applicable for studying the dynamics in which small fluctuations are involved.

Complex computer codes, based on multi-node models, are used for simulating accidents. In order to investigate normal operation of a natural circulation cooled BWR, Miida and Suda (1963, 1964) constructed a frequency domain, lumped parameter model. With the model, step responses were calculated and transfer functions were analyzed. The model was used later for studying the noise sources in a BWR (see Suda (1985) for a review of Japanese studies on model based noise analysis).

For the Dodewaard reactor, Kleiss (1983) performed time series analysis of noise signals to study noise sources and transfer functions. Also, Kleiss (1983) performed measurements of control rod and steam flow control valve step responses. Similar experiments are reported later by Kleiss and Van der Hagen (1985a; Van der Hagen, 1986, 1989; Van der Hagen *et al.*, 1988b). Kleiss and Van Dam (1985b) drew up a frequency domain, lumped parameter model with which transfer functions were calculated.

Recently, the research on stationary conditions of the Dodewaard reactor was intensified. Measurements of several reactor parameters were performed at various operating conditions (see the appendix).

Scope of this study

Due to the strong interconnection of the various processes in the reactor vessel of a natural circulation cooled BWR, explaining the physics of both the statics and the dynamics of the Dodewaard reactor is not an easy task. In literature, little information can be found on the behaviour of natural circulation cooled BWRs. In this thesis, the physics is studied through a combined experimental and theoretical investigation. The experiments are analyzed further with the use of the model, and the results of the model calculations provide ideas for new experiments.

For an experimental study of the reactor behaviour, measurement tools are required. Many relevant process variables are supplied by the power plant's data-logger, but a direct method for measuring the circulation flow rate is not available. Termaat (1970) gives a method to measure the circulation flow rate indirectly from downcomer thermocouple noise signals. This method is outlined below and the research to improve the method is discussed in more detail in chapters 2 and 3.

No probes are available for measuring the in-core void fraction - a variable of importance for both the reactivity of the reactor as well as the circulation flow rate. The noise signals of in-core neutron and gamma detectors, however, contain information on the local in-core two-phase flow (Boyd, 1959). In chapter 4, a literature survey on two-phase flow monitoring with the use of in-core detector noise signals is presented. In this chapter also measurements of in-core neutron detector noise signals that demonstrate the relation between the two-phase flow conditions and the signal characteristics are discussed.

Reactor behaviour can be studied theoretically with the use of a complex computer code, based on a multi-node model. In this way, reliable results are obtained. In many cases, however, such a code is not easy to use, and the calculations require much computer time. Calculations based on a simple model have a lower reliability, but, as the model is clearer, provide more insight into the physics of the system.

For this reason, a simple theoretical dynamical model for the main physical processes of the Dodewaard natural circulation cooled BWR is presented in this thesis. The model is a time domain, lumped parameter model. As the interest lies in the interconnection of the processes in the reactor vessel, the model is developed for the simulation of slow transients. The steady state representation of the model equations is used for examining the stationary conditions of the reactor. In view of the simplicity of the model, the calculations do not provide an accurate simulation of the experiments, but the general trend and important effects are simulated correctly.

The theoretical model, the model parameters and the simulator program are presented in chapter 5. Stationary reactor conditions are analyzed in chapter 6, and transient behaviour is discussed in chapter 7. In these chapters, both measurements and simulations are presented, and the physics of the system is elaborated.

An introduction to the Dodewaard natural circulation cooled BWR is given below, followed by an explanation of the circulation flow measurement technique.

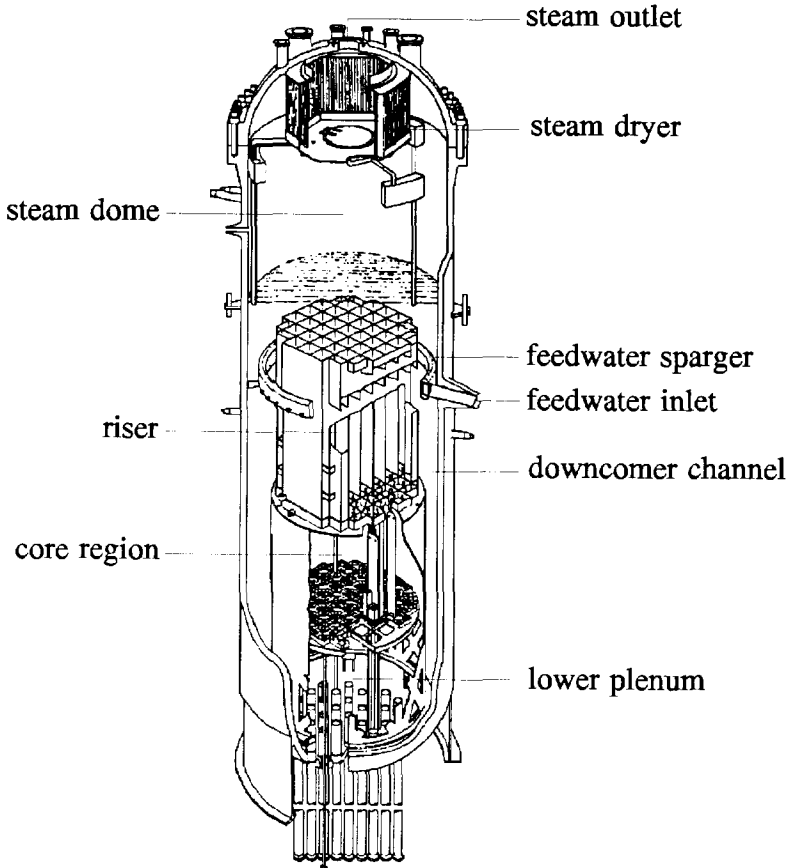


Figure 1-1. Cut-away view of the Dodewaard reactor vessel

The Dodewaard reactor

Figure 1 shows a cut-away view of the reactor vessel of the Dodewaard reactor and in Fig. 2 a cross-section of the reactor vessel is drawn. Table 1 lists the main characteristics of the full-power conditions.

Nuclear fissions take place in fuel rods with a diameter of 13.5 mm, that are arranged in a square lattice of 6×6 rods (one of the 36 rods is a so-called water rod filled with water in stead of fuel). The 6×6 array, with a shroud, forms a flow channel, called a fuel bundle. The core consists of 164 fuel bundles. The arrangement of the bundles approximately forms a cylinder, as shown in Fig. 3. The squares drawn in this figure are so-called control cells - a combination of a control rod surrounded by four

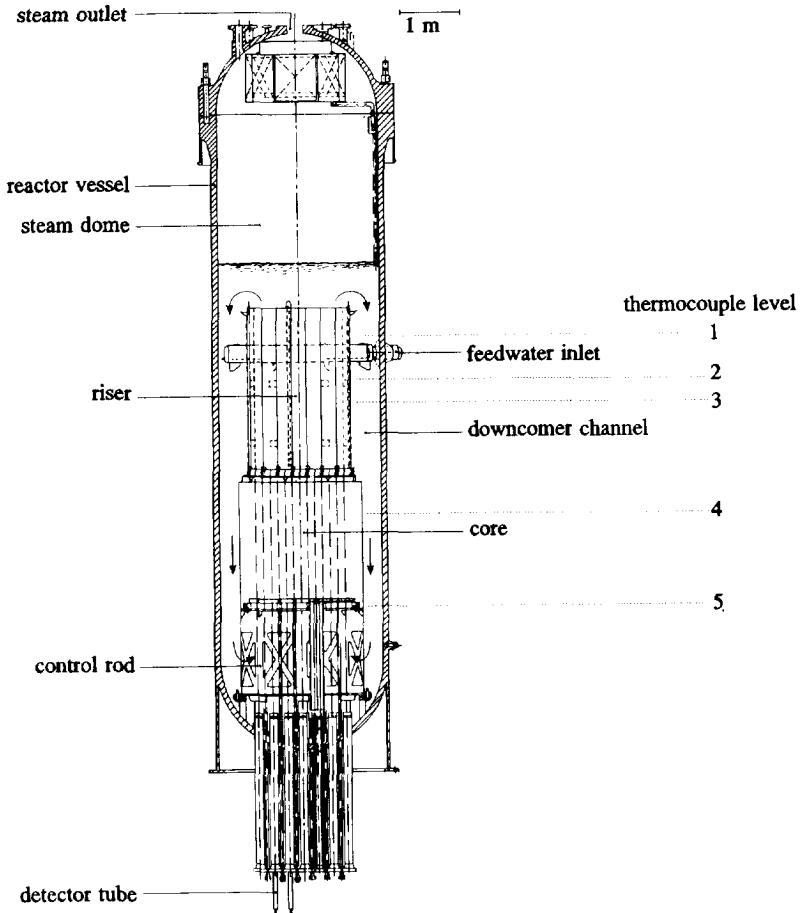


Figure 1-2. Cross-section of the Dodewaard reactor vessel

fuel bundles. The control cells are coded according to the number (1-7) and capital (A-G) indicating the position. The remaining 16 fuel bundles are not situated next to a control rod position. The reactivity of the reactor is controlled in coarse steps with the control rods. Fine-step reactivity control is performed by varying the water level (see chapter 6).

Water flows upwards through the fuel bundles. The water slows down the fast neutrons produced by the fission process (moderation), and transports heat from the fuel rods out of the core (coolant). This double role of the water is important, because a change in the power produced by the fission process changes the properties of the water, and thus of the moderator. This, in turn, affects the fission chain reaction, and

Table 1-1. Main characteristics of the full-power conditions of the Dodewaard reactor

| | |
|---|------------------------------------|
| electric power | 60 MW |
| thermal power | 183 MW |
| pressure | 75.5 bar |
| saturation temperature | 563 K |
| circulation flow rate | approx. 1300 kg/s |
| feedwater flow rate | 81 kg/s |
| feedwater temperature | 408 K |
| collapsed water level (at hot stand-by) | 55 cm above the top of the chimney |
| core-averaged outlet flow quality | approx. 8 % |
| core-averaged outlet void fraction | approx. 62 % |
| flow quality in the downcomer above the feedwater sparger | approx. 2 % |

consequently the power.

The water enters the core with a temperature below saturation temperature. Flowing upwards, the water heats up, and, at some level, boiling occurs - first sub-cooled boiling, followed by saturated boiling. As the water proceeds upwards, the flow quality and the void fraction increase. The two-phase mixture flows from the core through the riser into the upper plenum. Here, free surface steam separation takes place. Most of the steam flows through the steam dryer to the main steam line on top of the vessel. Most of the water turns around and flows into the downcomer channel next to the riser and the core. Some water flows into the steam dryer and is fed back into the upper plenum. Some steam is dragged into the downcomer channel. This effect is called carry under. Due to the carry under, a two-phase flow exists in the upper part of the downcomer channel. Arriving at the feedwater sparger, where strongly subcooled water is injected, the steam condenses and all the water is cooled down to a temperature of a few K below saturation temperature. The water travels through the remaining part of the downcomer channel next to the riser and next to the core, through the lower plenum, to the inlet of the core.

Usually in BWRs, no riser is installed, and the circulation of the water is driven by pumps. In the Dodewaard reactor, the circulation is driven by the density difference between the water/steam in the downcomer channel and the water/steam in the core and

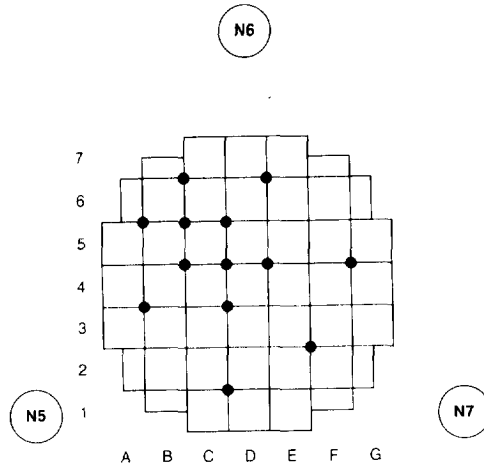


Figure 1-3. Cross-section of the Dodewaard core with the positions of the ex-vessel neutron detectors N5, N6, and N7, and the in-core detector positions (black dots)

the riser. The riser increases the driving force of the circulation flow.

The Dodewaard BWR is a so-called direct-cycle BWR (Lahey and Moody, 1977). The steam leaving the vessel is fed directly into the turbine. The steam from the turbine condenses in the condenser. The condensate is pre-heated, and pumped into the downcomer channel through the feedwater sparger.

For monitoring the axial and, in a limited sense, the radial neutron flux density distribution, instrument guide tubes are installed at some radial positions (see Fig. 3). These so-called TIP-tubes (TIP=Traversing In-core Probe) are coded according to the coordinates of control cell to the lower left of the TIP-tube. An average measure of the flux density is obtained from the ex-vessel neutron detectors. The plant is equipped with flow meters for measuring all in- and out-going flow rates of the vessel. Also, temperatures of the flows are measured. A device is installed for measuring the subcooling of the flow in the downcomer channel next to the core (Wouters *et al.*, 1992a). Thermocouples are installed in the downcomer channel. As explained below, these thermocouples can be used for estimating the circulation flow rate.

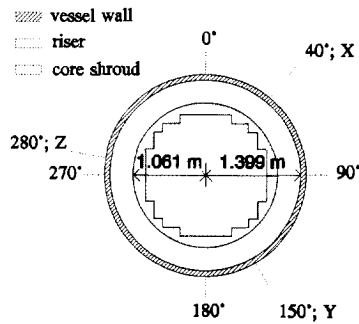


Figure 1-4. Top view of the reactor vessel with thermocouple angular positions X, Y and Z

Downcomer thermocouple noise and circulation flow rate measurements

Termaat (1970) describes a method to measure the circulation flow rate of the Dodewaard reactor. The method is based on the transportation of inherent fluctuations of the temperature of the downcomer flow. By correlating the signals of a down-stream and an up-stream thermocouple, the transit time of the fluctuation is estimated. The circulation flow rate is calculated from the transit time (see also Beck and Płaskowski, 1987). To put the method into practice, thermocouples were installed at five heights (coded 1-5; see Fig. 2), at three azimuthal angles (coded X, Y and Z; see Fig. 4), and at two distances from the vessel wall (coded A and B; see Fig. 5). Furthermore, at all positions, two thermocouples were installed with 5 cm axial displacement (code 1 and 2; see Fig. 5). The complete code of a thermocouple consists of the code for the distance to the vessel wall, followed by the code for the elevation, followed by the code for the up- or down-stream thermocouple, and, finally, followed by the code for the azimuthal angle. For instance: A41Y is the thermocouple closest to the vessel wall, at elevation 4, the upper thermocouple of the two, and at azimuthal angle 150°. At the date of this thesis, only nine of the original thermocouples function properly. The response time of the thermocouples is approximately 0.018 s (Termaat, 1970). The vertical instrument tubes have a horizontal cross-section of $6.35 \times 12.7 \text{ mm}^2$. The thermocouples protrude from the widest side of the instrument tubes 5 mm (Termaat, 1969).

For all (properly functioning) thermocouples, the voltage supplied lies between 9.3 mV and 9.6 mV. This implies that all thermocouples indicate the same temperature within 7.3 K (according to a sensitivity of $41 \mu\text{V/K}$; Termaat, 1970). The RMS-value

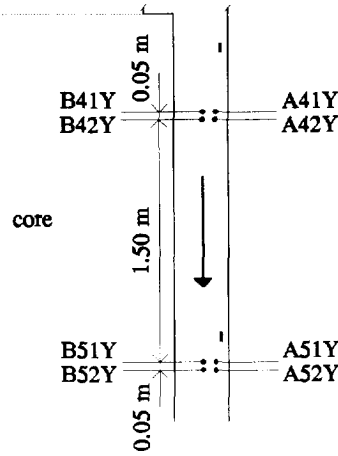


Figure 1-5. Thermocouples in the part of the downcomer channel next to the core

(Root Mean Square) of the noise signal of the thermocouples is approximately 0.4 K-0.9 K, and is lower for lower elevation: A31Y: 0.86 K, A41Y: 0.60 K, and A52Y: 0.48 K (Van der Hagen, 1991; Stekelenburg *et al.*, 1991).

The signals of thermocouples which are located at different angular position show a low coherence (< 0.04 ; see, for instance, Priestley (1981) for detailed information on noise analysis; see the appendix for the general procedure of the noise measurements performed at IRI). The auto-power spectral densities, however, show a strong resemblance. The signals of thermocouples at the same angular position show a much higher coherence. In Fig. 6, the cross-correlation functions and the auto- and cross-power spectral densities of the noise signals of thermocouples A31Y, A41Y and A52Y are plotted. The auto-spectra show that the signals are low-frequency signals. The auto-spectra drop to 10 % of their maximum value at approximately 1 Hz. The correlation of A31Y with A41Y and A52Y is low. The correlation between A41Y and A52Y is higher, and the correlation function shows a clear transit time behaviour (see chapter 2). These characteristics are also present in the frequency domain. The coherence functions of A31Y with A41Y and A52Y only show some coherence below 0.1 Hz. For signals A41Y and A52Y, however, the coherence is high up to 0.5 Hz. The phase between signal A31Y and A41Y or A52Y is non-linear at low frequency, and shows erratic behaviour at high frequency. Between A41Y and A52Y, the phase is linear, and only shows a minor increase in statistics. As the coherence is low for frequencies above 0.5 Hz, much time is required for an accurate estimation of the cross-power spectral

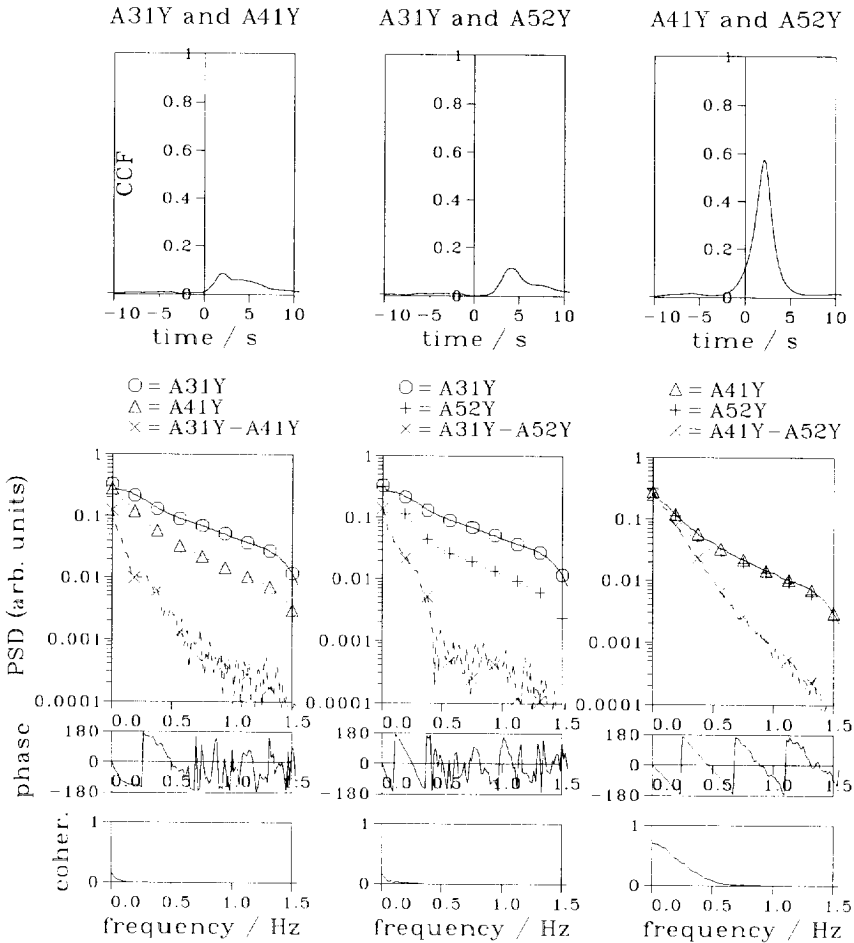


Figure 1-6. Characteristics of the noise signals of thermocouples A31Y, A41Y and A52Y

density (or the cross-correlation function). For this reason, the response time of the transit time estimation, which involves the cross-power spectral density or the cross-correlation function, is large.

Summarizing, it can be stated that only between A41Y and A52Y, which are the thermocouples next to the core, a clear transit time phenomenon is present. The signal of thermocouple A31Y, located high in the downcomer channel next to the riser, is weakly correlated with the signals of the thermocouples next to the core. This is due to the dissipation of the fluctuations on the path from the level 3 thermocouples to the

level 4 and 5 thermocouples. The dissipation on this path is greater than on the path from level 4 to level 5, because of the larger distance between level 3 and 4, the mixing of the flow due to the transition from the section of the downcomer channel next to the riser to the section next to the core, and the turbulence induced by the injection of the feedwater some 70 cm above thermocouple level 3. This explanation is supported by the results of the measurements of the RMS-value of thermocouples A31Y, A41Y and A52Y given above.

Possible sources of the inherent temperature fluctuations of the downcomer flow are:

- 1) fluctuations of the feedwater flow rate;
- 2) fluctuations of the feedwater temperature;
- 3) fluctuations of the saturation pressure and consequently the temperature;
- 4) fluctuations of the (local) circulation flow rate;
- 5) fluctuations of the (local) carry under.

As the feedwater is injected from the feedwater sparger (which is a ring in the downcomer channel between the riser and the vessel wall; see Figs. 1 and 2), the first two noise sources would result in a correlation between the signals of thermocouples from different angular positions, with a possible transit time. This correlation is not observed. Besides, the noise signal of the feedwater flow meter is only weakly correlated with the noise signals of the downcomer thermocouples. A similar argument applies for the third possible noise source. Downcomer thermocouple noise signals are only weakly correlated with the noise signal of the vessel pressure sensor.

Both of the last two remaining possible noise sources can be the result of the chaotic behaviour of the froth in the upper plenum. With respect to a discrimination between the two noise sources, the thermocouple transit time measurement technique cannot be used for measuring the local fluctuations of the flow rate, as the response time of the transit time measurements is too large. Possibly, a discrimination can be performed according to the correlation of the noise signal of A31Z, which is located at an angle of 280° (see Fig. 4), and the noise signal of the pressure difference transducer, DP1, which is located at an angle of 270° (GKN, 1965). With DP1, the density of the two-phase flow at the level of the feedwater sparger can be measured.

The RMS-value of the fluctuations of the circulation flow rate, or the downcomer steam flow, needed to result in a given RMS-value of the fluctuation of the downcomer temperature, can be calculated from the model of the specific downcomer enthalpy, presented in chapter 5, Eq. (5-49). At full power conditions, a 1 K fluctuation of the temperature of the downcomer flow is caused by a fluctuation of the circulation flow rate of 0.43 %, or a fluctuation of the downcomer gas flow rate of 12.5 %. Both these

values sound reasonable.

At the date of this thesis, A41Y and A52Y are the only functioning vertically displaced thermocouples next to the core. The method for measuring the circulation flow rate from the noise signals of these thermocouples involves two steps:

- 1) measurement of the transit time between A41Y and A52Y;
- 2) calculation of the circulation flow rate from the transit time.

In chapter 2, theoretical and practical aspects of transit time estimation are discussed. The circulation flow rate measurement technique is calibrated by simulating the transportation of a fluctuation of the temperature of the downcomer flow with FLUENT, a computer program for calculating turbulent flow in space-time (FLUENT, 1990; Colenbrander, 1991). This work is presented in chapter 3.

chapter 2

Coolant flow rate estimation - downcomer thermocouple transit time measurements¹

Introduction

As no flow meters are installed in the Dodewaard reactor vessel, the circulation flow rate cannot be measured directly. As presented in chapter 1, however, the downcomer thermocouples A41Y and A52Y can be used for indirectly measuring the circulation flow rate. The transit time between the noise signals of these two thermocouples can be estimated by applying noise analysis techniques. In this chapter theoretical and practical aspects of such a transit time estimation are discussed. The measured transit time is converted into a mass flow rate with the use of a calibration curve. The numerical fluid flow calculations, which were made to produce this calibration curve, are presented in chapter 3.

¹This chapter is an adapted version of:
Stekelenburg A.J.C., Van der Hagen T.H.J.J. and Nissen W.H.M. (1991) *The downcomer flow in a natural-circulation-cooled BWR*, proc. of *SMORN VI - A symposium on nuclear reactor surveillance and diagnostics* (ed. Kryter R.C. and Upadhyaya B.R.) 19-24 May, 1991, Gatlinburg, Tennessee, USA, 1, 37.01, Oak Ridge National Laboratory / The University of Tennessee, Knoxville, USA

Transit time estimation

Theory

For a mathematical analysis of the transit time estimation process, the zero-mean thermocouple noise signals are modelled as

$$x_1(t) = s(t) + n_1(t) \quad (2-1)$$

$$x_2(t) = \alpha s(t-D) + n_2(t) , \quad (2-2)$$

where $x_1(t)$ and $x_2(t)$ are the noise signals of the up-stream and the down-stream thermocouple respectively, $s(t)$ is the common signal, α is an attenuation factor, and $n_1(t)$ and $n_2(t)$ are uncorrelated noise influences. The time delay D corresponds to the time shift τ at which the cross-covariance function $R_{12}(\tau)$ (CCF)

$$R_{12}(\tau) = E[x_1(t+\tau)x_2(t)] \quad (2-3)$$

has its maximum (Priestley, 1981).

In the frequency domain, the transit time phenomenon can be seen from the phase behaviour of the cross-power spectral density $G_{12}(f)$ (CPSD):

$$G_{12}(f) = \alpha G_{ss}(f) e^{-j2\pi f D} , \quad (2-4)$$

where $G_{ss}(f)$ is the auto-power spectral density (APSD) of the common signal. The transit time can be estimated from the slope of the linear phase behaviour of the cross-spectrum. This involves the subjective choice of a fit interval, algorithms to extrapolate the phase behaviour and, in general, the choice of a weight function for the measured phase data. For these reasons, an estimation of the transit time from the CCF (the location of the maximum) could be preferred. With respect to the weight function in the frequency domain, however, it is shown below that the estimation of the transit time from the CCF can be arranged in such a way that it still involves a weight function in the frequency domain.

The CCF and the CPSD are related by the inverse Fourier transform

$$R_{12}(\tau) = \int_{-\infty}^{\infty} G_{12}(f) e^{j2\pi f \tau} df . \quad (2-5)$$

The objective is to produce a reliable and accurate estimation of the location of the maximum of the CCF. If the CPSD is not constant as a function of the frequency, the CCF will not exhibit a sharp peak. From this point of view, whitening the CPSD before calculating the CCF lowers the variance. External noise increases the variance of the transit time estimation. In order to suppress the influence of external noise, it is

advantageous to give a low weight to the frequency region in which the coherence between the signals $x_1(t)$ and $x_2(t)$ is low, before transforming the CPSD to the CCF. When both the CPSD and the coherence are not constant as a function of frequency, a combination of whitening and suppressing must be applied in order to lower the variance of the transit time estimation \hat{D} .

Weighting can be achieved by multiplying the CPSD by a real valued weight function $\psi(f)$ before applying the inverse Fourier transform. The resulting cross-covariance function is the so-called generalized correlation (Knapp and Carter, 1976; see also Federico *et al.*, 1982)

$$R_{12}^{(g)}(\tau) = \int_{-\infty}^{\infty} \psi(f) G_{12}(f) e^{j2\pi f\tau} df. \quad (2-6)$$

When *a priori* knowledge about the noise spectra is available, the weight function $\psi(f)$ can be chosen according to the spectral characteristics, with the objective of lowering the variance of the transit time estimation when the generalized correlation $R_{12}^{(g)}(\tau)$ is used. For the generalized correlation $R_{12}^{(g)}(\tau)$ the following expression for the variance of the transit time estimation $\text{var}[\hat{D}]$ can be derived

$$\text{var}^{(g)}[\hat{D}] = \frac{\int_{-\infty}^{\infty} \psi^2(f) (2\pi f)^2 G_{11}(f) G_{22}(f) [1 - \gamma_{12}^2(f)] df}{T \left[\int_{-\infty}^{\infty} (2\pi f)^2 |G_{12}(f)| \psi(f) df \right]^2}, \quad (2-7)$$

where T is the measurement time, and $\gamma_{12}^2(f)$ is the coherence

$$\gamma_{12}^2(f) = \frac{|G_{12}(f)|^2}{G_{11}(f) G_{22}(f)}. \quad (2-8)$$

Equation (7) can be used to calculate the variance when the CCF is used directly for estimating the transit time ($\psi(f) = 1$).

Knapp and Carter (1976) showed that on the assumption that $s(t)$, $n_1(t)$ and $n_2(t)$ are Gaussian, the variance of the transit time estimation \hat{D} is minimized when the so-called Hannan-Thomson (HT) weight function is taken:

$$\psi^{HT}(f) = \frac{1}{|G_{12}(f)|} \frac{\gamma_{12}^2(f)}{1 - \gamma_{12}^2(f)}. \quad (2-9)$$

Furthermore, it is shown that the variance of \hat{D} achieves the Cramér-Rao lower bound,

$$\text{var}^{HT}[\hat{D}] = \left\{ 2T \int_0^{\infty} (2\pi f)^2 \frac{\gamma_{12}^2(f)}{1-\gamma_{12}^2(f)} df \right\}^{-1}, \tag{2-10}$$

when the HT-processor is used. From this expression it follows that the variance is inversely proportional to the measurement time T , and that high frequency coherence is very important for a low variance. In the limit, when coherence is unity for a certain frequency region, the variance is zero.

Example

The effect of processing on the spectral characteristics, the CCF, and the variance of the transit time estimation are demonstrated by the following example. In Fig. 1 (left) the spectra and CCF of two artificially generated noise sequences are plotted. Figure 1 (right) shows the spectra and CCF after HT-processing. Comparing the shape of the original and the processed CPSD, it can be seen that the HT-processor increases the CPSD where the coherence is high and reduces the CPSD where the coherence is low. Furthermore, the plots show that processing has no effect on coherence (if the APSDs are processed accordingly) and on phase behaviour (because $\psi^{HT}(f)$ is real). In this case

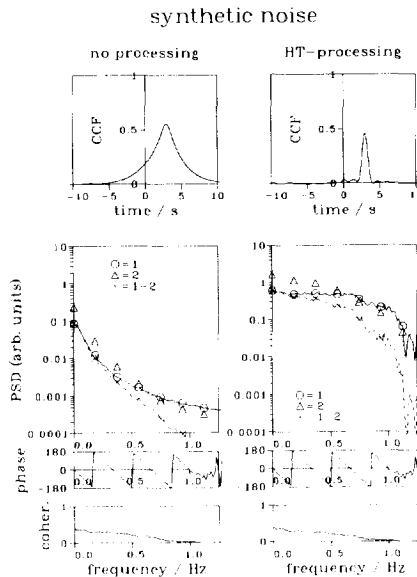


Figure 2-1. Effect of Hannan-Thomson processing on the noise signal characteristics. Example with artificially generated noise sequences.

of artificially generated noise the variance of \hat{D} , as calculated from Eq. (7) (with $\psi(f)=1$) and Eq. (10), is reduced by a factor of 3.

Practical aspects

In practice it is only possible to make an estimation of the spectra $G_{12}(f)$, $G_{11}(f)$ and $G_{22}(f)$, but for a sufficiently large measurement time, these spectra are estimated accurately. Furthermore, if the spectra do not change much in time, an accurate estimation of the spectra coming from a lengthy measurement can be used to construct a processor for a short measurement used for the estimation of the transit time.

Sampling causes the CCF to become discrete. When the standard deviation of the transit time estimation is much larger than the width of the sampling interval, the systematic error can be neglected. But in practice both the sampling time and the standard deviation depend on the frequency contents of the signals and can be of the same order of magnitude. In order to avoid a systematic error due to sampling, the CCF (or the generalized correlation) can be interpolated before locating its maximum. On the assumption that the CPSD is zero above a certain frequency, the CCF can be interpolated by extending the CPSD with a number of zeroes before transformation to the CCF.

Another practical problem which may lead to systematic errors is the data or lag window used. Compensation is necessary when the (resulting) lag window is not rectangular (the so-called Boxcar lag window; Bertora *et al.*, 1975).

Downcomer thermocouple transit time measurements

Theoretical prediction and measurement of the standard deviation

In order to check the theoretical prediction of the standard deviation of the measured transit time, many transit time measurements were performed. The experimental standard-deviation was calculated from the set of transit times, and its value was compared with the theoretically predicted value.

The measurements were performed at four stationary reactor conditions. At each reactor condition, a number of measurements was performed. Each measurement consisted of 50 records of 128 samples. The number of measurements for each reactor condition is listed in Table 1 together with a summary of the reactor operating conditions. The noise signals of the thermocouples A41Y and A52Y were sampled at a sampling rate of 4 s⁻¹.

The signals were compensated for DC drift. No significant drift in the standard

Table 2-1. Set-up and results of the transit time measurements. The error concerns the statistical error only.

| power MWth | number of measurements | total experi- ment time h | transit time | | 2σ error s |
|---------------|---------------------------|---------------------------------|---------------|---------------|----------------------|
| | | | no proc. s | HT-proc. s | |
| 131 | 10 | 4.4 | 2.133 | 2.141 | 0.011 |
| 145 | 7 | 3.1 | 2.141 | 2.141 | 0.014 |
| 156 | 20 | 8.9 | 2.148 | 2.141 | 0.009 |
| 175 | 100 | 44.4 | 2.141 | 2.125 | 0.005 |

deviation and the spectral characteristics was found, and, as is shown below, the transit time only varied due to statistical errors.

By averaging the spectra of all measurements at a certain operating condition, an accurate estimation of the APSD and the CPSD was made. These average spectra were used to predict the standard deviation of the measured transit time for an estimation based on a single measurement of 50 records (with Eq. (10) for the HT-processor and Eq. (7) with $\psi(f)=1$ for the unprocessed CCF; Note that the variance follows the usual inverse proportionality with respect to the measurement time). For the experiment at 175 MWth these standard deviations are

$$s_p = 0.024 \text{ s} ; s_p^{HT} = 0.023 \text{ s},$$

where the superscript *HT* denotes the HT-processing and the subscript *p* indicates that these variables are predicted standard-deviations.

The values show that HT-processing does not lower the variance dramatically - apparently the CPSD is already quite optimal for transit time estimation. This can be seen from Fig. 1-6 and the expression for the weight function $\psi^{HT}(f)$ (Eq. (9)). This weight function takes both the CPSD and coherence into account. As a result the processing only slightly modifies the spectrum, and the resulting covariance function strongly resembles the original CCF.

The CCFs were interpolated 32 times by extending the spectrum with zeroes. This made the effective sampling time 7.8 ms.

For the experiment at 175 MWth, 100 measurements were available. For each measurement the transit time was estimated with HT-processing and no processing ($\psi(f)=1$). Figure 2 shows the estimated transit time as a function of the measurement

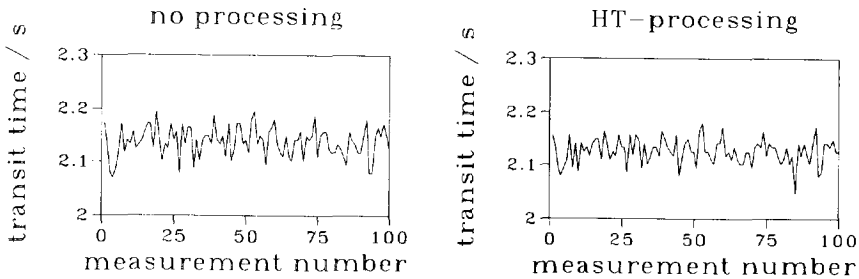


Figure 2-2. The set of measured transit times at 175 MWth. Left without processing, right with HT-processing.

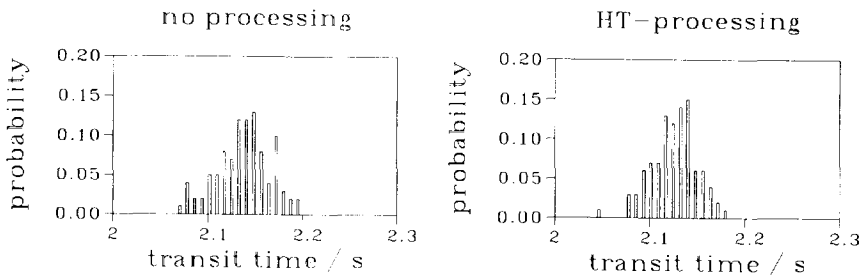


Figure 2-3. Probability distribution of the measured transit times at 175 MWth. Left without processing, right with HT-processing.

number. It can be seen that the transit time shows no apparent drift and varies erratically. In Fig. 3 the distribution of the estimated transit time is plotted. The plots show a Gaussian-like distribution.

From the sets of transit times the following standard deviations were calculated (the subscript m indicates that these variables are the measured standard-deviations)

$$s_m = (0.028 \pm 0.004) \text{ s} ; s_m^{HT} = (0.023 \pm 0.003) \text{ s},$$

where the error specification is based on the 95 % confidence region for the statistical error in the standard deviation estimation if all measurements are assumed to be independent. A comparison of these values with the before-mentioned s_p -values leads to the conclusion that for these downcomer thermocouple transit time measurements Eqs. (7) and (10) predict the variance very well in the case of HT-processing and quite well for the unprocessed case.

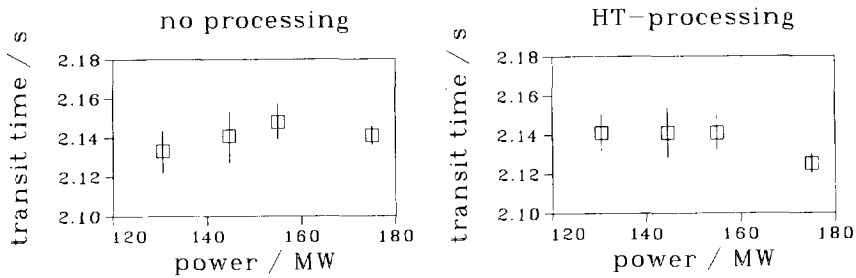


Figure 2-4. Result of the transit time measurements. Left without processing, right with HT-processing.

Results of averaged transit time measurements

The results of the averaged transit time measurements are presented in Table 1 and Fig. 4. The transit times were estimated from the averaged spectra with the before-mentioned techniques. In the case of the HT-processed estimation, the weight function was calculated from the averaged spectra. The given errors were calculated from the expressions for the variance of unprocessed and HT-processed transit time estimations and represent the statistical errors only. In the cases of the 175 MWth and 156 MWth experiments this statistical error is of the same order of magnitude as the effective sampling time. The total error is a combination of the statistical and the systematic error due to discretization of the CCF.

Taking into account the statistical accuracies, the transit time obtained from the unprocessed CCF is in accordance with the transit time obtained from the HT-processed CCF, apart from the experiment at 175 MWth. This implies that the simple transit time model which is applied here (Eqs. (1) and (2)) is not valid throughout. The deviation, however, is less than 1 % of the transit time. Possible sources of error are the difference in the time constants of the two thermocouples, or some dissipation of the fluctuations, which accompanies the transportation of the fluctuations. The former source of error was investigated with the use of a measurement performed by Kleiss (1984) of the noise signals of two downcomer thermocouples which are only 5 cm axially displaced. The high-frequency measurements show non-linear behaviour of the phase of the CPSD at 8 Hz and 10.5 Hz. These two break points correspond to time constants of 0.02 s and 0.015 s. The magnitude of these values agrees well with the values measured by Termaat (Termaat, 1991). The difference in the thermocouple response-times is small enough to make reliable transit time measurements possible.

The remaining cause of the difference between the estimations of the transit time

from the unprocessed and the HT-processed CCF is some dissipation of the fluctuations, which accompanies the transportation of the fluctuations. The dissipation can be seen from the decreasing RMS-value of the downcomer thermocouple noise signals from the up-stream to the down-stream thermocouples (Stekelenburg *et al.*, 1991). This effect is demonstrated in chapter 3.

With the use of a calibration curve, the circulation mass flow rate can be calculated from the measured transit times. This calibration curve was generated by performing numerical simulations of the downcomer flow. This investigation is presented in chapter 3. The physical interpretation of the circulation flow measurements is discussed in chapter 6.

Conclusions

The noise signals of the two axially displaced downcomer thermocouples A41Y and A52Y show a clear transit time. This transit time is closely related to the magnitude of the circulation flow rate. In this chapter, theoretical and practical aspects of transit time estimation are discussed. The theory of transit time estimation gives tools for predicting and lowering the standard deviation of transit time estimations. With the use of a large set of measurements of the noise signals of A41Y and A52Y the standard deviation of the measured transit time is compared with the theoretically predicted standard-deviation. Good agreement was found. Methods for lowering the standard deviation by processing the cross-power spectral density of the two noise signals are described, but, as to these thermocouple noise signals, little improvement could be achieved. The transportation of the temperature fluctuations of the downcomer flow is accompanied by some dissipation of the temperature fluctuations. This phenomenon affects the reliability of the estimated transit time, but the resulting error is only of the order of 1 % of the transit time.

It can be concluded that the noise signals of the two downcomer thermocouples A41Y and A52Y can be used for estimation of the circulation flow rate. The relation between the measured transit time and the circulation flow rate is discussed in the next chapter.

chapter 3

Coolant flow rate estimation - numerical simulation of the downcomer flow¹

Introduction

By applying noise analysis techniques to the noise signals of the downcomer thermocouples A41Y and A52Y, an estimation is made of the average transit time of fluctuations in the temperature of the downcomer flow from thermocouple A41Y to A52Y (see chapters 1 and 2; see Figs. 1-2, 1-4 and 1-5 for thermocouple coding). This transit time supplies information on the circulation flow rate. A problem with this measurement, however, is the interpretation of the measured transit time, and the conversion of this transit time into parameters like the average velocity or the mass flow rate, particularly in cases in which the flow field is not uniform. Usually this problem is solved by calibrating the technique with another flow meter. If no other flow meter can be installed, the measured transit time and the mass flow rate can be linked using information about the flow field through, for instance, numerical flow field calculations. In this chapter the numerical flow field calculations, which were performed to obtain a calibration curve for the estimation of the circulation flow rate from the measured transit time, are described.

¹This chapter is an adapted version of:
Stekelenburg A.J.C., Van der Hagen T.H.J.J. and Van den Akker H.E.A., *Numerical simulation of turbulent flow for calibration of cross-correlation flow measurements*, accepted for publication in the *Int. J. Num. Methods for Heat and Fluid Flow*

As early as in 1969 the measured downcomer thermocouple transit times were used for estimating local water velocities and the total coolant flow rate (Termaat, 1970; Oosterkamp, 1987). These measurements show that the velocity varies over the downcomer channel. Thermocouple signals were simulated by Koopmans, by combining fluid flow calculations and Monte Carlo simulations (see also Oosterkamp, 1987). With increased computer speed and capacity, improved computer programs, and improved analysis techniques it is possible to gain even more insight and make a reliable and accurate estimation of the flow rate.

Important ingredients of the translation of the noise signals to the flow rate are the characteristics of the downcomer flow field. In the current investigation this information is obtained by performing two- and three-dimensional turbulent flow calculations as well as simulation of a steady state flow with transient thermal characteristics with the use of FLUENT (FLUENT, 1990; Colenbrander, 1991), a general purpose computer program for modelling fluid flow. With this method the response of downcomer thermocouples to temperature fluctuations was directly simulated, thus providing a natural link between the total flow rate and the measured transit time.

For detailed information on computational fluid dynamics, the reader is referred to literature (Peyret and Taylor, 1983; George and Arndt, 1989; Colenbrander, 1991; Launder, 1991).

Fundamentals of the computer program

The computer program FLUENT (V3.0) was used to calculate the characteristics of the downcomer flow field. With this program it is possible to model turbulence by two turbulent flow models: a two-equation model (the $k-\epsilon$ model) or the Algebraic Stress Model. The equations for conservation of mass, momentum and energy are reduced to their finite volume analogues while the domain is divided into computational cells. The resulting set of equations is solved by a semi-implicit iterative scheme. Integration in time is fully implicit. For interpolation between grid points and for calculation of the derivatives of the flow variables a power-law differencing scheme or a Quadratic Upwind Scheme (QUICK) is used. Different types of boundary conditions can be specified. For inlet cells velocity vectors and turbulence intensity must be specified. In symmetry cells zero gradient boundary conditions are applied (except for lateral velocity components which must vanish). In outlet cells overall continuity is assured, and it is assumed that the flow is fully developed. The log-law is employed for computing the shear stress in the turbulent flow near the wall.

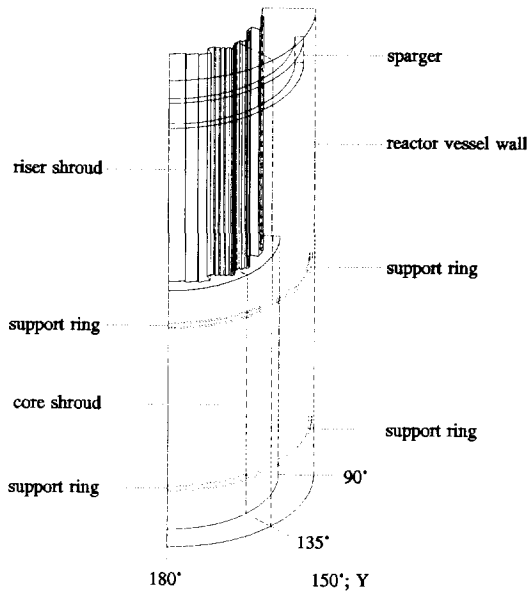


Figure 3-1. Geometrical outline of the downcomer channel for the three-dimensional calculations. For this plot, the calculational domain was mirrored in the first θ -plane.

The geometry of the downcomer channel

The annular downcomer channel consists of two regions, an upper region surrounding the riser, and a lower region next to the core (Figs. 1, 1-1, 1-2, and 1-5). The shape of the riser follows the arrangement of the outer fuel bundles. The core is surrounded by the core shroud, which is a cylinder.

The downcomer channel is approximately 5.5 m in length. At the height of the riser it is 0.4-0.5 m in width and in the lower region it is 0.338 m in width. The inner radius of the reactor vessel is 1.399 m.

An important obstruction in the downcomer channel is the feedwater sparger, which is a ring of 360° , and which has a height of 28 cm (in the flow direction) and a width of 10 cm. Cold feedwater is injected from tiny holes in the feedwater sparger into the downcomer channel. The feedwater flow is approximately 70 kg/s. The downcomer flow is approximately 1350 kg/s.

At each of two elevations, eight instrument support rings are mounted onto the inner wall of the vessel. These arched rings are stainless steel strips, 1 cm in thickness and 6 cm in height (in the flow direction) which follow the vessel wall over 41° at a spacing of 4 cm. This implies that the eight arcs do not cover 360° completely. These arcs, and

the angularities of the riser make the downcomer channel a three-dimensional problem.

The inner vessel wall is covered with stainless steel strips, leading to a corrugated wall with a roughness of approximately 2 mm and a period of 5 cm.

Three-dimensional calculations

As described above, the annular downcomer channel represents a three-dimensional problem. Arguments as to symmetry reduce the calculation domain to a segment of 45° . Because of the size of the domain and the flow conditions (the Reynolds number is approximately 4×10^6), the three-dimensional grid, having a maximum of 25,000 grid cells in FLUENT V3.0, is too coarse, which leads to lower reliability of the result calculated. The reliability of the result can be investigated by performing test calculations in which the influence of grid cell size, discretization scheme and turbulence model on the calculational result is investigated. These calculations demonstrate, as shown below, that the three-dimensional problem may confidently be collapsed into a typical two-dimensional plane in which much smaller grid cells can be applied.

The annular downcomer channel is modelled in cylindrical coordinates. The flow direction, which is downward in this case, is called the z -direction, the radial coordinate is called r , and the angle is called θ . The corresponding velocities are called u , v , and w , respectively.

Set-up

For the annular downcomer channel, a three-dimensional grid of $r \times z \times \theta = 21 \times 59 \times 20 = 24,780$ cells was designed. The result of the geometric modelling is plotted in Fig. 1. Where large changes in flow field quantities were expected, the grid cell size was reduced. Inlet cells were put in the first z -plane, outlet cells at the last z -plane, and symmetry cells at the first and last θ -plane. The last r -plane was completely filled with wall cells. The first 5 r -planes were filled in such a way that the shape of the riser was approximated.

Because the support rings are smaller (1 cm in y -direction) than the grid cells at that location (2.5 cm), the rings were modelled with the use of FLUENT's porous media option. With this option a pressure drop per unit length of $\frac{1}{2} C \rho u^2$, where ρ is the water density and C (m^{-1}) is a constant, is introduced over the grid cell. The constant C is obtained from the drag coefficient C_w for flow around objects. With a C_w of 2 for square rods and a length of the strip of 6 cm, C is $2/(0.06 \text{ m}) = 33 \text{ m}^{-1}$.

Table 3-1. Data on the downcomer flow

| physical quantity | unit | actual value above sparger | actual value below sparger | value in 3D calcula- tion | value in 2D calcula- tion |
|----------------------------------|------------------------------------|-------------------------------------|-------------------------------------|------------------------------------|------------------------------------|
| flow surface at sparger level | m ² | 3.52 | - | 3.53 | 3.75 |
| temperature | K | 563 | 558 | 558 | 500 * |
| density | kg m ⁻³ | 732 | 743 | 743 | 743 |
| dynamic viscosity | kg m ⁻¹ s ⁻¹ | 8.96x10 ⁻⁵ | 9.17x10 ⁻⁵ | 9.17x10 ⁻⁵ | 9.17x10 ⁻⁵ |
| thermal conductivity | W m ⁻¹ K ⁻¹ | 0.568 | 0.577 | - | 0.577 |
| specific heat capacity | J kg ⁻¹ K ⁻¹ | 5.50x10 ³ | 5.35x10 ³ | - | 5.35x10 ³ |

*The temperature is varied in time (see Fig. 7), 500 K is the inlet temperature at the beginning of the simulation and the inlet temperature after 2 s.

A uniform velocity and turbulence intensity distribution was taken at the inlet cells. For the turbulence intensity (the RMS-value of the velocity fluctuations with respect to the mean velocity) the program's default value of 10 % was taken.

The physical properties of water at 75.5 bar and 558 K (operating conditions) given in Table 1 were used (Suessbrich, 1978).

Reliability

Insight into the reliability of the numerical flow calculations was gained by studying the influence of the mesh size, the model for turbulence, and the discretization scheme on the results. In order to offer the possibility of a reduction of the mesh size, which leads to an increase of the number of grid cells, the reliability study of the three-dimensional calculation was performed for a small sub-section of the downcomer channel. The test domain was two-dimensional (r - z -geometry), but still in annular geometry (with results independent of θ). With this domain it was possible to reduce the mesh size with a factor of four in both directions. Also, the model for turbulence, and the discretization scheme were varied. As in the case of this application the transport of temperature fluctuations is important, the reliability of the calculation was judged by looking at the calculated u -velocity at several positions. It was found that the difference between the calculated u -velocities for various settings was sometimes as large as 20 % at some positions.

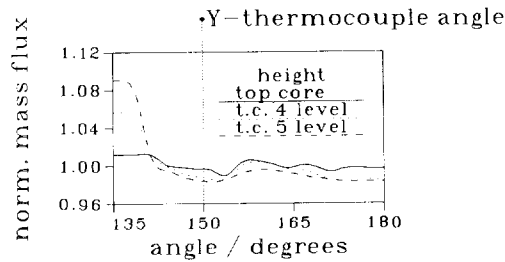


Figure 3-2. Calculated angular dependence of the downcomer flow at the top of the core, and at thermocouple levels 4 and 5. The mass flux is normalized to the average mass flux.

This result demonstrated the necessity for applying a finer mesh. Because the number of grid cells applied in the three-dimensional calculation was already close to the program's maximum number of grid cells, it was investigated whether the downcomer flow-field could be calculated in r - z -geometry rather than in r - z - θ -geometry. This was done by looking at the angular dependence of the axial flow calculated with the three-dimensional domain. The flow rate in the z -direction through all grid cells (all possible r -positions) at a certain z - and θ -position was summed up. This was done for all angles and for three elevations: at the top of the core, and at thermocouple elevations 4 and 5. The result is plotted in Fig. 2. This plot shows that the flow varies some 10 % with the angular position.

However, at 150° (the Y-thermocouple plane) the difference between the mass flux at thermocouple elevations 4 and 5 is only 0.5 %. This indicates that the three-dimensional domain can confidently be collapsed into two dimensions. The magnitude of the flow rate applied in the two-dimensional calculation and the flow rate in reality can be linked with the use of the angular dependence shown in Fig. 2.

This result was obtained from the three-dimensional calculation which was found to have a low reliability of the calculated u -velocity at some positions. The reliability of the angular dependence (which is an integrated quantity) following from this calculation, was investigated by performing calculations for a smaller, but still three-dimensional domain. This domain (Fig. 3) was part of the downcomer channel next to the core which included an instrument support ring. The domain was limited to 30° and the length was 83 cm. This offered the possibility of reducing the grid cell size with a factor of two in all directions. With the coarse grid the support ring was modelled with porous cells. With the fine grid the cells were small enough to allow for modelling the strip by wall cells. As in the two-dimensional test calculation, the model for turbulence and the discretization scheme were varied. Also, the influence of wall roughness and

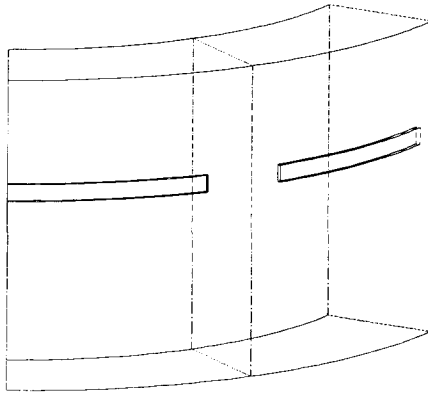


Figure 3-3. Geometrical outline of the three-dimensional test domain. For this plot, the calculational domain was mirrored in the first θ -plane.

inlet turbulence intensity was studied. The results were judged by looking at the summation over the r -direction of the calculated flow rate of all cells at the outlet at the θ -plane where the thermocouples are located. For all test calculations the difference between the result and the average of all tests was smaller than 0.3 %. From this it can be concluded that although the calculated u -velocity is strongly dependent on grid size, turbulence model, and discretization scheme, the angular dependence of the flow rate (Fig. 2) can be reliably calculated from the three-dimensional calculation.

Results

From the three-dimensional calculation for the full geometry (Fig. 1) it followed that the flow at the Y-thermocouple angular position (150°) is mainly two-dimensional. For linking the flow rate in a two-dimensional calculation and the flow rate in reality, the mass flux at the Y-thermocouple angular position is important. Quantitatively, this link can be expressed in terms of the calculated mass flux ϕ_c'' at this angular position, as compared to the mass flux ϕ_u'' following from an angularly uniform flow distribution, by introducing a form factor f

$$f = \frac{\phi_c''}{\phi_u''} \quad (3-1)$$

For ϕ_c'' the average value of the mass fluxes in the thermocouple plane at thermocouple elevations 4 and 5 can be taken. In a calculation with a total flow rate of 1500 kg/s, the calculated mass flux at the thermocouple plane was found to be $563.6 \text{ kg m}^{-2} \text{ s}^{-1}$, while $\phi_u'' = 573.5 \text{ kg m}^{-2} \text{ s}^{-1}$, leading to $f = 0.9827$. From this value it follows that the calcu-

lated mass flux is 1.73 % lower than in the uniform case.

In order to check whether this result is applicable to a wide range of flow rates, another three-dimensional calculation was performed with a total flow rate of 600 kg/s. The mass flux at the thermocouple plane following from this calculation was $225.6 \text{ kg m}^{-2} \text{ s}^{-1}$, while in the uniform case the mass flux would be $229.4 \text{ kg m}^{-2} \text{ s}^{-1}$. From these values it follows that $f=0.9834$ and that, at this flow rate, the calculated mass flux is 1.66 % lower than in the uniform case.

These two calculations show that the value $f=0.983$ can be used to collapse the three-dimensional domain into two dimensions.

It was stated above that all three-dimensional test calculations lead to the same result for the mass flux within ± 0.3 %. Because the downcomer channel includes two axially displaced support rings (Fig. 1), and the test calculation domain only one (Fig. 3), this value can be multiplied with a factor of two when applied to the full geometry. The resulting value of ± 0.6 % is used for the 95 % confidence interval for the calculated form factor f , leading to $f=0.983 \pm 0.006$. Of course it must be remarked that the estimation of the error follows from a comparison of calculation results only rather than from a comparison with measurements.

Two-dimensional calculations

By calculating the problem in two dimensions (r - z -geometry, but still in annular geometry independent of θ), a much finer grid can be applied within the limit of 25,000 grid cells. The form factor, as introduced above, can be used to link the total (three-dimensional) flow rate to the flow rate that is applied in the two-dimensional calculation.

With a calculated velocity vector field however, the problem has not been solved yet. The purpose of the investigation was to establish a link between the total flow rate and the measured transit time between thermocouple signals. This translation is made by performing a simulation of the transportation of a temperature fluctuation.

Steady-state flow

The calculational domain of the two-dimensional calculations is plotted in Fig. 4. The length of the domain is the same as in the three-dimensional calculation. Also, the thickness of the downcomer channel next to the core is the same. For the thickness next to the riser, the actual distance between the vessel wall and the riser at the Y-thermocouple angular position was taken. The calculation was performed in annular

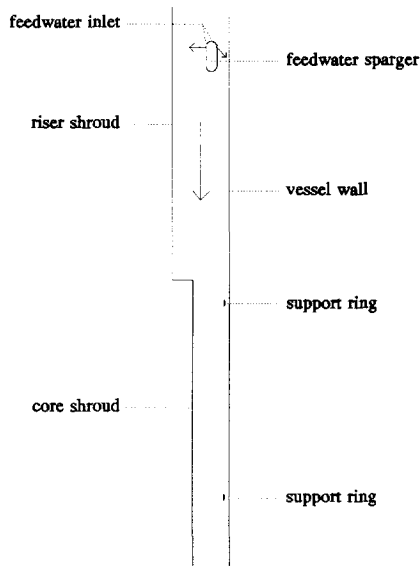


Figure 3-4. Geometrical outline of the downcomer channel for the two-dimensional calculations geometry. A grid of $z \times r = 268 \times 93 = 24,924$ cells was designed. As in the three-dimensional calculation the grid cells were taken smaller where large changes in the flow field variables were expected. Grid cell size allowed for modelling the instrument support rings by a set of wall cells. As in the three-dimensional calculation inlet cells were taken in the first z -plane, and outlet cells in the last z -plane. Two additional inlet cells were placed in the sparger for modelling the feedwater injection. These cells had a length (in the z -direction) of 6.2 mm.

In reality, feedwater is injected with a velocity of approximately 7 m/s from tiny holes in the feedwater sparger into the downcomer flow in the $+r$ and $-r$ direction. This leads to a perturbation of the downcomer flow. This process is modelled in two dimensions (r - z -geometry, but still in annular geometry, results independent of θ) by representing the sparger with the individual holes by a ring (in three dimensions) from which water flows. The effect of the water injection from the ring on the downcomer flow was approximated by equating the momentum flow rate of the injected feedwater in model and reality; hence,

$$\phi_f + \phi_c = c_1 \quad (3-2)$$

$$\frac{\phi_f |v_f|}{\phi_c |v_c|} = c_2, \quad (3-3)$$

Table 3-2. The two-dimensional calculation cases A-D

| case | actual total flow (kg/s) | actual feedwater flow (kg/s) | total flow in 2D (kg/s) | inside feedwater flow (kg/s) | outside feedwater flow (kg/s) | transit time (s) | product of transit time and total flow (10^3 kg) |
|------|--------------------------|------------------------------|-------------------------|------------------------------|-------------------------------|------------------|---|
| A | 1477 | 80 | 1453 | 99 | 55 | 1.96 | 2.89 |
| B | 1078 | 80 | 1060 | 97 | 54 | 2.72 | 2.93 |
| C | 579 | 80 | 570 | 90 | 50 | 5.29 | 3.06 |
| D | 1477 | 40 | 1453 | 50 | 27 | 1.99 | 2.94 |

where ϕ and v are the flow rates and velocities respectively, the subscripts f and c denote feedwater and circulating water respectively, and the constants c_1 and c_2 should be equal in model and reality. With this modelling, it can be taken into account that the outflow area of the ring is not equal to the area of the holes. The problem that the number of holes is different for the inside and the outside of the feedwater sparger is solved by applying Eqs. (2) and (3) to the inside and the outside separately. Finally, the flow from the outside holes is deflected in the $+\theta$, $-\theta$ and $+z$ -direction by deflectors on the feedwater sparger. This is modelled by firstly calculating the feedwater flow rate and velocity with Eqs. (2) and (3). Secondly, the inlet velocity vector is rotated 45° into the z -direction. This leads to equal components in the z - and θ -direction (see Fig. 4), and a reduction of the flow rate with a factor of $\sqrt{2}$.

In order to calibrate the flow measurement technique over a large range of the flow rate, several cases were calculated (see Table 2, cases A, B, and C). The sensitivity of the technique as to the modelling of the feedwater flow was tested by considering a case for which the total flow rate was the same as in case A, but for which the feedwater flow rate was halved (case D). The model flow rates given in Table 2 were calculated from the actual flow rates by applying the form factor $f=0.983$. The feedwater flow rates for the in- and the outside of the feedwater sparger were calculated by applying the model for the feedwater injection presented above, with the use of the values given in Tables 1 and 3. For this reason, actual value of the feedwater flow rate is different from the value applied in the model.

In Fig. 5 the calculated stream lines for case A are plotted for the region near the feedwater sparger. The plot shows that the feedwater injection strongly influences the downcomer flow field. In Fig. 6 the calculated profiles of the u -velocity for the same

Table 3-3. Data on the feedwater flow

| physical quantity | unit | actual value | value in 2D calculation |
|-------------------------------|------------------------------------|-----------------------|-------------------------|
| surface at inside of sparger | m ² | 7.96x10 ⁻³ | 46.3x10 ⁻³ |
| surface at outside of sparger | m ² | 4.51x10 ⁻³ | 50.2x10 ⁻³ |
| temperature | K | 411 | 550 |
| density | kg m ⁻³ | 932 | 743 * |
| dynamic viscosity | kg m ⁻¹ s ⁻¹ | 2.01x10 ⁻⁴ | 9.17x10 ⁻⁵ * |
| thermal conductivity | W m ⁻¹ K ⁻¹ | 0.697 | 0.577 * |
| specific heat capacity | J kg ⁻¹ K ⁻¹ | 4.26x10 ³ | 5.35x10 ³ * |

*Based on a temperature of 558 K.

case are plotted for the lower region next to the core. It can be seen that the u -velocity profile changes downstream, which explains qualitatively that using different thermocouple pairs leads to different measured u -velocities (Termaat, 1970; Oosterkamp, 1987).

Simulation of transient flow

The transportation of water temperature fluctuations was simulated by varying the inlet temperature in time and calculating the temperature field under transient thermal conditions. As described in chapter 1, the fluctuations of the temperature of the downcomer flow are caused by local fluctuations of the circulation flow rate or local fluctuations of the carry under. Both these causes lead to a fluctuating specific enthalpy of the downcomer flow below the feedwater sparger. In the calculational model, this was simulated by applying a perturbation to the temperature of the water at the inlet of the downcomer channel. The inlet temperature introduced as a function of time is plotted in Fig. 7. By choosing this triangular shape the power spectral density of the applied fluctuation is non-zero up to 1 Hz. The fluctuation was applied uniformly over the inlet cells. During simulation the temperature at the thermocouple locations was registered as a function of time. In this way, the response of the thermocouples to a temperature fluctuation at the inlet was directly simulated. As only the advection of the temperature fluctuation is important here, heat sources like the hot core, or heat sinks like the vessel wall were not taken into account - the heat flux density through all walls

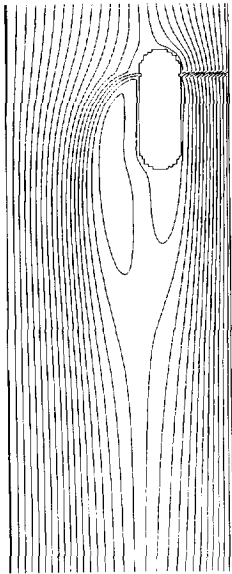


Figure 3-5. Calculated stream lines near the feedwater sparger for case A

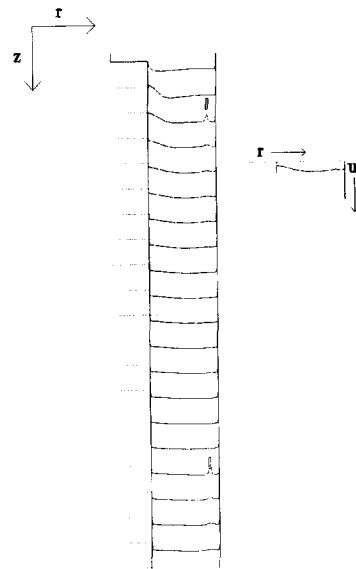


Figure 3-6. Calculated profiles of the u -velocity for the lower region of the downcomer channel for case A

was taken zero. For the same reason the feedwater temperature was taken constant in time at a value of 550 K.

Table 3 shows a large difference between the properties of the actual feedwater and the feedwater in the model calculations. This difference is due to the difference in the temperature. FLUENT offers the possibility of taking the dependence of the fluid properties on the temperature into account. Temperature measurements with the downcomer thermocouples and downcomer thermocouple noise measurements (Oosterkamp, 1987), however, show that the cold feedwater flow mixes with the hot circulation flow within the region between the feedwater sparger and the level-three thermocouples (which corresponds to approximately 0.7 m). This implies that for simulation of the transient flow in the downcomer channel 0.7 m below the feedwater sparger, the water properties can be fixed at their values at the full-power operating conditions, which saves computing time. The influence of applying this approximation to the region near the feedwater sparger on the flow below the sparger is illustrated with the results for case D (see below).

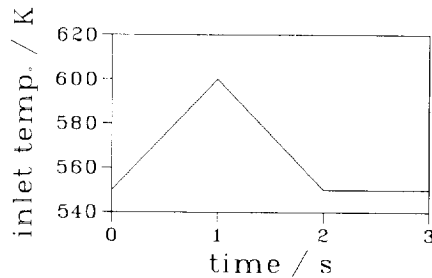


Figure 3-7. Inlet temperature as a function of time for the simulation of transient flow

The integration in time is treated fully implicitly, which implies that the time step for performing the time simulation is not limited by the *Courant-Friedrichs-Lewy stability condition* for explicit discretization of a hyperbolic equation (see, for instance, Peyret and Taylor, 1983). Accuracy, however, is of course influenced by the choice of the time step. The time step was given such a value that, for most grid cells, the product of the time step and the u -velocity is smaller than the length of the cell.

The reliability of the transient flow simulation was tested with the use of a smaller two-dimensional domain. During this simulation, the inlet temperature was varied as a function of time as plotted in Fig. 7, and the temperature at the outlet, 8 cm from the vessel wall (corresponding to a thermocouple position) was registered. The time position of the maximum registered temperature was determined for different mesh sizes, time steps, turbulence models, turbulence intensities, discretization schemes, convergence criteria, wall roughness, and inlet temperature fluctuation amplitude and temperature offset. For reasonable values of the above mentioned variables the time position of the maximum was always located in an interval of $\pm 2.3\%$ around the average value. Variation of the time step affected the registered temperature - a larger time step resulted in a spread of the temperature fluctuation - but did not affect the time position of the maximum temperature.

Turning back to the simulation of transient flow for the two-dimensional downcomer channel, in Fig. 8 the contours of the temperature function for case A for consecutive moments in time for different regions of this channel are plotted. The figure shows how the temperature fluctuation is transported downwards by the flow.

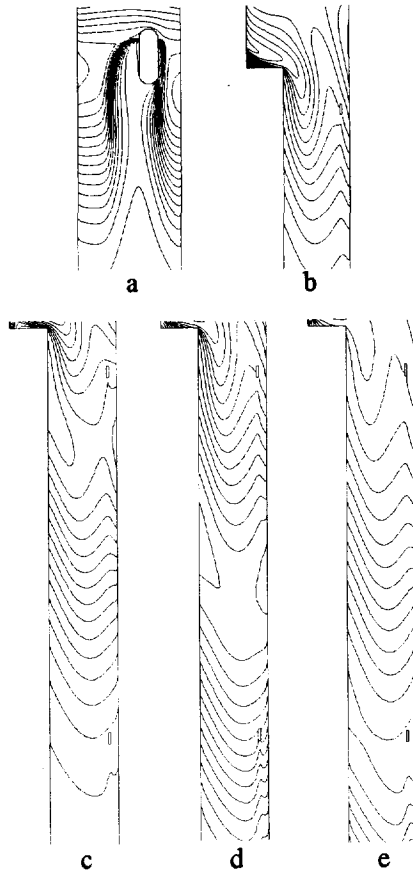


Figure 3-8. Contours of the temperature for case A; a: near the feedwater sparger at $t=2$ s, temperature difference between two lines: $\Delta T=3$ K; b: near the top of the core at $t=5$ s, $\Delta T=2$ K; c, d, e: next to the core at $t=6, 7, 8$ s respectively, $\Delta T=1$ K. For all plots, the minimum temperature is 551 K.

In Fig. 9 the calculated temperature response of the two thermocouples A41Y and A52Y is plotted. From this plot the delay of temperature signal of A52Y, which is a downstream thermocouple, with respect to the signal of A41Y can be clearly seen. That the temperature fluctuation dissipates can be seen from the decrease of the maximum value of the temperature, and the increase of the width of the temperature peak.

The transit times between the calculated thermocouple responses to the applied temperature perturbation were estimated by applying the cross-correlation technique (see

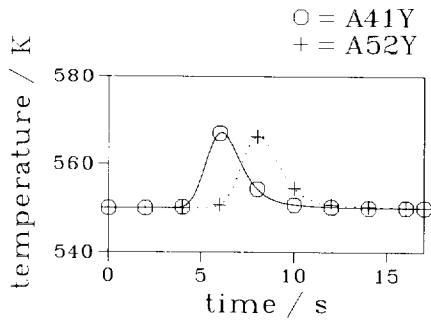


Figure 3-9. Calculated temperature as a function of time for thermocouples A41Y and A52Y for case A. $t=0$ s corresponds with $t=0$ s in Fig. 7.

chapter 2). The results are presented in Table 2. The dissipation of the temperature fluctuation between the two thermocouple positions causes some deviation from the simple transit time model presented in chapter 2 (Eqs. (2-1) and (2-2)). For this reason, transit times estimated through other methods can give different results. For the measured thermocouple noise signals, this effect is discussed in chapter 2. In order to study the influence of this effect on the transit times calculated from the simulated thermocouple responses, the transit times were estimated by applying the following three methods: cross-correlation, the shift in the time-location of the maximum of the two responses, and the shift in the time-location of the centre of mass of the two responses. This study was performed for all four cases. The results for the transit time calculated with the last two methods were always within $\pm 2\%$ of the transit time determined with the cross-correlation method.

Validation

Because the mass flow rate is an unknown variable in the measurements, the absolute values of the transit times obtained by measurements cannot be compared with the transit times following from the calculation. However, measured velocity profile effects, i.e. the relative differences between velocities measured with thermocouple pairs at different radial positions, can be compared with the values resulting from the calculations.

As already mentioned above, only the large distance thermocouple pairs in the lower region of the downcomer channel (see Fig. 1-5) are reliable for velocity estimation. For these large distance thermocouple pairs, the calculations for case A show that the velocity derived from the transit time between signals of the thermocouples 16 cm from the vessel wall is 92.7 % of the velocity obtained from the thermocouples 8 cm from

the vessel wall. This prediction is in good agreement with measurements performed by Termaat (1970) who found that the velocity derived from the transit time measured with the thermocouples 16 cm from the wall is 93.8 % of the velocity measured with the thermocouples 8 cm from the wall.

The fact that the velocities measured with small distance thermocouple pairs are strongly affected by the profile depression caused by the thermocouple instrument tube itself is illustrated by applying the same analysis to the small distance pairs. For instance, from the measurements by Termaat (1970) it follows that the velocity measured with the lowest pair of thermocouples 8 cm from the wall is 75.4 % of the velocity measured with the large distance thermocouples 8 cm from the wall. From the calculations, however, it follows that both velocities should be the same. As in the simulations the instrument tubes were not modelled, it can be concluded that the profile depression is as large as 25 % for the small distance thermocouple pairs.

Synthesis of two- and three-dimensional calculations

The results for the transit time between thermocouple signals A41Y and A52Y for cases A-D are given in Table 2. Also, in this table the product of the transit time and the mass flow rate is given. The difference between this quantity for each case, and the average value for all cases shows that the transit time is inversely proportional to the mass flow rate within +3.6 % and -2.2 % for all four cases. The deviation is systematic - a higher flow rate leads to a larger product of flow rate and transit time. This indicates that the flow-field depends on the mass flow rate. The result is presented graphically in Fig. 10. In this figure the inverse of the transit time is plotted as a function of the mass flow rate. This plot can be considered as the calibration curve for the cross-correlation flow rate measurements. Due to the above-mentioned dependence of the flow-field on the mass flow rate, the calibration curve is non-linear.

Table 2 also shows that the results of the cases A and D differ by 2 % only, although the feedwater flow rate in case A is twice the value in case D. From this it can be concluded that although the injection of feedwater strongly affects the downcomer flow (see Fig. 5), the transit time between the thermocouples A41Y and A52Y is hardly influenced by the amount of feedwater which is injected. This implies that possible errors in the modelling of the flow in the upper part of the downcomer channel only have a small influence on the resulting transit time.

The reliability of the calibration technique can be estimated, once all sources of errors have been considered. As discussed above, the comparison of results of three-dimensional test calculations leads to a relative error of ± 0.6 % in the form factor f .

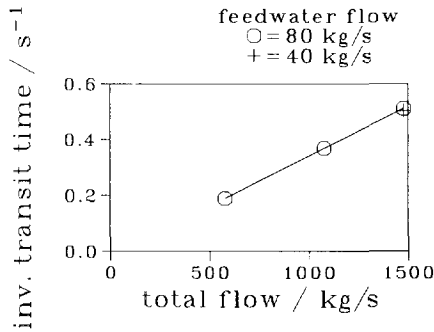


Figure 3-10. Inverse of the calculated transit time for cases A-D as a function of the total three-dimensional mass flow rate

From the investigation concerning the reliability of the two-dimensional transient flow simulations, it was found that for a smaller domain (83 cm length), the error did not exceed $\pm 2.3\%$. As the distance between the thermocouples A41Y and A52Y is 1.6 m, $\pm 4.6\%$ is taken as the error interval. Furthermore, the dissipation of the temperature fluctuation between the two thermocouple positions leads to an uncertainty in the estimated transit time. This uncertainty was found to be $\pm 2\%$. Combining the three estimated errors and assuming that the errors are independent (calculation of the root of the sum of the squared errors), the error interval of the calibration technique is taken $\pm 5\%$. Again it must be stressed that the estimated errors follow from the comparison of the results of many test calculations, and that it is still possible that all calculations deviate systematically from reality.

Conclusions

The downcomer thermocouple signal cross-correlation flow measurement technique was calibrated by performing numerical fluid flow simulations. The procedure comprises a combination of the extensive use of the computer code's modelling possibilities, including steady-state as well as transient flow, powerful calculational data processing and interpretation, and many test calculations.

The calculated flow field following from a coarse-grid three-dimensional calculation was used to confidently collapse the three-dimensional geometry into two dimensions, although the calculated u -velocity showed a large dependence on grid cell size, discretization scheme and turbulence model.

With a fine-grid two-dimensional calculation the propagation of a temperature fluctuation was simulated. By registering the temperature response at the thermocouple

positions, and applying cross-correlation techniques, the relationship between the measured transit time and the flow rate was established. Three calibration points were taken in the range of 579 kg/s to 1477 kg/s. In this range, the product of the calculated transit time and the mass flow-rate is constant up to +3.6 % and -2.2 %. The influence of the inlet boundary conditions, and the modelling of the flow in the upper part of the downcomer channel on the calibration result is shown to be small. By combining the results of various test calculations, the overall error of the calibration technique was estimated at ± 5 %.

Comparison of the transit times resulting from the calculations and measured transit times shows that the effect of a radial u -velocity profile can be predicted successfully.

chapter 4

**Two-phase flow monitoring
by analysis of in-core detector
noise signals¹**

Introduction

In chapters 2 and 3 a method for estimating the total circulation flow rate is presented. Because of the non-uniform power distribution, due to the control rod pattern, the bundle flow rate, different fuel bundle types and burn-up, the radial distribution of the total circulation flow rate over the core can be highly non-uniform. For this reason, the local two-phase flow conditions are not only axially space dependent, but also radially. For a safe and efficient operation of BWRs, monitoring of local two-phase flow conditions is of the utmost importance. Using data on the two-phase flow conditions, normal operating conditions can be verified, or anomalous conditions can be detected. Furthermore, these data can be used for computer code validation.

For many years, much effort has been put into the development of reliable methods for estimating two-phase flow variables like velocities and void fraction. It is a real challenge to find reliable, safe and low-cost measuring techniques. Analysis of the noise of in-core neutron or gamma detectors in principle offers the possibility of studying local two-phase flow conditions without disturbing the operating condition itself. Furthermore, no complex instrumentation is needed for applying the technique.

¹This chapter is an adapted version of:
Stekelenburg A.J.C. and Van der Hagen T.H.J.J (1993) *Two-phase flow monitoring by analysis of in-core neutron detector noise signals - a literature survey*, *Ann. Nucl. Energy* **20**, 611-621

One well-known technique is the application of the cross-correlation method for measurement of velocities, as described in chapters 1 and 2. While the method described in these chapters involves the noise signals of thermocouples, the in-core two-phase flow velocity measurements involve axially displaced neutron detectors (Randall and Pekrul, 1967; Seifritz, 1972; Seifritz and Cioli, 1973; Wach, 1973; see Kleiss and Van Dam (1981) for a description of a so-called twin self-powered neutron detector). In this application, the propagating disturbances, which are fluctuations of the void fraction, cause perturbations of the neutron flux density, which in turn cause fluctuations of the detector signals (Fig. 1). Practical problems with this technique are the distortion of the fluctuation between the two detectors, the relation between the measured velocity and two-phase flow velocities like the gas or liquid velocity, and the localization of the measured velocity. Because of these problems, the interpretation of these measurements is still difficult.

In order to find possible explanations for the results of in-core neutron noise measurements that were performed at the Dodewaard BWR, presented later in this chapter (see also Stekelenburg and Van der Hagen, 1992a), a study of literature on the monitoring of two-phase flow by the analysis of in-core neutron detector noise signals, was performed (Stekelenburg, 1992b). It was found that the neutronics involved in neutron noise processes is quite well understood, i.e. one is able to predict the response of a neutron detector to, both in space and time, arbitrarily distributed density fluctuations. The research on the fluctuations in two-phase flow, however, is still developing. The field of in-core neutron detector noise analysis for monitoring two-phase flow has a turbulent history. In the literature many different opinions regarding the interpretation of the measurements are given.

This chapter aims at providing a collection of leading opinions and results, from both the field of neutronics, as well as the field of (thermal) hydraulics. All relevant papers from the journals listed in Table 1 were considered.

Two-phase flow induced in-core detector noise

The response of an in-core detector to density fluctuations

In a BWR, differences in bundle power and flow in the bundles neighbouring the detector cause differences in two-phase flow conditions on a macroscale. Also, on a subchannel level these differences exist (Fig. 2). The information present in the detector noise signal has its origin in these different regions. Therefore, it is necessary to study how this information is carried to the detector, and how the detector signal is built up

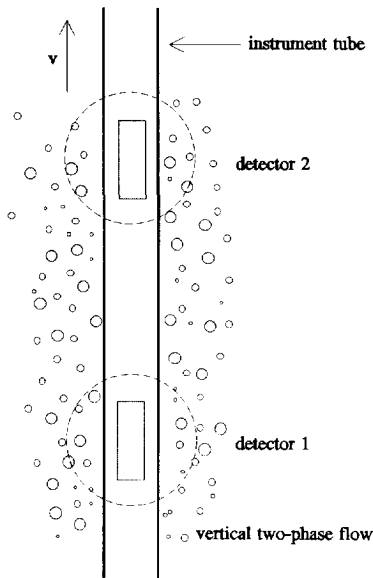


Figure 4-1. Schematic view of an in-core detector pair and propagating fluctuations

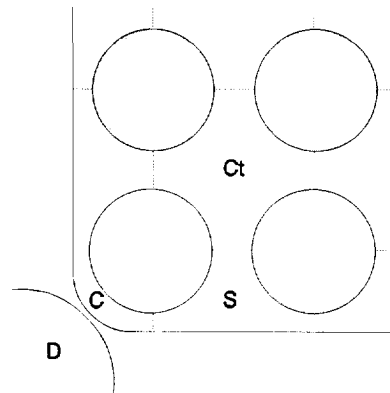


Figure 4-2. Part of a BWR fuel bundle with corner (C), side (S) and central (Ct) subchannel, and detector (D)

from different contributions.

A steam bubble in water causes a local change in absorption and scattering, due to the density difference between water and steam. These changes lead to a perturbation of the flux, which in turn can be detected by an in-core detector. Inspired by the results of neutron noise measurements, Wach and Kosály (1974) set up a model for neutron noise, based on the hypothesis that the neutron noise can be split into a local and a global component. From the results of measurements with axially and radially displaced neutron detectors, also Ando *et al.* (1975) concluded that neutron noise consists of a local and a global component.

In order to calculate the response of an in-core detector to parametric perturbations that are arbitrarily distributed in both space and time, Van Dam (1975) extended the perturbation analysis method (Bell and Glasstone, 1970) to the frequency domain, and introduced this method into the field of in-core noise analysis (see below for an outline of the result). With the application of this method the so-called field-of-view of an in-core detector was introduced (Van Dam, 1976). This field-of-view defines the region, both in the space and frequency domain, in which fluctuations affect the detector signal.

Table 4-1. List of journals included in the literature study

| Journal | period referred to |
|---|--|
| <i>Annals of Nuclear Energy</i> | 1977-1992 |
| <i>Int. J. Multiphase Flow</i> | 1973-1976, 1986-1992 |
| <i>Nuclear Science and Engineering</i> | 1977-1992 |
| <i>Nuclear Technology</i> | 1979-1992 |
| <i>Atomkernenergie</i> | where needed from references |
| <i>Atomwirtschaft</i> | where needed from references |
| <i>Nuclear Science and Technology</i> | where needed from references |
| <i>Nucleonics</i> | where needed from references |
| <i>Progress in Nuclear Energy</i> | Proceedings of <i>SMORN II, III, IV and V</i> , else: where needed from references |
| <i>Transactions of the American Nuclear Society</i> | where needed from references |

For simple problems, the detector response can be calculated analytically; a neutron diffusion or transport code can be used for complex problems (Van Dam 1976, 1977). With the analysis of a homogeneous system with two-group diffusion theory, it was found that the field-of-view is indeed composed of two components: a global and a local component (see also Behringer *et al.*, 1977). A density fluctuation affects the neutron level of the complete core through the global component. With this effect, the perturbation of the flux is propagated through the core by the fission chain and diffusion, and can be detected everywhere. The local component accounts for effects which directly influence the detector signal, like a lower thermal flux due to a lower moderator density. These effects are limited to a few centimetres. The field-of-view also depends on the frequency of the fluctuation. This can be understood by noting that low frequency fluctuations cause reactivity changes that influence the power of the complete reactor. High frequency fluctuations, however, are attenuated when transported through the fission chain, but do influence the detector signal through the local component. For a detailed treatment of the frequency dependence of the field-of-view, and the calculation of the field-of-view with the use of a diffusion code, see Van der Hagen *et al.* (1992b).

Fuge *et al.* (1977) found further support for the local/global noise theory from measurements on a critical reactor. These experiments were theoretically verified by Valkó and Meskó (1977). Kleiss and Van Dam (1979) verified the theory's predictions

by performing measurements on a subcritical set-up. In this paper, different calculated effects of an air bubble on the detector signal (thermal and fast absorption and diffusion, and thermalization) are visualized. The calculations were in agreement with the measurements. Mingchang and Gouzhen (1981) also gave further experimental support for the local/global noise concept.

From the two-group diffusion analysis of the field-of-view of an in-core detector for a homogeneous system it follows that the field-of-view of the detector for the local component can be approximated by an exponentially decreasing sensitivity. In water moderated reactors, the relaxation length is close to the thermal diffusion length, and the largest effect of a steam bubble is through the change in thermalization. Many papers on this type of analysis of the field-of-view were published. Some authors combined neutronic analysis with a model for the two-phase flow density fluctuations (Van Dam, 1976; Kosály and Meskó, 1976; Behringer *et al.*, 1977; Behringer *et al.*, 1979; Difilippo and Otaduy, 1980a; Kosály *et al.*, 1982a; Miteff and Behringer, 1982). Analytis (1980, 1982a) and Pázsit (1981) studied the influence of the number of energy groups in the analysis of the field-of-view. It was found that the magnitude of the relaxation length depends on the number of energy groups used to calculate the field-of-view, but the order of magnitude is the same in all cases.

When the field-of-view was calculated for heterogeneous problems, some different results were found. Sweeney (1979) performed one-dimensional, four-group transport calculations for a heterogeneous system. It was concluded that not the thermalization is the most important effect, but that '...the local effect may be treated as a fixed-source shielding problem with a fluctuating coolant density (attenuation noise).' This conclusion was supported by Sweeney and Robinson (1980) and Difilippo (1980b). The same conclusion was drawn by Analytis (1981, 1982b) and Difilippo (1982), who analysed heterogeneous systems with the Feinberg-Galanin method (see also Analytis, 1982c, 1982d, 1983a, 1983b; Difilippo, 1984).

In this period, not only the switch was made from homogeneous to heterogeneous systems, but also transport analysis was applied (Sweeney, 1979; Sweeney and Robinson, 1980; Kosály and Sanchez, 1982b, 1985; Haghghat and Kosály, 1985), multi-dimensional and multi-group analyses were performed, the influence of fuel homogenization was investigated (Haghghat and Kosály, 1985), and the applicability of the Feinberg-Galanin method was questioned (Kosály and Sanchez, 1985). Also, the dependency of the field-of-view on the void fraction (or axial detector-position), and the importance of the different sub-channels (see Fig. 2) in the sensitivity volume were investigated.

Because of the different methods used, this period is characterized by a rapid succession of changing results and opinions. However, the period seems to be concluded by the rigorous work of Haghghat and Kosály (1985, 1989) and Haghghat (1986). They studied the effects of both homogenization and the use of transport/diffusion analysis on the result of the field-of-view. Transport and diffusion calculations were performed for a quarter of a fuel bundle at different levels of homogenization. As only the relative sensitivity of the detector to density fluctuations in each subchannel is important, the calculated field-of-view parameters were averaged over each subchannel, and the sensitivity distribution was normalized to the sensitivity of the detector to fluctuations in the corner subchannel. By comparing the calculated field-of-view from different kinds of calculations, it was found that a so-called cell homogeneous bundle diffusion calculation (in which each subchannel is homogenized) is sufficient for calculating the field-of-view. From the calculations it also followed that, although the corner subchannels are closest to the detector, the sensitivity of the detector to density fluctuations in the side subchannels is greatest, followed by the sensitivity to fluctuations in the central and corner subchannels. This is due to the fact that not only the area of the corner subchannels is smaller than that of the side and central subchannels, but also because there are more side and central subchannels than corner subchannels. Furthermore, it was found that the field-of-view slightly increases with increasing void fraction. Finally, as opposed to the results of some investigations in the years 1979-1982 (see above), it is concluded that the most important effect of a water density fluctuation on the detector signal is due to the fluctuation of the thermalization - as was found already in 1976 (Van Dam, 1976).

The research performed since 1975 has resulted in a solid method for calculating the fluctuation of the count rate $\delta R(\omega)$ of a neutron detector to an arbitrary fluctuation of the density $\delta\rho(r, \omega)$:

$$\begin{aligned} \delta R(\omega) &= \iiint dV dE d\Omega \Sigma_d(r, E) \delta\varphi(r, \omega, E, \Omega) = \\ &= \iiint dV dE d\Omega \psi(r, \omega, E, \Omega) \frac{\partial A}{\partial \rho} \varphi(r, E', \Omega') \delta\rho(r, \omega) , \end{aligned} \quad (4-1)$$

where ω is the angular frequency, $\Sigma_d(r, E)$ is the macroscopic detector cross-section, $\varphi(r, E, \Omega)$ is the neutron flux density. Note that the operator A , which is formed by the diffusion or transport operator, is a function of the neutron energy E and direction Ω , and operates on E' and Ω' . $\psi(r, \omega, E, \Omega)$ is a complex importance function, thus containing both amplitude and phase information. This function is the solution of the

equation defined by the adjoint of the operator A and a 'source' $\Sigma_d(\mathbf{r}, E)$, the macroscopic cross-section of the detector. The integral with respect to the position is taken over the core volume. For further details and derivation, the reader is referred to literature (Van Dam, 1976, 1977). The density fluctuation $\delta\rho(\mathbf{r}, \omega)$ causes a fluctuation in the local scattering and absorption, which is accounted for by the combination of the partial derivative of A and the term $\delta\rho(\mathbf{r}, \omega)$. The effect of this change in transport and absorption on the count rate of the detector depends on the neutron flux at the position of the fluctuation, and the importance function $\psi(\mathbf{r}, \omega, E, \Omega)$, which accounts for effects like the distance between the fluctuation and the detector, the energy and direction of the neutrons, and the frequency of the fluctuation. By defining a weight function

$$w(\mathbf{r}, \omega) \equiv \int \int dE d\Omega \psi(\mathbf{r}, \omega, E, \Omega) \frac{\partial A}{\partial \rho} \varphi(\mathbf{r}, E', \Omega') , \quad (4-2)$$

Eq. (1) can be rewritten as

$$\delta R(\omega) = \int dV w(\mathbf{r}, \omega) \delta\rho(\mathbf{r}, \omega) . \quad (4-3)$$

The calculation of the expected noise signal from a given density noise source distribution involves integrating all density noise sources, weighted with the weight function $w(\mathbf{r}, \omega)$, over the core volume. When analysing a detector signal, however, the characteristics of the distributed density fluctuations are to be obtained from the measured signal. Without *a priori* knowledge of the characteristics of the density fluctuations, it is not always possible to perform this deconvolution. This problem is encountered in another form later in this chapter.

Fluctuations in two-phase flow

In 1959 it was observed that boiling near a neutron detector causes fluctuations in the detector signal (Boyd, 1959). It was found that the detector noise strength increased with increasing boiling intensity. In a BWR, however, not only the boiling intensity varies along the height of the core, but also steam is transported upwards. Measurements of neutron detector noise in a BWR show that the normalized detector noise strength (NRMS, σ_0) increases along the height of the core (Seifritz, 1972; Seifritz and Cioli, 1973). Given this increase in NRMS with void fraction, Kosály *et al.* (1975) developed the following theoretical model for the NRMS of a neutron detector as a function of the void fraction α and the average steam velocity v , which can both be a function of the axial detector-position z :

$$\sigma_0^2(z) = m \frac{\alpha(z)}{v(z)} + C, \quad (4-4)$$

where m and C are constants.

In this model, the steam bubble spectrum is assumed to be white. For the neutronic transfer of the fluctuations to the detector signal, the fluctuations are filtered by two filters: one caused by the finite detector length, and one due to the finite sensitivity volume (Kosály and Meskó, 1976; Van Dam, 1976; see also Wach, 1973; Wach and Kosály, 1974). Kosály *et al.* (1975) successfully applied the model, which is applicable at a low void fraction only, to measurements with a void fraction up to 30 %. As expected, the measurements deviate from the theoretically predicted behaviour above 30 %. Kozma (1992a) developed theoretical models for higher void fractions, one based on Bernoulli statistics of bubble dynamics:

$$\sigma_0^2(z) = m\alpha(z)(1-\alpha(z)) + C, \quad (4-5)$$

and one based on the dynamics of a (nearly) bimodal flow. In this last model, the flow has two basic modes, but fluctuations in these modes are allowed. Both models lead to a second-order polynomial for the variance of the density fluctuations as a function of the void fraction. For both models, the NRMS reaches a maximum at some value of the void fraction. Kozma (1992a) applied both the model of Kosály *et al.* (1975) and the model based on Bernoulli statistics to measurements on a simulated MTR-type fuel assembly (MTR=Material Testing Reactor). It was found, that the latter gives a better description of the void fraction fluctuations at higher void fraction. It should be noted that the thermal hydraulics of the narrow rectangular coolant channels of an MTR-type assembly is very different from the thermal hydraulics of a BWR bundle.

Ceelen *et al.* (1976) drew up a theoretical model from the following physical considerations: the density noise is due to the void fraction itself, and the growth of the void fraction (the formation of bubbles). These considerations lead to:

$$\sigma_0(z) = c \left\{ \alpha^2(z) + g \left[\frac{\Delta\alpha(z)}{\Delta z} \Delta z \right]^2 \right\}, \quad (4-6)$$

where c and g are constants. This model was applied to measurements performed at the Lingen BWR. The model gave a good description of the NRMS-measurements, which showed a local maximum at the lower half of the core.

Starting from the balance equations for mass and heat, Gebureck *et al.* (1977) developed a theoretical model for the void fraction fluctuations in a BWR (see also Singh and Stegemann, 1978). Fluctuations of the nuclear power density were considered

to be the driving source for the void fraction fluctuations. Degrees of freedom remaining in their model are the characteristics of this driving source. Theoretical results show that a completely uncorrelated noise source leads to unrealistic results. Comparison of the measured NRMS and the NRMS following from a numerical treatment of the problem with an exponentially decreasing correlation of the noise sources in space, leads to an estimation of the correlation coefficient. The theoretical and measured behaviour of the NRMS correspond quite well. The predicted spectrum of the void fraction fluctuations, however, deviates considerably from the measured spectrum. Gebureck *et al.* (1977) state that the model could be improved by a better simulation of the bubble generation process.

John and Singh (1980) derived an analytical expression for the mean square value of the void fluctuations in terms of the before mentioned correlation coefficient and some other process variables. The bubble generation process was also analysed by John and Singh (1983). They derived an expression for the bubble departure diameter in terms of the pressure, the flow velocity, the contact angle, and the cavity size. This bubble diameter is directly connected with the bubble generation frequency. A set of values for the bubble generation frequency is obtained through a parametric study. The frequency at which the spectrum of measured void fraction fluctuations reaches its maximum, corresponds with the theoretically predicted values.

Pauchon and Bannerjee (1986) drew up a theoretical model for void propagation in bubbly flows. With this model, they calculated the void fraction wave velocity for different experimental set-ups, liquid superficial velocities, and void fractions. The predictions were in close agreement with the measured data. The model and the measurements concern a non-heated two-phase flow. Biesheuvel and Gorissen (1990) also developed a theoretical model for void fraction wave propagation for gas/liquid bubbly flow. They studied the void propagation velocity, and the stability of bubbly flow. Measurements of the void fraction wave velocity for bubbles in stagnant water were in agreement with the model's predictions.

Hummel and Wesser (1988) performed X-ray computer tomography on two-phase flow. In the paper, the two-dimensional distribution of the first four moments of the fluctuations (mean value, variance, skewness, flatness), and the RMS value for different frequency intervals are plotted for various flow types.

Noise measurements on an out of pile set-up with an air/water two-phase flow mixture were performed by Jones and Zuber (1975). In this investigation, void fraction fluctuations were measured with a fast response X-ray void measurement system. It

was shown that the two-phase flow patterns bubbly, slug and annular flow can be recognized by analysing the probability density function of the void fraction fluctuations. From the statistical measurements, the film thickness for slug and annular flow, the slug length, and the slug residence time are calculated. The paper contains a large number of pictures of the flow, time signals, and probability density functions for a wide range of liquid and gas superficial velocities.

Albrecht *et al.* (1981, 1982) performed measurements with in-core neutron detectors near an air/water two-phase flow in a thermal column of the University of Washington nuclear reactor. A clear evolution of the probability density function for a gradual transition from bubbly to churn and slug flow is shown.

Lübbesmeyer and Leoni (1983d) performed measurements of the noise signals of light beams through an air/water flow. So-called characteristic functions (the noise signal, the probability density function, the coincidence probability function, the cross-correlation function, and the auto- and cross-power spectral density) are given in this paper for several flow regimes.

The propagation of spontaneous void fraction fluctuations in a nitrogen/water flow was experimentally studied by Matuszkiewicz *et al.* (1987). Time signals and spectra of conductivity probes are shown for void fractions ranging from 10 % to 50 % (flow regimes bubbly, churn and slug flow). Their experimental set-up also allowed for studying the development of void fraction waves for the vertical two-phase flow. The measurements show that the RMS of the void fraction increases with axial position, while the average void fraction is constant as a function of the axial position. As a function of the average void fraction, the RMS increases up to approximately 40 % void, and decreases at higher void fraction. The frequency-dependent velocity, as calculated from the phase behaviour of the cross-spectrum of two axially displaced conductivity probes, was analyzed. For low void fraction, this velocity is independent of the frequency, and increases only slightly with increasing axial position. For high void fraction, the velocity strongly depends on the frequency and the axial position. For a void fraction of 50 %, the velocity even exhibits a minimum value at some axial position. The measured velocity is different from the gas or liquid velocity. The authors connect the stability of void fraction waves to the bubble-slug transition.

The propagation of both spontaneous and induced void fraction fluctuations in a nitrogen/water flow was experimentally studied by Saiz-Jabardo and Bouré (1989). They studied the attenuation and velocity of the waves in the frequency domain as a function of the liquid superficial velocity and the void fraction. The authors conclude, that if two velocities can be measured (for instance, from two peaks in the cross-correlation

function), this can be an indication that slug flow arises.

From the list of investigations given above, it is clear that there is a strong evolution in the interpretation of measurements, and the construction of models. In the early days, neutron noise was thought to be induced by independent steam bubbles. Later, the steam bubbles were modelled as being (partly) correlated, first through the correlation of the fluctuations of the nuclear power, later through the concept of void fraction waves. Many models have been developed, but many explain only part of the measured effects, or have a questionable applicability to the two-phase flow in a nuclear reactor. The many experiments that have been performed show that the characteristics of the density noise depend on many variables, like void fraction, velocity, geometry, etc. This makes it very difficult to construct a general model, or to perform universal measurements. As most of the experiments were performed on gas-liquid flows, or on in-core set-ups (with many uncertainties as to the operating conditions), it would be desirable to perform void fraction fluctuation measurements on the two-phase flow in (simulated) fuel assemblies, like the experimental set-up described by Van de Graaf *et al.* (1994).

Two-phase flow monitoring

Velocity measurements

As outlined in the introduction to this chapter, the two-detector velocity measurement technique is based on the propagation of fluctuations of the void fraction from an upstream to a downstream detector. By applying noise analysis techniques to the detector noise signals, the transit time of the fluctuations can be estimated. The propagation velocity can be calculated by combining the transit time and the distance between the detectors. In a BWR, however, different propagation velocities exist due to the heterogeneity of the two-phase flow on subchannel and core level, and the information present in the detector noise signal has its origin in different regions. Furthermore, a relation has to be established between the measured velocity (the velocity of the fluctuations) and two-phase flow quantities like liquid and gas (superficial) velocities or volumetric flux.

Some investigators tried to solve this problem by calibration of the measured data with data from other measurement techniques (Analytis and Lübbesmeyer, 1983c; Pór *et al.*, 1984; Van der Hagen and Van der Voet, 1988a), or from two-phase flow calculations (Kosály *et al.*, 1977; Kosály, 1980; Behringer and Crowe, 1981;

Lübbesmeyer, 1983a; Khan and Kosály, 1984; Analytis and Lübbesmeyer, 1984a, 1984b, 1984c, 1985), or by performing numerical simulations (Sweeney, 1978, 1979; Lübbesmeyer, 1983b, 1984; Behringer, 1983; Analytis and Lübbesmeyer, 1983c, 1984b; Lübbesmeyer and Analytis, 1985; Kozma, 1991). The outcome of these investigations was that the velocity that follows from the measured transit time is the steam velocity (Seifritz and Cioli, 1973; Kosály *et al.*, 1977; Sweeney, 1979; Analytis and Lübbesmeyer, 1984a, 1984b, 1984c), the volumetric flux (Lübbesmeyer, 1983a, 1983c), or the void propagation velocity (Kosály, 1983). With respect to spatial effects, the measured velocity is thought to be a (weighted) bundle average quantity (literature up to ± 1983 ; Haghghat and Kosály, 1989), or the steam velocity in the side subchannel (Khan and Kosály, 1984; Analytis and Lübbesmeyer, 1984a, 1984b, 1984c).

In some cases, the phase of the cross-spectrum of the noise signals of two axially displaced in-core neutron detectors shows different slopes in different frequency regions, or the cross-correlation function shows an additional peak (Kosály *et al.*, 1977; Federico *et al.*, 1982). The transit time related to the additional peak is the so-called second transit time. The second transit time is sometimes observed in the upper half of the core, and can be explained by the influence of a radial velocity profile in the bundles next to the detector (Lübbesmeyer, 1983b; Behringer, 1983; Analytis and Lübbesmeyer, 1983d) (in case of four neighbouring bundles with a different flow pattern), or the steam velocity in the corner or inner subchannels (Analytis and Lübbesmeyer, 1984b, 1984c).

Literature on experimental and theoretical investigations on gas/liquid flows shows some other possible interpretations of the measured velocities (see *Fluctuations in two-phase flow*, page 62). The measured velocities turn out to be not identical to the gas or liquid velocity, and to be a function of the gas and liquid superficial velocity. Analysis in the frequency domain of the phase of the cross-spectrum of two axially displaced void fraction probes shows that dispersion takes place, and the analysis of the cross-correlation function shows that two propagation processes can co-exist (Matuszkiewicz *et al.*, 1987; Saiz-Jabardo and Bouré, 1989).

It is clear that the research on the propagation of void fraction waves is still developing, especially for the case of heated two-phase flow. In order to gain insight into the propagation of void fraction waves in fuel bundles, extensive measurements with local void fraction probes (like conductivity or capacitance probes) in simulated fuel assemblies are required.

The results of theoretical and experimental investigations can be combined with the detector field-of-view to form the characteristics of the neutron detector signals. From Eq. (3) it follows that the cross-power spectral density $G_{12}^d(\omega)$ of two neutron detector noise signals can be written as

$$\begin{aligned} G_{12}^d(\omega) &= \iint dV dV' w_1^*(r, \omega) w_2(r', \omega) \delta\rho^*(r, \omega) \delta\rho(r', \omega) = \\ &= \iint dV dV' w_1^*(r, \omega) w_2(r', \omega) G_{12}^c(r, r', \omega), \end{aligned} \quad (4-7)$$

where $G_{12}^c(r, r', \omega)$ is the cross-power spectral density of the void fraction fluctuations at positions r and r' and $*$ denotes the complex conjugate. The factor $G_{12}^c(r, r', \omega)$ represents the magnitude of, and the relation between, the fluctuations at r and r' , including a phase shift due to the propagation from r to r' .

In the case of a heterogeneity of the propagation process, there is a fundamental problem in obtaining the information on the propagation from the measured $G_{12}^d(\omega)$, which can only be solved if knowledge on the fluctuations, the flux, and the importance function is available. Of course, the knowledge on the fluctuations involves information on two-phase flow quantities like gas and liquid velocities and the void fraction - quantities which are to be measured.

An example of knowledge that could be used when interpreting measurements is given by the measurements of Lübbesmeyer (1983a; see also Analytis and Lübbesmeyer, 1984a, 1985). These measurements show, that, if the detector is surrounded by four bundles under different thermal hydraulic conditions, the measured velocity has its origin in the bundle with the highest flow quality. Apparently, the higher flow quality results in a stronger noise source. It is clear, however, that this result can not be universally applicable, because, at very high flow quality, the noise source strength decreases with increasing flow quality.

Other neutron noise techniques for monitoring two-phase flow

Other noise analysis techniques also prove to be useful in studying two-phase flow. For example, a well-known method is flow pattern recognition through analysis of the probability density function of the noise signal (Jones and Zuber, 1975; Albrecht *et al.*, 1982; Van der Hagen and Van der Voet, 1988a; Kozma, 1992a; Kozma *et al.*, 1992b). Lübbesmeyer and Leoni (1983d) present a set of so-called characteristic functions which can be used for flow pattern recognition. King *et al.* (1988, 1989) studied the possibilities of flow pattern recognition with the use of auto-regressive/moving average modelling. The so-called dynamic signature, which is the variance of the neutron noise,

relative to the variance of the residual noise, proves to be an indicator for the flow type. Wang *et al.* (1988, 1990) studied the same problem by analysing the ratio of the power of the high and the low frequency part of the noise signal.

Furthermore, the neutron noise technique offers the possibility of boiling detection (Bernard *et al.*, 1982; Behringer *et al.*, 1985; Katona, 1985; Hoogenboom *et al.*, 1985; Katona and Kozma, 1988; Defloor and Baeyens, 1988; Pór *et al.*, 1988; Kozma, 1992a).

Although many of these methods prove to be (partly) successful, they all could be improved if more knowledge was available on the physical processes involved in density fluctuations in two-phase flow. Furthermore, also these techniques suffer from the same localization problem as already encountered previously in this chapter. Two-phase flow conditions are not only to be detected, but also to be pinpointed. Besides, different two-phase flow conditions near the detector might obscure the results of the detection. Finally, there is a problem in finding suitable locations for in-core detectors in order to cover the complete core region with a monitoring system.

Example: distribution of the in-core neutron detector noise

The following measurements, which were performed at the Dodewaard BWR, illustrate the space dependence of the in-core neutron noise due to the space dependence of density fluctuations, and show the possibilities of monitoring two-phase flow with a single in-core detector. At the three radial TIP-positions 5C, 6B and 6D, neutron noise measurements were performed at five heights for the lower 25 % of the core height (see Fig. 1-3 for TIP-positions). Figure 3 shows the spectra of the neutron noise signals for five heights for radial position 5C. The spectra are normalized to the strength of the global component of the neutron noise (low frequency part; 0-3 Hz). In this way, the change in the high frequency region as a function of the detector height is clearly visible. The plot shows an increase in amplitude of the high frequency part of the signal (>5 Hz) with detector height. This is due to the increase of the amplitude of the density fluctuations as the void fraction grows with higher elevation. This effect is studied more closely by calculating the high frequency contribution relative to the low frequency part. In Fig. 4 the ratio of the mean square values of the high and low frequency part are plotted as a function of the height for the three different radial positions. This figure shows several features:

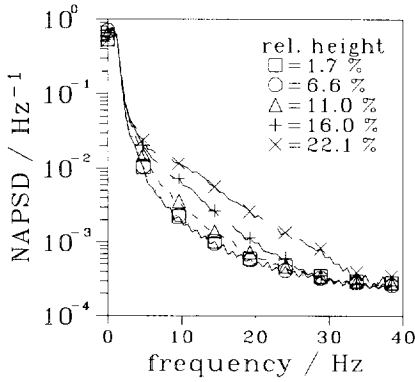


Figure 4-3. Normalized auto-power spectral density of the in-core neutron detector noise signal for various axial positions at radial position 5C

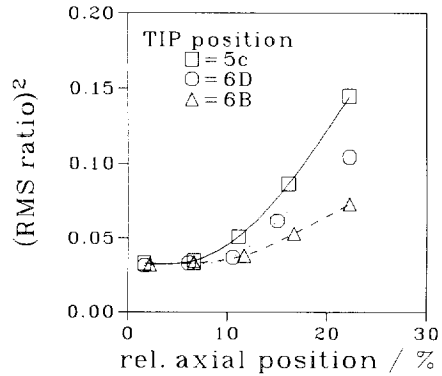


Figure 4-4. Ratio of the high and low frequency contribution to the detector noise signal as a function of the axial position of the detector for three radial positions

- for very low elevations, the noise strength ratio is constant, and equal for the three radial positions;
- in the region considered here (lower 25 % of the core), the high frequency contribution grows with the height. The gradient is different at the three radial positions;
- in the small region 5-10 %, the contribution suddenly increases. The axial position at which there is this sudden increase is different for the radial positions considered here.

From the last two observations it can be concluded that the thermohydraulic conditions are different at the three radial positions. A higher slope of the curve and a lower transition point indicate a higher power and/or a lower flow rate.

For a quantitative analysis of these measurements the model of Kosály *et al.* (1975), Eq. (4), for the relation between the measured NRMS-value and the two-phase flow variables α and v is applied. As an approximate solution to the deconvolution problem stated earlier in this chapter, only the bundle with the largest power production of the four bundles surrounding the detector is considered in the analysis, as this bundle is likely to have the largest noise source contribution. With the use of the void-quality-slip relation (Todreas and Kazimi, 1990a)

$$\alpha = \frac{\chi}{(1-\chi)S\frac{\rho_g}{\rho_l} + \chi}, \quad (4-8)$$

where χ is the flow quality, ρ_g and ρ_l are the steam and water density respectively, and S is the slip factor between the two phases, and

$$\chi(z) = \frac{I(z) - (h_{sat} - h_{ci})\phi}{\Delta h_{gl}\phi}, \quad (4-9)$$

where z is the axial position, h_{ci} and h_{sat} are the specific enthalpies of water at the inlet of the core and at saturation temperature respectively, Δh_{gl} is the heat of evaporation, ϕ is the bundle flow rate, and $I(z)$ is the integral of the linear power q' from the bottom of the core to the detector height

$$I(z) = \int_0^z q'(z') dz', \quad (4-10)$$

the following expression can be derived

$$\frac{\alpha}{v} = \frac{(I - (h_{sat} - h_{ci})\phi)A\rho_g\Delta h_{gl}}{\left[I - (h_{sat} - h_{ci})\phi + S\frac{\rho_g}{\rho_l}\Delta h_{gl}\phi \right]^2}. \quad (4-11)$$

In the right-hand-side of this expression, only I varies substantially as a function of the axial position (the relative variation of the slip is much smaller). In principle, when this expression is substituted into Eq. (4), the integrated linear power as a function of the axial position can be calculated from the measured NRMS-distribution, and given values for the constants in the expressions. Likewise, some of the parameters can be estimated by combining the NRMS-measurements with a given integrated linear-power distribution. The latter application is demonstrated below.

For low flow quality, Eq. (11) can be approximated by

$$\frac{\alpha}{v} \approx \frac{(I - (h_{sat} - h_{ci})\phi)A\rho_g\Delta h_{gl}}{\left(S\frac{\rho_g}{\rho_l}\Delta h_{gl}\phi \right)^2}. \quad (4-12)$$

Through this expression, the NRMS is a linear function of the integrated linear power. In Fig. 5 the integrated linear power for the bundles with the largest power next to the TIP-positions, obtained from calculated power distributions (Wouters, 1992d), is

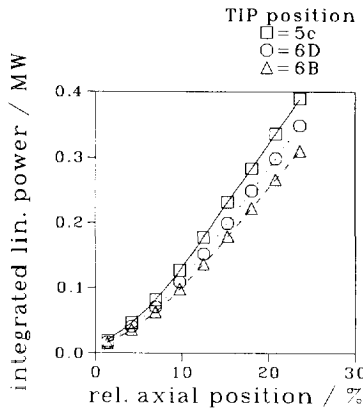


Figure 4-5. Integrated calculated linear power for the bundle with the largest power next to the TIP-positions as a function of the axial detector position

plotted. The figure shows that the integrated linear power is, approximately, a linear function of the axial position for heights above 10 %. The combination of these two linear functions leads to the conclusion that the NRMS is a linear function of the axial position, which is in accordance with Fig. 4 for heights above 10 %.

When $I(z)$ is modelled as

$$I(z) = az + b \quad (4-13)$$

in which a and b are constants following from Fig. 5, Eqs. (12) and (4) can be combined to form

$$\sigma_0^2 = \frac{A \rho_g \Delta h_{gl} m a}{(S \frac{\rho_g}{\rho_l} \Delta h_{gl} \phi)^2} z + C' \quad (4-14)$$

where C' is a constant. It is important to note that in this expression A , ρ_g , ρ_l , Δh_{gl} , and m do not depend on the radial position, S only weakly depends on the radial position, and a and ϕ depend on the radial position. By estimating a from Fig. 5 for the different radial positions, and the ratios of the slopes of the curves in Fig. 4, the ratios of the flows in the bundles with the largest power near the three TIP-positions can be calculated. This results in the following estimations of the flow ratios: $\phi_{6D}/\phi_{5C} = 1.16$, $\phi_{6B}/\phi_{6D} = 1.25$, and $\phi_{6B}/\phi_{5C} = 1.46$.

In this application, the RMS-value calculated from the frequency region 5-30 Hz was analyzed (normalized with respect to the RMS calculated from the frequency region 0-3 Hz). An assumption in the model of Kosály *et al.* (1975) is that the noise spectrum

is white. For this reason, the analysis presented above should also be applicable to other frequency regions. The flow ratios following from an analysis for 5-10 Hz and 10-15 Hz lie within $\pm 6\%$ of the above-mentioned flow ratios. For higher frequencies, the RMS-ratio as a function of the axial position is non-linear. For this reason, the simple method presented above cannot be applied. Furthermore, this indicates that the boiling noise spectrum is not white, which can also be seen from Fig. 3, as the increase of the noise level for increasing axial position depends on the frequency. The conclusion that the density noise in two-phase flows is not white is supported by literature (John and Singh, 1983; Matuszkiewicz *et al.*, 1987; Saiz-Jabardo and Bouré, 1989).

As the assumption of the white noise spectrum is vital for the derivation of the model, Eq. (4), the application of the model to the measurements presented in Figs. 3 and 4 is questionable. For this reason, the above-mentioned flow ratios have a large uncertainty. Thermal hydraulic/neutronic calculations give the following results (Wouters, 1992d): $\phi_{6D}/\phi_{5C}=1.04$, $\phi_{6B}/\phi_{6D}=1.02$, and $\phi_{6B}/\phi_{5C}=1.06$. The calculated and the measured/calculated results show a large discrepancy, but at least agree on the statement that $\phi_{6B} > \phi_{6D} > \phi_{5C}$.

Although the results of the analysis presented above are questionable, the analysis demonstrates that with a suitable model, and a combination of calculated and measured data, parameters can be estimated from in-core neutron detector noise measurements. In order to obtain reliable results from such an analysis, the development of a solid theoretical model for the characteristics of the density noise in two-phase flows is vital.

Conclusions

A study of literature on the possibilities of measuring local two-phase flow conditions in a BWR with the use of in-core detector noise signals was performed. It was found that the neutronics involved in neutron noise measurements is quite well understood. The development in this field is characterized by many discussions and opinions, but a consensus seems to be reached. Furthermore, with the present calculational resources, the methods and results presented can be quite easily verified.

The physical processes governing the density fluctuations, which cause the neutron flux perturbations, are less well-understood. Theory on fluctuations in two-phase flow has to be improved, especially for heated two-phase flows. The field of investigation of the propagation of void fraction waves is still developing. Extensive measurements in simulated fuel bundles have not yet been performed.

For a detailed analysis of the measured neutron noise signal, a deconvolution of the

noise signal into separate contributions has to be performed. This involves knowledge on the detector field-of-view, as well as information on the distributed density fluctuations, i.e. *a priori* knowledge on the two-phase flow conditions. However, for a limited number of practical applications, some information on the two-phase flow characteristics can be extracted from in-core neutron detector noise signals through a smart use of knowledge of the neutron flux, the importance of the fluctuations, and the fluctuations themselves. In this way, the analysis of in-core neutron detector noise signals can be a very useful tool for studying local two-phase flow conditions, thus providing information for the calculation of important local quantities like bundle peaking factor, DNB-ratio and rod burn-up.



chapter 5

A theoretical model for the reactor dynamics

Introduction

In chapters 2 and 3, a method for estimating the circulation flow rate from downcomer thermocouple noise signals is presented. As discussed in chapter 4, the noise signals of in-core detectors provide information on the in-core two-phase flow conditions. With these measurement techniques, and the readings of numerous plant sensors, the behaviour of the Dodewaard BWR under various conditions is studied. In spite of the extensive measurement data, gaining insight into the behaviour can still be difficult due to the following reasons:

- some reactor parameters, like void fraction, carry under and reactivity, cannot be measured directly;
- the conditions at which measurements can be performed are restricted by the technical specifications of the power plant;
- some of the measurement techniques, including the circulation flow rate measurement technique, have a large response time, which excludes them from being used for studying dynamical behaviour.

In order to increase the insight into both the statical and the dynamical behaviour of natural circulation cooled BWRs, analytical and numerical studies can be performed. The type of the study and the tools to be applied depend on the results required. Sophisticated computer codes are available for reliably calculating stationary reactor conditions, or simulating slow as well as fast transients. In the study presented in this thesis, however, the emphasis is on the understanding of the interaction of the physical processes involved, rather than on the reliability of the numerical results of the

simulations. It is required that the analysis tool applied provides a roughly correct estimate of the reactor behaviour, that the model is clear, and that the tool allows parameter studies to be performed easily. Therefore, it was decided to draw up a simple theoretical model of the main physical processes involved, and to write an easy-to-use computer program to solve the model equations and to simulate the reactor behaviour. In this chapter, the model is presented, together with the model parameters and a short description of the simulator program.

In chapters 6 and 7, the results of measurements and simulations of the statical and dynamical behaviour of the reactor are both discussed and compared, and the reactor behaviour is analysed with the use of the simulator program.

Theoretical model

Introduction

The physical processes taken into account in the modelling are drawn schematically in Fig. 1. In Fig. 2 the dimensions of the main sections in the reactor vessel are indicated. The theoretical model is presented, starting with the model for the nuclear reactor kinetics, followed by the fuel temperature dynamics. Next, the models for the processes encountered when following the coolant flow from the core inlet, through the core and riser and back through the downcomer channel, are discussed. Finally, the models for the remaining processes are presented. Basically, the mass, energy and momentum conservation equations are stated for each section. Regarding the momentum, however, only the largest friction and acceleration terms in the circulation flow loop are considered. These terms are the friction of the core flow (both single- and two-phase flow) and the acceleration due to the steam production in the core. Because of the large uncertainty of the magnitude of the actual bypass flow rate, the bypass flow is not taken into account in the modelling.

The flow in the core, the riser, the downcomer channel, and the lower plenum is modelled in one dimension, the flow direction, only. This implies that the radial distribution of the flow in these sections is not taken into account. Furthermore, these sections, except for the core region, are modelled with averaged quantities and transport delays. The core flow, which is subcooled in the lower part of the core and saturated in the upper part of the core, is modelled with two nodes: one for the subcooled and one for the saturated part. For the complete core, the axial power distribution is modelled as a sinusoidal distribution superimposed on a uniform distribution. From this power distribution, the power in the subcooled node and the saturated node is

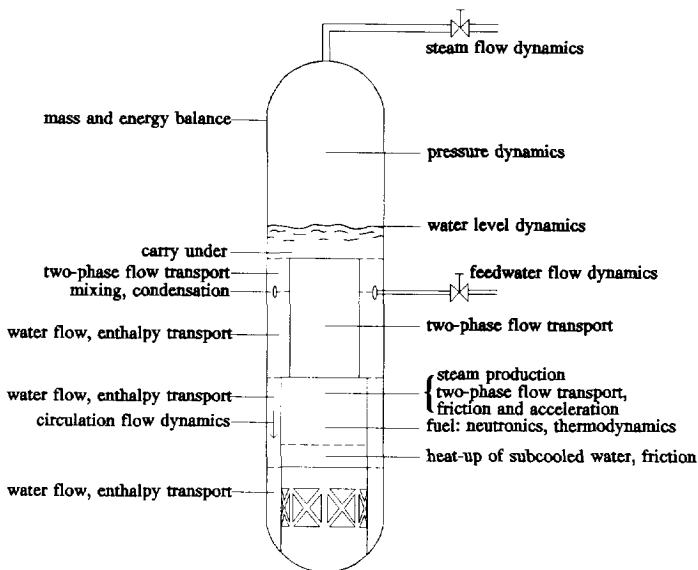


Figure 5-1. Schematic view of the main physical processes in the Dodewaard reactor vessel

calculated. Within these two nodes, the power production is taken uniformly.

The values of some parameters, in particular the parameters which involve fluid flow, are a result of processes which are distributed in both space and time. As space dependence within the nodes is not taken into account explicitly in the model, effective values are calculated by separating the space and time behaviour. For calculating these values, all processes involved are assumed to be stationary, and the values of some of the parameters involved are taken at the time at which the flow has travelled half the section. For example, the flow quality at the exit of the core is a result of the time-dependent power production and the transport of the two-phase flow through the core. In the model, the exit quality is calculated from an expression like (assuming, for simplicity, that temperature of the water entering the core is saturation temperature)

$$\chi_{co}(t) \approx \frac{1}{\Delta h_{gl} \phi_i} \int_0^{l_c} q'(z, t - \frac{1}{2} \tau_c) dz, \tag{5-1}$$

where χ_{co} is the core exit flow quality, Δh_{gl} is the heat of evaporation of water, ϕ_i is the core mass flow rate, q' is the linear power, z is the height, τ_c is the transit time for the core, and l_c is the length of the core. Implications of this modelling are illustrated with the examples plotted in Fig. 3. In these examples, the influence of a step increase and

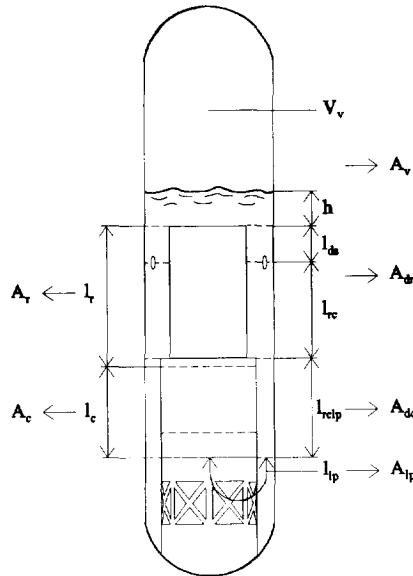


Figure 5-2. Dimension parameters of the main sections in the Dodewaard reactor vessel

a step decrease of the (in these examples uniform) linear power on the exit flow quality is analyzed. Second order effects, like the change in the flow velocity due to the change in the flow quality, are not taken into account in this example. The plots show that the estimated exit quality deviates from the actual exit flow quality for a time interval of length τ_c . The magnitude of the deviation depends on the magnitude on the step change. Generalizing the last two conclusions, it can be stated that the accuracy of the estimations depends on the transit times and the rate at which the variables being integrated vary in time. In this respect, it is important to note that the time scale of interest in this study runs from the order of one second.

In many of the expressions that follow, the time dependence is omitted for simplicity. In these expressions, the variables are taken at time t , unless stated otherwise.

Neutron kinetics

The neutron kinetics is modelled by the point reactor kinetics equations (Duderstadt and Hamilton, 1976). In this model, spatial effects are not considered explicitly. As the maximum value of the reactivity that arises during normal operation is much smaller than the fraction of delayed neutrons, and in view of the time scale of interest, the

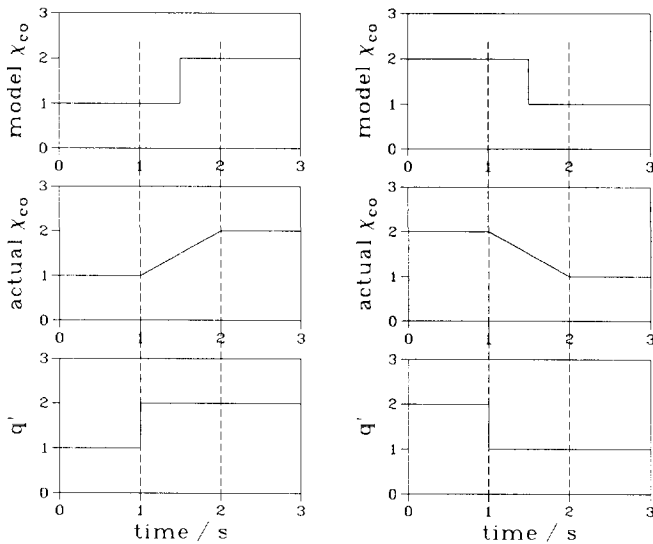


Figure 5-3. Examples to demonstrate the modelling of transport phenomena (see text)

prompt jump approximation can be applied (Duderstadt and Hamilton, 1976; see also Goldstein and Shotkin, 1969), leading to

$$P(t) = \frac{\Lambda}{\beta - \rho(t)} \sum_{i=1}^6 \lambda_i C_i(t) \tag{5-2}$$

$$\frac{dC_i}{dt} = \frac{\beta_i}{\Lambda} P(t) - \lambda_i C_i(t) , \tag{5-3}$$

where $P(t)$ is the nuclear power, Λ is the neutron generation time, β is the fraction of delayed neutrons, $\rho(t)$ is the reactivity, λ_i is the decay constant of neutron precursor group i , $C_i(t)$ is a parameter which is proportional to the concentration of neutron precursors in group i , and β_i is the fraction of delayed neutrons of group i . The reactivity is split into five terms:

- the constant base reactivity ρ_0 . This reactivity is given such a value that the reactor is critical ($\rho=0$) at the initial condition (see the section *initial conditions*);
- the external reactivity ρ_{ext} . This is an independent reactivity for simulating, for example, the control rods;
- the moderator/coolant temperature reactivity ρ_T . The temperature of the water in the core affects the density of the water. As the water in the core acts as a moderator for the neutrons, a change in the water density leads to a change in the reactivity.

The coolant temperature reactivity is modelled as a linear function of the saturation temperature T_{sat} (most of the water in the core is at saturation temperature)

$$\rho_T(t) = r_T T_{sat}(t) , \quad (5-4)$$

where r_T is a constant;

- *the fuel temperature reactivity* or *Doppler reactivity* ρ_D . The fuel temperature influences the resonance absorption of neutrons in the fuel through the Doppler effect. The resulting reactivity effect is modelled as a linear function of the fuel temperature T_f

$$\rho_D(t) = r_D T_f(t) , \quad (5-5)$$

where r_D is a constant;

- *the void reactivity* ρ_α . The void fraction affects the reactivity, as the void fraction is directly coupled to the density of the moderator. Neutronic calculations of the void reactivity effect show that the reactivity as a function of the void fraction can be represented by a second order polynomial in the void fraction (Kleiss, 1982). As the void fraction varies as a function of the height, the void reactivity is modelled as a function of the average void fraction $\langle \alpha_c \rangle$ and the mean square value of the void fraction $\langle \alpha_c^2 \rangle$

$$\rho_\alpha(t) = r_{\alpha 1} \langle \alpha_c(t) \rangle + r_{\alpha 2} \langle \alpha_c^2(t) \rangle , \quad (5-6)$$

where $r_{\alpha 1}$ and $r_{\alpha 2}$ are constants.

The net reactivity is the sum of the above-mentioned reactivity effects

$$\rho(t) = \rho_0 + \rho_{ext}(t) + \rho_T(t) + \rho_D(t) + \rho_\alpha(t) . \quad (5-7)$$

Fuel temperature dynamics

The fuel temperature dynamics is described by a lumped parameter model. In the model, heat transfer in axial direction is not considered. Furthermore, it is assumed that the coolant temperature is equal to the saturation temperature for the complete length of the fuel, which is a reasonable approximation since the subcooling is only of the order of 4 K, and $T_f \gg T_{sat}$. The core average linear heat rate $\langle q'(t) \rangle$ from fuel rod to coolant is

$$\langle q'(t) \rangle = 2\pi R_f \alpha_f (T_f(t) - T_{sat}(t)) , \quad (5-8)$$

where R_f is the radius of the fuel rods, and α_{fc} is the fuel to coolant heat transfer coefficient. The energy balance for the fuel reads

$$\frac{dT_f}{dt} = \frac{P(t)}{\rho_f c_{pf} V_f} - \frac{1}{\tau_f} (T_f(t) - T_{cool}(t)) , \quad (5-9)$$

where ρ_f , c_{pf} , V_f are the density, the specific heat capacity, and the volume of the fuel respectively, and τ_f

$$\tau_f = \frac{\rho_f c_{pf} V_f}{\alpha_{fc} A_f} , \quad (5-10)$$

is the fuel time constant (El-Wakil, 1978). Usually, τ_f is not calculated from Eq. (10), but it is estimated from an experimental or theoretical analysis of the response of the fuel temperature to nuclear power variations (Van der Hagen, 1988c). In this way, the single time-constant model is tuned to approximate the behaviour of the more complex reality.

In the previous section, the nuclear power production is modelled as a single quantity - the three-dimensional distribution of the power production is not taken into account explicitly. In reality, the power production is lowest at the top and the bottom of the core, and has its maximum value close to the middle of the core. In the model for the linear heat rate from fuel to coolant (with Eq. (8) as a starting-point), this axial distribution of the nuclear power is modelled by a sine-function, superimposed on a constant, for the linear heat rate $q'(z,t)$

$$q'(z,t) = q_0'(t) + q_1'(t) \sin\left(\frac{\pi z}{l_c}\right) , \quad (5-11)$$

where l_c is the length of the active fuel, z is the axial position, and q_0' and q_1' are constants that follow from the axial peaking factor f_p

$$f_p = \frac{q_0' + q_1'}{\langle q' \rangle} \quad (5-12)$$

and the normalization

$$\langle q' \rangle = q_0' + \frac{2q_1'}{\pi} . \quad (5-13)$$

Lower part of the core with single-phase flow

The water enters the core at a time-varying temperature below saturation temperature. The height at which saturation temperature is reached is calculated from

$$\int_0^{f_{nb}l_c} q'(z, t - \tau(z)) dz = (h_{sat} - h_{ci}) \phi_t, \quad (5-14)$$

where this point is expressed as a fraction f_{nb} of the core length, h_{sat} is the specific enthalpy of water at saturation conditions, h_{ci} is the specific enthalpy of the water at the core inlet, and ϕ_t is the total core coolant mass flow rate. The subscript nb denotes the non-boiling section. The time variable was omitted for simplicity.

For the stationary case, this equation is a transcendental equation for the variable f_{nb} . Because f_{nb} is small, the resulting cosine from the integration can be adequately approximated by a Taylor series expansion of the second order, leading to

$$f_{nb} \approx \frac{-q'_0 l_c + \sqrt{q'_0{}^2 l_c^2 + 2\pi q'_0 l_c \phi_t (h_{sat} - h_{ci})}}{\pi q'_0 l_c} \quad (5-15)$$

For an estimation of $f_{nb}(t)$, h_{sat} is taken at time t . Because of the water transport, q' , and ϕ_t are taken at time $t - 1/2 \tau_{nb}$, where τ_{nb} is the transit time for the non-boiling section, and h_{ci} is taken at time $t - \tau_{nb}$ (see the discussion in the introduction to the section **Theoretical model**).

The transit time for the non-boiling section is calculated from

$$\tau_{nb}(t) = \frac{f_{nb}(t) l_c \rho_f(t) A_c}{\phi_t(t)}, \quad (5-16)$$

where $\rho_f(t)$ is the water density (taken at saturation conditions for simplicity), and A_c is the cross-sectional flow area of the core.

The frictional pressure drop for the non-boiling section of the core Δp_{nb} is calculated from a function Δp_c , which describes the friction of two-phase flow through the core as a function of flow quality χ , water density, mass flow rate, and the pressure p ,

$$\Delta p_{nb} = f_{nb} \Delta p_{cf}(\chi, \rho_f, \phi_t, p), \quad (5-17)$$

with $\chi=0$, and all variables at time t . The function Δp_{cf} is presented below.

Subcooled boiling is not modelled.

Part of the core with two-phase flow

The part of the core height (fraction f_b) in which saturated boiling takes place is

$$f_b(t) = 1 - f_{nb}(t) . \quad (5-18)$$

The power P_b produced in this part is (again making use of the second order Taylor series expansion of the cosine-function)

$$P_b \approx f_b l_c q_0' + \left(\frac{2}{\pi} - \frac{1}{2} \pi f_{nb}^2 \right) l_c q_1' . \quad (5-19)$$

The core exit flow quality χ_{co} is calculated from

$$\chi_{co} = \frac{P_b}{\Delta h_{gl} \phi_t} , \quad (5-20)$$

where Δh_{gl} is the specific heat of evaporation. In this expression, P_b and ϕ_t are taken at time $t - 1/2 \tau_b$, with the transit time τ_b for the boiling section to be defined below.

The axial volumetric void fraction distribution $\alpha(z)$ is modelled by the homogeneous equilibrium model of two-phase flow (Todreas and Kazimi, 1990a), which reads for the stationary case

$$\alpha_c(z) = \frac{\chi_c(z)}{(1 - \chi_c(z)) \frac{\rho_g}{\rho_l} + \chi_c(z)} , \quad (5-21)$$

where ρ_g is the steam density. In this model it is assumed that the water and steam velocity are equal, and that both phases are in thermodynamic equilibrium.

When a uniform linear heat rate for the boiling section is assumed (with a total power of P_b), χ_c is a linear function of z , ranging from 0 to χ_{co} . The core average void fraction $\langle \alpha_c \rangle$ is calculated by integrating Eq. (21) over the core height, resulting in

$$\langle \alpha_c \rangle = \frac{f_b}{\chi_{co} \left[1 - \frac{\rho_g}{\rho_l} \right]^2} \left\{ \left[1 - \frac{\rho_g}{\rho_l} \right] \chi_{co} - \frac{\rho_g}{\rho_l} \ln \left[\frac{\rho_l \chi_{co}}{\rho_g \alpha_{co}} \right] \right\} . \quad (5-22)$$

The mean square value of the void fraction is needed in Eq. (6). This quantity is calculated in the same way as α_c , but now taking the square of $\alpha_c(z)$ before performing the integration

$$\langle \alpha_c^2 \rangle = \frac{f_b}{\chi_{co} \left[1 - \frac{\rho_g}{\rho_l} \right]^3} \left\{ \frac{\chi_{co}^2 \rho_l^2 - \alpha_{co}^2 \rho_g^2}{\chi_{co} \alpha_{co} \rho_l^2} - \frac{\rho_g}{\rho_l} \ln \left[\frac{\rho_l \chi_{co}}{\rho_g \alpha_{co}} \right] \right\}. \quad (5-23)$$

The total pressure drop for the boiling section can be expressed as the sum of the three components due to acceleration, friction and gravity. Form losses are not considered - this effect, which only arises at definite heights (inlet, spacers, etc.) is modelled to be spread over the core height, and is included in the friction term. The pressure drop due to acceleration Δp_{ca} is (Todreas and Kazimi, 1990a)

$$\Delta p_{ca} = \left[\frac{\phi_l}{A_c} \right]^2 \left[\frac{(1 - \chi_{co})^2}{(1 - \alpha_{co}) \rho_l} + \frac{\chi_{co}^2}{\alpha_{co} \rho_g} - \frac{1}{\rho_l} \right]. \quad (5-24)$$

The frictional pressure drop for the boiling section, Δp_{bf} , is modelled as a function of the core exit flow quality, water density, mass flow rate, and the pressure

$$\Delta p_b = f_b \Delta p_{cf}(\chi_{co}, \rho_l, \phi_l, p). \quad (5-25)$$

In this function, the two-phase frictional pressure drop is related to the single-phase (water only) pressure drop by a core averaged factor $\langle R_{MN} \rangle$ (Todreas and Kazimi, 1990a)

$$\Delta p_{cf} = c_{cf} \frac{\phi_l^2 \langle R_{MN} \rangle (\chi_{co}, p)}{\rho_l}, \quad (5-26)$$

where c_{cf} is a constant. The value of $\langle R_{MN} \rangle$ is calculated from a fit of averaged factors for a uniformly heated channel as a function of flow quality and pressure as presented by Martinelli and Nelson (Todreas and Kazimi, 1990a). This fit, which is valid for $0 < \chi_{co} < 0.5$ and $1 < p < 100$ bar, is presented in the section **Model parameters** of this chapter. It should be noted that the two-phase flow friction model has a large uncertainty and that the results of Martinelli and Nelson are best applicable to systems with a somewhat smaller mass flow rate (separated flow).

The transit time for the boiling section is derived from

$$\tau_b = \int_{z_l}^{z_t} \frac{dz}{v(z)}, \quad (5-27)$$

where the two-phase flow velocity $v(z)$ follows from the homogeneous equilibrium model

$$v(z) = \frac{\chi(z)\phi_i}{\alpha(z)A_c\rho_g} \quad (5-28)$$

Performing the integration in Eq. (27), while assuming uniform heat production in the boiling section, yields

$$\tau_b = \frac{f_b^l c \rho_g A_c}{\left[1 - \frac{\rho_g}{\rho_l}\right] \phi_i \chi_{co}} \ln \left[\frac{\rho_l \chi_{co}}{\rho_g \alpha_{co}} \right], \quad (5-29)$$

where all variables are taken at time t .

Riser

The water/steam mixture flows through the riser to the upper plenum. This transport is modelled by a transport of flow quality (homogeneous equilibrium flow). The riser outlet quality χ_{ro} is

$$\chi_{ro} = \chi_{co}(t - \tau_r), \quad (5-30)$$

where τ_r is the riser transit time. The average riser quality χ_r is taken

$$\chi_r = \chi_{co} \left(t - \frac{1}{2}\tau_r\right). \quad (5-31)$$

From the average riser quality, the average riser void fraction α_r is calculated

$$\alpha_r = \frac{\chi_r}{(1 - \chi_r) \frac{\rho_g}{\rho_l} + \chi_r}. \quad (5-32)$$

The riser transit time is

$$\tau_r = \frac{l_r \rho_g \alpha_r A_r}{\chi_r \phi_i}, \quad (5-33)$$

where A_r is the cross-sectional flow area of the riser and l_r is the length of the riser.

Upper plenum - carry under

In the upper plenum, free surface water/steam separation takes place. Steam escapes from the water, flows through the steam dome, through the steam dryer, and out of the reactor vessel. The water flow is reversed from upwards to downwards through the

downcomer channel. The steam/water separation is not perfect - some steam is dragged into the downcomer channel by the water. This effect, called carry under, influences the level of subcooling of the water entering the core and the driving force of the circulation flow.

Carry under was studied experimentally and theoretically by Lützow and co-workers for a reactor with a geometry different from that of the Dodewaard reactor (Lützow *et al.*, 1983, 1987b; Lützow and Stäck, 1987a; Lützow and Wegner, 1990). These studies show that the amount of steam dragged into the downcomer channel depends on the quality of the steam in the riser, the water level, the mass flow rate, the pressure (through the properties of water and steam), and the radial distribution of the riser steam quality. As the carry under also depends on the geometry, the results cannot easily be applied to the Dodewaard reactor. For this reason, an empirical approach is followed in the study in this thesis.

Carry under can be described quantitatively in terms of the entrainment ratio Ψ (Wouters *et al.*, 1992b, 1992c)

$$\Psi = \frac{\chi_{di}}{\chi_{ro}}, \quad (5-34)$$

where χ_{di} is the flow quality at the inlet of the downcomer channel. The entrainment ratio is studied as a function of the water level (Wouters *et al.*, 1992b, 1992c) and as a function of the pressure (Van der Hagen *et al.*, 1993a). The measurement results are presented in Figs. 4 and 5. The entrainment ratio is a decreasing function of the water level (Fig. 4). Due to the large scattering of the measurement data the exact relation is not clear. The results can be understood by noting that the radial flow velocity in the upper plenum is lower at higher water level, which increases the steam residence time, and thus increases the steam escape probability (Wouters *et al.*, 1992b, 1992c; Van der Hagen, 1991). As a function of the pressure (Fig. 5), the entrainment ratio increases linearly. Qualitatively, this is due to the smaller density difference between water and steam at higher pressure, which decreases the rise velocity of the steam bubbles, thus decreasing the steam escape probability.

During the experiment of the variation of the water level the pressure was constant, and during the pressure variation experiment the water level was constant. The measurement results for the two experiments were used to estimate the model parameters of the empirical model

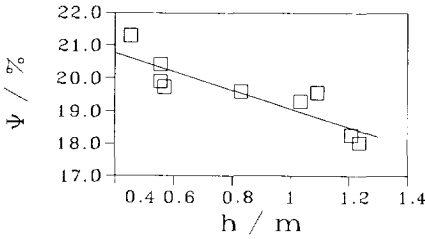


Figure 5-4. Entrainment ratio measured at the water level experiment ($p=69.7$ bar)

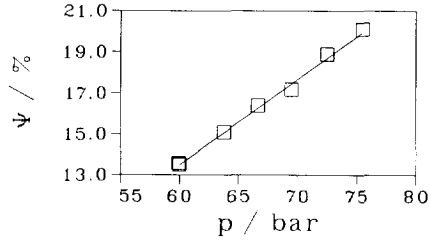


Figure 5-5. Entrainment ratio measured at the pressure variation experiment ($h=0.569$ m)

$$\Psi = c_{cup}P + c_{cuh}h + c_{cu} \tag{5-35}$$

where c_{cup} , c_{cuh} and c_{cu} are constants, and h is the water level. The measurements and the empirical modelling are discussed in further detail in the section **Model parameters** of this chapter.

As the origin of the steam dragged into the downcomer is mostly the outer ring of riser channels (Wouters, 1989), the transit time for the steam from the top of the riser to the inlet of the downcomer channel is small. Furthermore, the temperature of the water in the upper plenum is saturation temperature. For these reasons no transport phenomenon was modelled for this section.

Downcomer channel above the feedwater sparger

As described above, a water/steam mixture flows downwards through the upper part of the downcomer channel. This affects both the driving force of the natural circulation, as well as the level of subcooling. The downcomer inlet flow quality can be calculated from Eqs. (34) and (35)

$$\chi_{di} = [c_{cup}P + c_{cuh}h + c_{cu}] \chi_{ro} \tag{5-36}$$

If carry over, which is the amount of water being dragged into the steam line, is neglected, the water mass flow rate at the downcomer inlet $\phi_{ldi}(t)$ is

$$\phi_{ldi} = [1 - \chi_{ro}] \phi_t \tag{5-37}$$

The steam mass flow rate at the downcomer inlet ϕ_{gdi} is

$$\phi_{gdi} = \frac{\chi_{di} \phi_{ldi}}{1 - \chi_{di}} \tag{5-38}$$

It is assumed that there is no heat exchange between the two-phase flow and the environment on the path from the downcomer inlet to the feedwater sparger. As the two

phases are in thermal equilibrium, no condensation or evaporation takes place.

As the two-phase flow direction is downwards, the velocity difference between the two phases is considerable, which implies that the homogeneous equilibrium model is not applicable. The transport of water and steam from the downcomer inlet to the sparger level (subscripts *lds* and *gds*) is considered separately, with a transport velocity, and a corresponding transit time, for each phase:

$$\phi_{lds}(t) = \phi_{ldi}(t - \tau_{lds}) \quad (5-39)$$

$$\phi_{gds}(t) = \phi_{gdi}(t - \tau_{gds}) \quad (5-40)$$

The average void fraction is calculated by first calculating the average water and steam mass flow rates (subscripts *ld* and *gd*)

$$\phi_{ld} = \frac{\phi_{ldi} + \phi_{lds}}{2} \quad (5-41)$$

$$\phi_{gd} = \frac{\phi_{gdi} + \phi_{gds}}{2} \quad (5-42)$$

and then the average quality

$$\chi_d = \frac{\phi_{gd}}{\phi_{ld} + \phi_{gd}} \quad (5-43)$$

and finally, by applying the void-quality-slip relation (Todreas and Kazimi, 1990a)

$$\alpha_d = \frac{\chi_d}{(1 - \chi_d)S \frac{\rho_g}{\rho_l} + \chi_d} \quad (5-44)$$

where *S* is the slip ratio, defined as

$$S \equiv \frac{v_g}{v_l} \quad (5-45)$$

in which v_g and v_l are the steam and water velocity respectively

$$v_l = \frac{\phi_{ld}}{\rho_l(1 - \alpha_d)A_{dr}} \quad (5-46)$$

where A_{dr} is the cross-sectional flow area of the downcomer channel next to the riser. v_g is calculated from Eq. (45). The slip ratio is taken constant in the model, with a value of 0.43 (Wouters, 1989).

The transit times for the water and steam are

$$\tau_{lds} = \frac{l_{ds}}{v_l} \quad (5-47)$$

$$\tau_{gds} = \frac{l_{ds}}{v_g}, \quad (5-48)$$

where l_{ds} is the distance from the inlet of the downcomer channel to the sparger level.

Condensation and mixing at the sparger level

At the sparger level, the two-phase flow from the top of the downcomer channel and the cold feedwater mix. The steam condenses, and a subcooled single-phase flow continues downwards through the downcomer channel. The condensing process itself, which is estimated to take place over only 0.3 m in the flow direction (Wouters, 1989), is not modelled. The heat balance at the sparger level reads

$$h_{ds} = \frac{\phi_{lds} h_{sat} + \phi_{gds} h_g + \phi_f h_f}{\phi_{lds} + \phi_{gds} + \phi_f}, \quad (5-49)$$

where h_{ds} is the specific enthalpy of the resulting downcomer flow, h_g is the specific enthalpy of steam, and ϕ_f and h_f are the mass flow rate and the specific enthalpy of the feedwater respectively.

Further on in this section, the equation of motion for the circulation mass flow rate ϕ_l is presented. Generally, this flow rate is not equal to the flow rate following from the mass balance at the sparger level

$$\phi_l \neq \phi_{lds} + \phi_{gds} + \phi_f. \quad (5-50)$$

A difference between the right-hand-side and the left-hand-side of this inequality leads to a change in the vessel water level. As the discrepancy is small, no direct flow-path for the change in water level is modelled. The water level is calculated from the water mass content of the vessel. This model is presented further on in this section.

Downcomer channel and lower plenum enthalpy transport

The flow-path through the downcomer channel and the lower plenum from the sparger level to the inlet of the core is split into three sections (see Figs. 1 and 2): from the sparger to the top of the core/bottom of the riser (subscript rc), from the top of the core to the level of the bottom of the core (subscript rc/p), and from the level of the bottom

of the core through the lower plenum to the inlet of the core (subscript lp). For these three sections, the enthalpy transport is modelled by

$$h_{rc}(t) = h_{dc}(t - \tau_{rc}) \quad (5-51)$$

$$h_{\varphi}(t) = h_{rc}(t - \tau_{rc\varphi}) \quad (5-52)$$

$$h_{cr}(t) = h_{\varphi}(t - \tau_{\varphi}) \quad (5-53)$$

where the transit times are

$$\tau_{rc}(t) = \frac{l_{rc} \rho_l(t) A_{dc}}{\phi_l(t - \frac{1}{2} \tau_{rc})} \quad (5-54)$$

$$\tau_{rc\varphi}(t) = \frac{l_{rc\varphi} \rho_l(t) A_{dc}}{\phi_l(t - \frac{1}{2} \tau_{rc\varphi})} \quad (5-55)$$

$$\tau_{\varphi}(t) = \frac{l_{\varphi} \rho_l(t) A_{\varphi}}{\phi_l(t - \frac{1}{2} \tau_{\varphi})} \quad (5-56)$$

where l_{rc} , $l_{rc\varphi}$ and l_{φ} are the (effective) lengths of the three sections, and A_{dc} and A_{φ} are the area of the downcomer channel next to the core and the effective flow area of the lower plenum respectively.

With the result of Eq. (53) to be used in Eq. (14), the modelling following the circulation flow loop is completed. Next, some general models are presented.

Vessel steam and water content

The rate of change of the vessel water mass content m_l is due to three terms: the supply of feedwater, the evaporation of water in the core, and the condensation of carry under near the feedwater sparger (other flows, like the control rod drive flow and the flow through the water purification system are not modelled). The water mass balance reads

$$\frac{dm_l}{dt} = \phi_j - \frac{P_b}{\Delta h_{gl}} + \phi_{gdc} \quad (5-57)$$

where all variables are taken at time t .

Similarly, the rate of change of the vessel steam mass content m_g is due to the production of steam in the core, the condensation of carry under near the feedwater sparger, and the steam flow out of the vessel ϕ_{go} . The steam mass balance reads

$$\frac{dm_g}{dt} = \frac{P_b}{\Delta h_{gt}} - \phi_{gds} - \phi_{go}, \quad (5-58)$$

where again all variables are taken at time t .

Water level

In this study, the water level is defined as the distance between the surface of the water and the top of the riser in the case that no steam is present in the water (the so-called collapsed level). For simplicity, the density at saturation temperature is taken for all the water in the vessel, although in part of the core, in the lower plenum, and in part of the downcomer channel the water is actually subcooled. The water level is calculated from the water mass by

$$h = \frac{m_l - \rho_l V_{h=0}}{\rho_l A_v}, \quad (5-59)$$

where $V_{h=0}$ is the water volume at a water level of zero, and A_v is the area of the horizontal cross-section of the upper plenum.

Pressure

A change in the vessel water mass or the vessel steam mass leads to a change in the pressure. In turn, a change in the pressure affects the densities of water and steam. This mechanism is modelled by considering the volume of the vessel, and of the water and steam content of the vessel. The amount of water and steam calculated with the use of Eqs. (57) and (58) should fit within the vessel volume. A discrepancy between the water/steam volume and the vessel volume results in a change in the pressure. If this process is regarded as an adiabatic process, a change in pressure, in turn, leads to a phase transition of some amount of water or steam, and a change in the water and steam densities.

In order to simplify the problem, only the part of the vessel containing water at saturation temperature and steam is considered. This volume, V_{sat} , is the vessel volume, excluding the downcomer channel below the feedwater sparger, the lower plenum, and the subcooled section of the core, or, in mathematical form

$$V_{sat} = f_b l_c A_c + l_r A_r + V_v - V_{h=0} + l_{ds} A_{dr}, \quad (5-60)$$

where V_v is the net volume of the vessel. The implication of this consideration is discussed further on in this section. The internal energy U_{sat} of the water/steam content

of V_{sat} is

$$U_{sat} = m_{l,sat} u_l + m_g u_g, \quad (5-61)$$

where u_l and u_g is the specific internal energy of water and steam respectively, and

$$m_{l,sat} = m_l - (V_v - V_{sat}) \rho_l. \quad (5-62)$$

If the pressure change due to the above-mentioned volume discrepancy is regarded as a quasi-static process, the internal energy of the system is constant because both the heat and work term, dQ and pdV , are zero in the first law of thermodynamics

$$dQ = dU + pdV \quad (5-63)$$

(Zemansky, 1968). As for the change in pressure the total mass, internal energy and volume is constant, the new pressure p^* satisfies the following set of constraints

$$m_{l,sat}^* + m_g^* = m_{sat}, \quad m_{l,sat}^* u_l^* + m_g^* u_g^* = U_{sat}, \quad \frac{m_{l,sat}^*}{\rho_l^*} + \frac{m_g^*}{\rho_g^*} = V_{sat}, \quad (5-64)$$

where the superscripts * denote the new values and m_{sat} is the total mass in V_{sat} . In this set of three constraints $m_{l,sat}$, m_g , and p^* are three unknowns, as the densities and the specific internal energies depend on p . Eliminating $m_{l,sat}$ and m_g , these three equations are combined to form one constraint for the pressure dependent properties of water and steam at saturation conditions:

$$\frac{u_{sat} - u_l}{u_g - u_l} \frac{\rho_l - \rho_g}{\rho_l \rho_g} + \frac{1}{\rho_l} - \frac{V_{sat}}{m_{sat}} = 0. \quad (5-65)$$

The pressure is calculated by locating the zero of the left hand side of Eq. (65) with the use of pressure dependent water and steam properties. With the new water and steam densities at the new pressure, the new water and steam masses are calculated from

$$m_g^* = \frac{\rho_g^* (V_{sat} \rho_l^* - m_{sat})}{\rho_l^* - \rho_g^*} \quad (5-66)$$

$$m_l^* = m_{sat} - m_g^* + (V_v - V_{sat}) \rho_l. \quad (5-67)$$

In the process of solving the model equations numerically, firstly the steam and water content are updated with the use of Eqs. (57) and (58), and secondly the steam and water content are adjusted according to Eqs. (66) and (67). In reality, as a result of a pressure increase, everywhere in the saturated volume some steam condenses, and with the arising energy the water is brought to saturation temperature. Conversely, at

a pressure decrease, water evaporates and cools down to saturation temperature. A change in pressure thus leads to a change in steam content. The magnitude of this change in steam content, however, is small compared to other processes concerning steam evaporation, condensation and flow. Therefore, the calculated flow qualities in the core, riser and downcomer are not corrected for the change in steam mass content due to a change in pressure. For the pressure change, the mass content of the total vessel is constant due to Eq. (64).

During a change in pressure, the water outside the volume V_{sat} experiences an adiabatic compression or expansion, which leads to a change in the specific enthalpy by an amount of dp/ρ . This change can be neglected compared to the change, due to dp , in the difference between the downcomer water enthalpy and the enthalpy of water at saturation temperature.

Equation of motion of the circulation flow

The driving pressure Δp_d of the circulation flow is calculated from the difference between the effective densities of the contents of the downcomer channel (both above and below the feedwater sparger), and the contents of the core and riser (see Fig. 2)

$$\Delta p_d = g [\rho_l \{ (1 - \alpha_d) l_{ds} + l_{rc} + l_{rcdp} - (1 - \langle \alpha_c \rangle) l_c - (1 - \alpha_r) l_r \} + \rho_g \{ \alpha_d l_{ds} - \langle \alpha_c \rangle l_c - \alpha_r l_r \}], \quad (5-68)$$

where g is the gravitational acceleration. In this expression all variables, except the lengths l , and g , are taken at time t .

The momentum equation for the circulation flow loop reads (Todreas and Kazimi, 1990b)

$$\frac{d\phi_c}{dt} = \frac{\Delta p_d(t) - \Delta p_{nb}(t) - \Delta p_{gy}(t) - \Delta p_{ca}(t)}{\sum_i \frac{l_i}{A_i}}, \quad (5-69)$$

where the summation runs over all sections in the flow loop: the core, the riser, the upper plenum, the downcomer channel, and the lower plenum.

Steam and feedwater flow rate

Both the feedwater mass flow rate and the steam mass flow rate are calculated from the pressure drop for a flow through a pipe with a valve

$$\Delta p_v = \frac{1}{2} K \rho v^2, \quad (5-70)$$

where Δp_v is the pressure drop across the valve, K is the (variable) friction coefficient of the valve, and v is the flow velocity. For the steam flow, the pressure drop is taken equal to the vessel pressure, thus taking the flow resistance of the turbine, the condenser and piping into account also. For the feedwater flow, the pressure drop is the difference between the pressure p_f generated by the feedwater pump and the system pressure. Rearranging Eq. (70) yields

$$\phi_{g0} = \left[\frac{p \rho_g}{C_{g0} K_{g0}} \right]^{\frac{1}{2}} \quad (5-71)$$

$$\phi_f = \left[\frac{(p_f - p) \rho_f}{C_f K_f} \right]^{\frac{1}{2}}, \quad (5-72)$$

where ρ_f is the density of the feedwater flow, C_{g0} and C_f are constants, and K_{g0} and K_f are the friction factors for the steam flow valve and the feedwater flow valve respectively. The valves are both modelled as gate valves. Janssen and Warmoeskerken (1987) give data for the friction factor of a gate valve as a function of the valve opening. The friction factor as a function of the valve opening is approximated by

$$K(A) = C_{gv} e^{-\frac{A}{A_r}}, \quad (5-73)$$

where C_{gv} and A_{gv} are constants. A_{gv} is given such a value that the valve is fully opened for $A=1$. Note that the friction factor is not infinite for a fully closed valve ($A=0$).

Model parameters

In Table 1 the parameters used in the theoretical model are presented. Many parameters are not taken directly from references. Therefore, these values are elucidated below. Properties of water and steam as a function of pressure (and temperature for water below saturation temperature) are calculated with the computer program H2OTP (Cortzen, 1988).

| | |
|-------|--|
| A_c | A_c is the product of the number of fuel assemblies (164; Wouters, 1989) and the cross-sectional flow area of one fuel assembly (which is 0.006981 m ² ; Wouters, 1989). Similarly, A_r |
| A_r | |

- is the product of the effective number of riser channels (41) times the cross-sectional area of one channel (which is 0.0628 m^2 ; Wouters, 1989). As a value for l_r , the length of the non-active part of the core (0.22 m) is added to the actual value of the length of the riser (2.84 m; both data from Wouters, 1989).
- l_r
- $V_{h=0}$ The value for $V_{h=0}$ is based on the following data taken from Verweij (1990). The gross internal volume of the reactor vessel is 68.628 m^3 . The length of the vessel is 12.094 m and the top of the riser is located 7.421 m above the bottom of the vessel. This makes the gross volume of the vessel below the top-of-riser level 42.111 m^3 . The sum of volumes of all vessel internals below the top-of-riser level is 3.940 m^3 . This makes $V_{h=0} = 38.170 \text{ m}^3$.
- A_{ip} As a typical value for A_{ip} , the area of the openings in the shroud of the lower plenum is taken (Verweij, 1990). For l_{ip} twice the vertical distance between the core inlet and the mid-point of the openings is taken, plus, as an estimation of the radial distance travelled, the radial distance between the middle of the downcomer channel and half-way the radius of the core: $l_{ip} = 2 \times 0.875 + 0.7 = 2.45$ (data from Verweij, 1990).
- l_{ip}
- β, λ All β and λ values are taken from the output of CASMO calculations on an E5-type fuel assembly for void fraction 35 % and burn-up 10 MWd/kg (Van der Voet, 1989). The void reactivity coefficients $r_{\alpha 1}$ and $r_{\alpha 2}$ are obtained by fitting the reactivity calculated as a function of the void fraction with the functional form of Eq. (6) (Kleiss, 1982).
- $r_{\alpha 1}, r_{\alpha 2}$
- A_{gv}, C_{gv} A_{gv} and C_{gv} are obtained from a fit of the gate valve friction factor as a function of valve opening, given by Janssen and Warmoeskerken (1987). C_{go} is set at such a value that the steam valve is completely open ($A=1$) at $p=80$ bar and $P=200$ MW.
- C_{go}
- C_f Likewise, for C_f is taken such a value that the feedwater valve is completely open at $p=80$ bar and $P=200$ MW.
- $2\pi R_f \alpha_{fc}$ The value of $2\pi R_f \alpha_{fc}$ is calculated by applying Eqs. (8) and (9) to stationary conditions. In these cases, the average linear power is P/l_c . This yields

Table 5-1. Model parameters

| parameter | value | unit | reference |
|------------------------|------------------------|---------------------------------|---------------------------|
| $2\pi R_y \alpha_{fc}$ | 9.33×10^5 | $\text{W m}^{-1} \text{K}^{-1}$ | see text |
| A_c | 1.145 | m^2 | see text |
| A_{dc} | 2.62 | m^2 | Verweij, 1990 |
| A_{dr} | 3.52 | m^2 | Verweij, 1990 |
| A_{gv} | 0.157 | - | see text |
| A_{lp} | 3.297 | m^2 | see text |
| A_r | 2.575 | m^2 | see text |
| A_v | 6.149 | m^2 | Verweij, 1990 |
| C_{cf} | 2.5 | m^4 | see text |
| C_{cu} | -0.0858 | - | see text |
| C_{cuh} | -0.0283 | m^{-1} | see text |
| C_{cup} | 4.18×10^8 | $\text{m}^2 \text{N}^{-1}$ | see text |
| C_f | 4.16×10^5 | m^2 | see text |
| C^{go} | 2.03×10^5 | m^2 | see text |
| C^{gv} | 117 | - | see text |
| f_p | 1.4 | - | Van de Graaf, 1993 |
| g | 9.81 | m s^{-2} | Weast, 1981 |
| l_c | 1.794 | m | Wouters, 1989 |
| l_{dc} | 0.7 | m | Wouters, 1989 |
| l_{lp} | 2.45 | m | see text |
| l_r | 3.06 | m | see text |
| l_{rc} | 2.136 | m | Wouters, 1989 |
| l_{rcip} | 2.014 | m | Wouters, 1989 |
| p_f | 83.5×10^5 | N m^{-2} | Nissen, 1993 |
| r_D | -2×10^{-5} | K^{-1} | Kleiss and Van Dam, 1985b |
| r_T | -1.75×10^{-4} | K^{-1} | Kleiss and Van Dam, 1985b |
| $r_{\alpha 1}$ | -0.014 | - | see text |
| $r_{\alpha 2}$ | -0.24 | - | see text |
| S | 0.43 | - | Wouters, 1989 |
| $V_{h=0}$ | 38.170 | m^3 | see text |
| V_v | 64.554 | m^3 | Verweij, 1990 |
| β_1 | 0.0002010 | - | see text |
| β_2 | 0.0012521 | - | see text |
| β_3 | 0.0011316 | - | see text |
| β_4 | 0.0024135 | - | see text |
| β_5 | 0.0008807 | - | see text |
| β_6 | 0.0002177 | - | see text |
| β | 0.0060966 | - | see text |
| λ_1 | 0.0128 | s^{-1} | see text |
| λ_2 | 0.0317 | s^{-1} | see text |
| λ_3 | 0.1218 | s^{-1} | see text |
| λ_4 | 0.3220 | s^{-1} | see text |
| λ_5 | 1.3979 | s^{-1} | see text |
| λ_6 | 3.8692 | s^{-1} | see text |
| Λ | 5×10^{-5} | s | Kleiss and Van Dam, 1985b |
| T_f | 2.11 | s | Van der Hagen, 1988c |
| $\rho c_{pl} V_j$ | 3.531×10^6 | J/K | see text |

$$2\pi R_f \alpha_{fc} = \frac{\rho_f c_{pf} V_f}{\tau_f l_c} \quad (5-74)$$

c_{cu} , c_{cup} , c_{cuh}

The parameters for the carry under model c_{cu} , c_{cup} and c_{cuh} follow from a fit, according to Eq. (35), of the entrainment ratio as a function of water level and pressure. The data were calculated from two separate sets of measurements: one at various pressures, and one at various water levels. During the pressure experiment (on 15 September, 1992; Van der Hagen *et al.*, 1993a), the water level was kept at a fixed level. Vice versa, during the water level experiment (on 14 June, 1989; Wouters *et al.*, 1992b, 1992c; Van der Hagen, 1991) the pressure was kept constant. With the use of the heat balance equation at the feedwater sparger level (Eq. (49)), and values of the appropriate flow rates, subcooling, and properties of water and steam, the steam mass flow rate in the downcomer channel is calculated. From the value of the riser exit quality (calculated with Eq. (20) to stay in the framework of the one-dimensional model) and the flow-quality relationship, Eq. (38), the entrainment ratio is calculated. The results are presented in Tables 2 and 3 (T_{fw} is the feedwater temperature). In Figs. 4 and 5 the entrainment ratio is plotted as a function of water level and pressure respectively. Also plotted in these figures are the linear fits. The results of the fits are: $c_{cuh} = -(2.83 \pm 0.58) \times 10^{-2} \text{ m}^{-1}$, $c_{cu} = 0.219 \pm 0.005$ for the water level experiment (with c_{cup} set to zero), and $c_{cup} = (4.18 \pm 0.10) \times 10^{-8} \text{ m}^2/\text{N}$, $c_{cu} = -0.116 \pm 0.007$ for the pressure experiment (with c_{cuh} set to zero). The predictions of the entrainment ratio for $p=69.7 \text{ bar}$ and $h=0.569 \text{ m}$, which is the condition that is covered by both fits, are not equal (water level experiment: $\Psi=0.203$; pressure experiment: $\Psi=0.176$). This is due to other influences than the water level and the pressure, like the radial power distribution, which affects the radial flow quality distribution. By taking $c_{cu} = -0.0858$ the entrainment ratio is fixed at 0.189, which is the average of the before-mentioned Ψ -values.

With this approach to the problem of the carry under it should be noted that it is assumed that the entrainment ratio is linearly dependent on both the water level and the pressure. There is no physical reasoning behind this dependence. As a function of the pressure, the measurement data show the linearity, but as a function of the water level the relation is not clear due to the large scattering of the measurement data. Furthermore, with this approach, it is assumed that the influence of the water level does not depend on the pressure, and vice versa, as only two experiments are considered. Finally, during both experiments, not only the water level or the pressure change, but

Table 5-2. Data on the water level variation experiment

| h m | P MW | ϕ_i kg/s | ϕ_f kg/s | T_{fw} K | $T_{sat}-T_{ci}$ K | ϕ_{gds} kg/s | χ_{di} % | χ_{ro} % | Ψ % |
|----------|-----------|------------------|------------------|---------------|-----------------------|----------------------|------------------|------------------|-------------|
| 0.453 | 160.9 | 1366 | 70.42 | 407.5 | 2.83 | 18.78 | 1.450 | 6.804 | 21.31 |
| 0.555 | 165.3 | 1347 | 72.62 | 409.2 | 3.12 | 18.31 | 1.437 | 7.034 | 20.43 |
| 0.555 | 163.9 | 1421 | 71.89 | 408.4 | 3.05 | 17.62 | 1.306 | 6.564 | 19.90 |
| 0.569 | 163.0 | 1428 | 71.42 | 408.2 | 3.05 | 17.37 | 1.280 | 6.485 | 19.74 |
| 0.830 | 166.3 | 1414 | 73.03 | 408.8 | 3.17 | 17.54 | 1.308 | 6.672 | 19.60 |
| 1.033 | 168.3 | 1448 | 73.95 | 408.8 | 3.20 | 17.42 | 1.268 | 6.570 | 19.30 |
| 1.091 | 168.2 | 1461 | 73.92 | 409.0 | 3.10 | 17.74 | 1.279 | 6.532 | 19.57 |
| 1.207 | 168.6 | 1458 | 74.17 | 409.2 | 3.39 | 16.33 | 1.180 | 6.464 | 18.26 |
| 1.236 | 169.8 | 1466 | 74.67 | 409.3 | 3.44 | 16.20 | 1.164 | 6.459 | 18.03 |

Table 5-3. Data on the pressure variation experiment

| p N/m ² | P MW | ϕ_i kg/s | ϕ_f kg/s | T_{fw} K | $T_{sat}-T_{ci}$ K | ϕ_{gds} kg/s | χ_{di} % | χ_{ro} % | Ψ % |
|-------------------------|-----------|------------------|------------------|---------------|-----------------------|----------------------|------------------|------------------|-------------|
| 59.9 | 166.2 | 1276 | 71.77 | 405.0 | 4.48 | 11.12 | 0.924 | 6.813 | 13.6 |
| 60.0 | 171.8 | 1288 | 74.33 | 404.0 | 4.68 | 11.40 | 0.940 | 6.950 | 13.5 |
| 63.8 | 167.0 | 1285 | 72.75 | 407.9 | 4.25 | 12.75 | 1.051 | 6.965 | 15.1 |
| 66.7 | 166.7 | 1260 | 73.09 | 410.0 | 4.13 | 14.06 | 1.184 | 7.231 | 16.4 |
| 69.5 | 166.6 | 1275 | 73.11 | 410.7 | 4.00 | 14.97 | 1.245 | 7.240 | 17.2 |
| 72.5 | 165.9 | 1234 | 73.01 | 410.8 | 3.90 | 16.68 | 1.434 | 7.607 | 18.9 |
| 75.5 | 164.5 | 1232 | 72.55 | 410.8 | 3.76 | 17.87 | 1.541 | 7.679 | 20.1 |

also some other variables, like, for instance, the circulation flow rate (see Tables 2 and 3). In chapter 6 of this thesis, it is investigated whether the change in other variables is the effect, rather than the cause of the change in entrainment ratio.

R_{MN}, C_{cf}

Usually the local pressure drop due to friction in a two-phase flow is calculated from

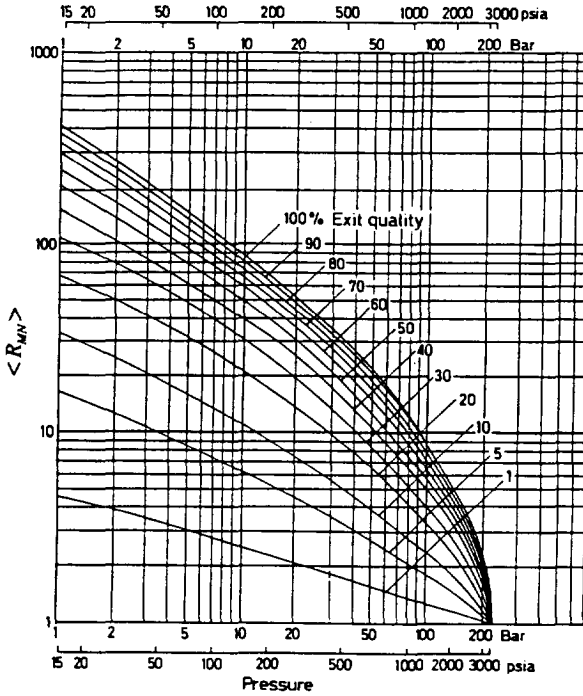


Figure 5-6. Martinelli-Nelson core averaged two-phase flow friction multiplier

$$\frac{dp_f}{dz} = c \frac{\phi_l^2 R_{MN}}{\rho_l} \tag{5-75}$$

where c (m^{-5}) is a constant, and where the so-called liquid-only multiplier R_{MN} is a function of, for instance, local flow quality and pressure. Martinelli and Nelson (Todreas and Kazimi, 1990a) integrated Eq. (75) for a uniformly heated two-phase flow, and calculated averaged two-phase flow friction multipliers for the complete length of the two-phase flow. The result is shown in Fig. 6. The plots shows nearly straight lines for pressures below 80 bar and exit qualities below 10 %, which is the region of interest in this study. An at eye fit of these curves with straight lines was performed. From these lines, the following model for the average liquid-only multiplier was constructed.

$$\overline{\phi_{lo}^2}(X_{co}, p) = e^{-0.1569 \ln(500 X_{co} + 1) \ln(10^{-2} p) + 1.077 \ln(500 X_{co} + 1)} \tag{5-76}$$

The result of the modelling is show in Fig. 7.

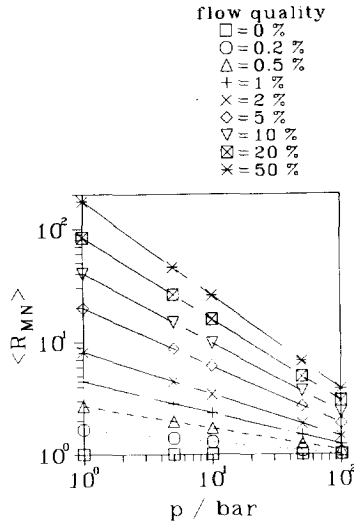


Figure 5-7. Fit of the core averaged two-phase flow friction multiplier as shown in Fig. 6

Both the two-phase flow friction model and the model for the average void fraction in the core and the riser have a large uncertainty. For this reason, the constant c_{cf} in the two-phase flow friction model (Eq. (26)) is not calculated from theoretical considerations, but is put to such a value that the circulation flow is 1300 kg/s at full power conditions ($P=183$ MWth, $p=75.5$ bar, $h=0.55$ m, $T_{fw}=408$ K). c_{cf} is the only model parameter with which the model is tuned to fit the actual behaviour.

Model implementation

Initial conditions

Stationary conditions are chosen as initial conditions. For describing the stationary conditions, the power, the pressure, the water level and the feedwater temperature are chosen as independent variables. In the differential equations given above, all time derivatives are put to zero, and the equations are rearranged, in order to find explicit expressions for many variables. The steam and feedwater flow rate are calculated from the heat and mass balance for the vessel

$$\phi_f = \phi_{g0} = \frac{P}{h_s - h_f} \quad (5-77)$$

For the circulation flow rate, no explicit expression is derived, but an iteration on the circulation flow rate and the subcooling is performed.

The external reactivity ρ_{ext} is put to zero. The reactivity needed for making the reactor critical is calculated, and equated to ρ_0 .

The computer subprogram which calculates the initial conditions can be used for studying the statical behaviour of the Dodewaard reactor (chapter 6).

Solving the differential equations numerically

The set of differential equations can be written in the form

$$\frac{dy}{dt} = f(t,y) . \quad (5-78)$$

A computer subprogram was written to calculate the function $f(t,y)$. Test calculations were performed following Euler's method and the modified Euler method (Burden and Faires, 1985). As the nuclear power is very sensitive to the void fraction, which depends, in turn, on parameters like the subcooling, the circulation flow rate, and the pressure, the nuclear power was taken to inspect the accuracy of the numerical solution. Two cases were considered in which the nuclear power is strongly affected (the physics of both cases is discussed in further detail in chapter 7 of this thesis):

- a step of 20 pcm in external reactivity at full power conditions. In the first few seconds after the reactivity addition, this calculation shows a damped oscillation of the reactor power, with an oscillation frequency of approximately 1 Hz, due to the void-reactivity feedback. After a few seconds other feedback mechanisms, like through the change in the pressure, become important;
- a perturbation of 1 K in the feedwater temperature during one second at very low power and low pressure. The system shows an oscillation with growing amplitude, due to the instability of the circulation flow (see chapter 7).

Test calculations were performed for various time-steps, and with the above-mentioned numerical methods. The calculated power as a function of time was compared for all test calculations. The test calculation show that with a time step size of 0.01 s, and with Euler's method, the power is calculated within a relative uncertainty of ± 0.5 %. Furthermore, the calculations show that with this step size the simulations can be performed real time. In view of the current calculational resources, no further effort was put into minimizing the CPU-time needed to perform an accurate simulation, and Euler's method with a time step of 0.01 s was accepted for solving the set of differential equations.

```

Dodewaard natural circulation BWR simulator

    pressure / bar = 75.53          nuclear power / MW = 184.59
    saturation temperature / K = 564.1      reactivity / pcm = 3
    water level / cm = 55.0          void reactivity / pcm = -3851
    feedwater flow / kg/s = 83.24      Doppler reactivity / pcm = -1348
    feedwater temperature / K = 408.1    temp. reactivity / pcm = -9872
    feedwater flow valve = 0.971      external reactivity / pcm = 20
    steam flow / kg/s = 83.46        start-up reactivity / pcm = 15054
    steam flow valve = 0.991

    subcooling / K = 4.124          average void fraction = 0.305
    circulation flow / kg/s = 1299.8    exit void fraction = 0.617
                                         average quality = 0.040
                                         exit quality = 0.081
                                         boiling length fraction = 0.769

    fuel temperature / K = 674.1      top downcomer void fract. = 0.243
    linear power / MW/m = 102.6       top downcomer quality = 0.017

    driving pressure / Pa = 15308
    core pressure drop / Pa = 15307

                                         time / s = 6.00

set points :
    feedwater valve      steam valve      feedwater temp.      ext. reactivity
    0.971                0.991                408.1                20

```

Figure 5-8. Print-out of the screen of the simulator program

The simulator program

The simulator program provides an accurate simulation of the dynamical behaviour of the Dodewaard natural circulation BWR for a wide range of operating conditions. The simulation is performed real time. The external reactivity, the feedwater temperature, and the settings of the feedwater valve and steam valve can be modified during the simulation. Large amplitude step changes are possible. Each second, the values of the 29 output variables on screen are refreshed (see Fig. 8 for a print-out of the simulator screen), and variables are saved on disk, for later analysis.

Concluding remarks

The model presented in this chapter consists of elements which are simplified and approximate representations of the processes that take place inside the reactor vessel. The strength of the model, however, lies in the interaction of the many subprocesses.

With the experimental results and the simulations presented in chapter 6 and 7, the ability of the model to provide reliable simulations of the statical and dynamical reactor behaviour is checked. Also, the influence of the values of some of the reactor parameters, many of which have a large uncertainty, is studied.

chapter 6

Measurement and simulation of stationary reactor conditions

Introduction

In order to study the stationary conditions of the Dodewaard BWR, extensive measurements have been performed (see the appendix). These measurements comprise basic plant parameters supplied by GKN, like the pressure, neutron flux levels, and the thermal power, thermal hydraulic data measured by KEMA (subcooling, several temperatures and pressure differences in the downcomer channel) and noise measurements performed by IRI, which are used for estimating the circulation flow rate (see chapters 2 and 3), measuring the in-core two-phase flow velocity (see chapter 4), and examining the system dynamics.

The measurements at stationary reactor conditions supply information on the relationship between various reactor parameters, like the circulation flow as a function of reactor power. The reactor behaviour is further analysed with the use of the computer program based on the model presented in chapter 5. With this computer program, the (stationary) initial conditions are calculated as a preparation for the simulation of the time dependent behaviour. The independent variables determining the stationary condition are the pressure, the thermal power, the water level, and the feedwater temperature (see chapter 5, section **Model implementation**). With the computer program, the experiments performed are simulated at the actual operating conditions of the measurements, and similar experiments are simulated at other operating conditions. Also, the influence of reactor parameters on the simulation results are analysed.

The following experiments are considered in this chapter:

- *Variation of power* (experiment: shut-down of the reactor; Van der Hagen *et al.*, 1993b). At a fixed value of the pressure, water level, and feedwater temperature, groups of control rods are inserted gradually. The thermal power decreases as a result of this. With this experiment, the circulation flow rate as a function of power is studied in detail. It should be noted that the insertion of the control rods strongly affects the power distribution, whereas in the model presented in chapter 5 it is assumed that the power distribution does not change. In the following three experiments global perturbations are applied to the reactor and local effects are of secondary importance;
- *Variation of feedwater temperature*. Up to the date of this thesis, no extensive experiment of this kind has been performed. Calculations are performed at a fixed value of the power, the pressure and the water level. Also, a calculation is performed in which a fixed position of the control rods is simulated. In this calculation, an iteration on the power is performed in order to obtain a constant base reactivity ρ_0 ;
- *Variation of water level* (experiment: Wouters *et al.*, 1992b, 1992c; Van der Hagen, 1991). At a fixed value of the pressure and the feedwater temperature, and at fixed positions of the control rods, the water level is varied by controlling the feedwater flow rate. The power is a dependent variable in this experiment. This experiment is simulated by performing an iteration on the power in order to obtain a constant base reactivity ρ_0 ;
- *Variation of pressure* (experiment: Van der Hagen *et al.*, 1993a). At a fixed value of the water level and the feedwater temperature, and at fixed positions of the control rods, the pressure is varied. As with the water level experiment, the power is a dependent variable in this experiment.

In power stations, as a reaction to an increase in the demand of the generator power, the steam flow rate to the turbine is increased by increasing the steam flow valve opening. In the case of direct-cycle BWRs (as the Dodewaard reactor), this leads to a decrease of the pressure. The so-called inherent load following capability of the reactor is the potential to respond passively to the decrease of the pressure with an increase of the nuclear power. In this respect, the experiment of the variation of the pressure is interesting, as with this experiment the inherent load following capability of the reactor is studied. In this chapter, load following is analyzed from the point of view of stationary reactor conditions. In chapter 7, dynamical aspects of load following are studied.

Table 6-1. Measurements during shut-down ($p=75.5$ bar)

| P MW | T_{fw} K | ϕ_t kg/s | $T_{sat}-T_{ci}$ K | $v_{2\phi}$ m/s |
|-----------|---------------|------------------|-----------------------|--------------------|
| 30.0 | 347.7 | 560 | 2.84 | N.A. |
| 65.8 | 366.5 | 972 | 2.74 | 0.983 |
| 86.5 | 391.1 | 1212 | 3.15 | 1.157 |
| 142.8 | 406.7 | 1306 | 3.89 | 1.470 |
| 178.6 | 412.1 | 1300 | 4.47 | 2.400 |

The physics of the stationary reactor behaviour is explained with the use of diagrams showing the main cause and effect relations involved in a particular experiment. In such a diagram, a full-line arrow is drawn between two variables if an increase of the first variable leads to an increase of the second variable. Otherwise, a dashed-line arrow is drawn. Care should be taken when interpreting the diagram, especially when variables are skipped. The signs of all the influences in the path(s) from one variable to another should be taken into account. It is important to note that for clarity, only the main effects are indicated in the diagrams. Effects of minor importance, or potentially large effects caused by a parameter that hardly changes in a particular experiment, are not indicated.

The measurements and the calculations show that carry under has a large effect on the results. In reactors with steam/water separators, like GE's SBWR design (McCandless and Redding, 1989), carry under plays a minor role. Therefore, the physics of a natural circulation cooled BWR without carry under is discussed as well in this chapter.

Variation of power

Measurements and simulations

On 7,8 January, 1993, at the end of cycle 23, measurements were performed at five power levels during shut-down of the reactor. Table 1 presents some of the measured data (Nissen, 1993; Van der Hagen *et al.*, 1993b). The two axially displaced in-core neutron detectors, with which the local in-core two-phase flow velocity $v_{2\phi}$ was measured (see chapter 4), were located approximately half-way the core. The circulation mass flow rate was measured with the techniques discussed in chapters 1, 2 and 3. The

Table 6-2. Simulation of power variation ($p=75.5$ bar)

| P MW | ϕ_t kg/s | $T_{sat}-T_{ci}$ K | f_b % | χ_{co} % | $\langle \alpha_c \rangle$ % | $v_{2\phi}$ m/s |
|-----------|------------------|-----------------------|------------|------------------|---------------------------------|--------------------|
| 1 | 411 | 0.064 | 78.25 | 0.14 | 1.00 | 0.496 |
| 2 | 514 | 0.103 | 78.24 | 0.23 | 1.58 | 0.623 |
| 5 | 679 | 0.196 | 78.20 | 0.43 | 2.92 | 0.833 |
| 10 | 822 | 0.324 | 78.15 | 0.70 | 4.68 | 1.027 |
| 25 | 1023 | 0.657 | 78.03 | 1.41 | 8.72 | 1.332 |
| 50 | 1165 | 1.170 | 77.85 | 2.48 | 13.84 | 1.607 |
| 100 | 1268 | 2.203 | 77.50 | 4.53 | 21.49 | 1.940 |
| 150 | 1297 | 3.311 | 77.15 | 6.61 | 27.25 | 2.178 |
| 175 | 1300 | 3.901 | 76.97 | 7.68 | 29.67 | 2.280 |
| 200 | 1298 | 4.519 | 76.79 | 8.77 | 31.85 | 2.377 |

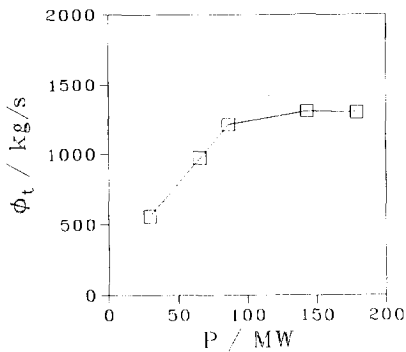
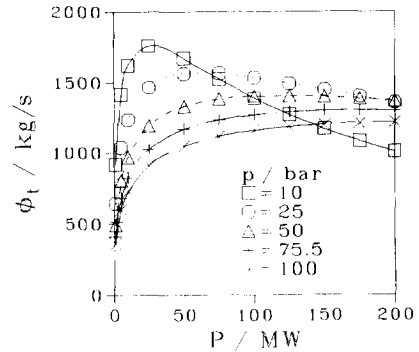
Figure 6-1. Measured circulation flow rate during shut-down ($p=75.5$ bar)

Figure 6-2. Results of calculations of the circulation flow rate as a function of power and pressure

measured circulation flow as a function of the reactor power is plotted in Fig. 1. The table and the plot show that, at low power, the circulation flow increases with power. At higher power, the circulation flow rate saturates.

Simulations show a similar behaviour. Table 2 shows some of the calculated data. The simulations were performed at a pressure of 75.5 bar, a water level of 0.55 m, and

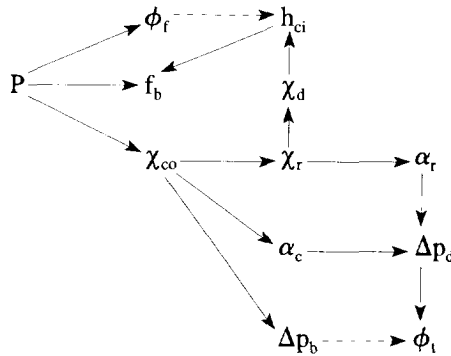


Figure 6-3. Main cause and effect relations involved in the power variation

a feedwater temperature of 408 K. The two-phase flow velocity is calculated at half the height of the core. Figure 2 shows the calculated circulation flow rate as a function of the power, and for various pressures. The effect of the pressure is a shift of the maximum of the circulation flow rate to higher power for higher pressure. At high power, the flow rate at low pressure is lower than the flow rate at high pressure.

Discussion

Figure 3 shows the main cause and effect relations involved in the power variation calculations (see the introduction for some comments on the interpretation of such a diagram). The feedwater flow rate is directly connected with the power through Eq. (5-77). The feedwater flow rate influences the core inlet enthalpy. Through this path, a decrease in the power leads to a decrease of the subcooling ($\equiv T_{sat} - T_{ci}$, in which T_{ci} is the temperature of the water at the core inlet). This decrease in subcooling has an increasing effect on the boiling length fraction. As in the theoretical model the axial power distribution does not change, the increasing effect on the boiling length fraction is exactly compensated for by the decreasing power, which has a direct decreasing effect on the boiling length fraction. The core flow quality is also directly affected by the power. In turn, the core flow quality influences the subcooling through the carry under. The amount of steam dragged into the downcomer channel is a complex function of power and circulation flow. In this application, the net effect of a power increase on the boiling length is a decreasing effect.

In the simulations and the measurements that are discussed further on in this

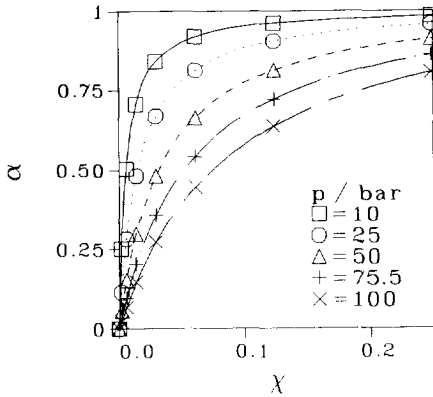


Figure 6-4. Void-quality relationship according to the homogeneous equilibrium model

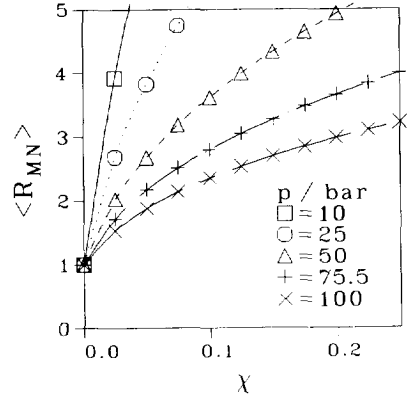


Figure 6-5. Core averaged two-phase flow friction multiplier as a function of flow quality and pressure

chapter, it is shown that the boiling length fraction has a large influence on the results of the experiments. As the boiling length fraction is relatively constant in these calculations, the influence is not discussed here.

The core flow quality influences the circulation flow through different paths. The circulation flow rate is a result of the balance of the driving pressure (Eq. (5-68)), the friction, and the acceleration. For the driving pressure, the riser void fraction is the most important. Of the friction and the acceleration, the in-core two-phase flow friction is the largest. Both the riser void fraction and the two-phase friction depend on the circulation flow rate, the power, and the pressure. In Fig. 4 the void-quality relationship according to the homogeneous equilibrium model (Todreas and Kazimi, 1990a), which is applied in the model for the riser two-phase flow (see Eq. (5-32)), is plotted. The plot shows that, at low quality, the void fraction increases very rapidly as a function of the flow quality. This implies that, at low quality, the driving pressure increases very rapidly with increasing power. The two-phase friction, however, does not show a rapid increase at low quality. This can be seen from Fig. 5, in which the core-averaged two-phase friction multiplier is plotted. As a result of both the void fraction and the two-phase friction multiplier as a function of the power, there is an increase of the net driving force of the circulation flow at low power. But at higher power, where the void-quality relation is less steep, the two-phase friction multiplier still increases with power, resulting in a smaller net driving force.

Due to the smaller density ratio of steam and water at low pressure, the void-quality relation is steeper at low quality. Although the two-phase friction multiplier as a

function of quality is also somewhat steeper at lower pressure, the effect of a lower pressure on the circulation flow rate as a function of power is a shift of the maximum flow rate to a lower power. As the two-phase friction multiplier is larger at lower pressure, while at high quality the void fraction is already near the maximum of one, the circulation flow rate is lower at high power.

At constant flow quality, the two-phase flow friction increases quadratically with increasing flow rate (Eq. (5-26)). At constant power, the two-phase friction multiplier decreases with increasing flow due to the lower flow quality. No general statement about the behaviour of the two-phase flow friction as a function of the flow rate can be made. In this application, however, the two-phase flow friction increases with increasing flow rate at constant power and subcooling. As the void fraction decreases with increasing flow rate, only one value of the flow rate balances the driving pressure and friction. The discussion presented here, however, is a simplified representation of reality. With the computer program for calculating the circulation flow rate, it was checked if multiple solutions for the circulation flow rate exist at a fixed power by applying extreme initial guesses of the circulation flow to the flow iteration process for many operating conditions. No multiple solutions were found. In the model, however, only one flow channel is considered. The search for multiple solutions could be extended to a model in which multiple flow channels are considered.

From a comparison of Figs. 1 and 2 (for $p=75.5$ bar) it follows that the circulation flow rate is overestimated by the simulation at low power. This can be due to the fact that friction in parts of the loop other than the core region is not taken into account in the model. With decreasing power, and thus decreasing in-core friction, the effect of the ex-core friction becomes relatively more important. Furthermore, the model for the two-phase flow friction is very general. A Dodewaard-specific model should be implemented for a more reliable calculation of the circulation flow as a function of the power. Finally, the core flow model is a one-dimensional two-node model. During shut-down, control rods are inserted, which results in a large change in the power distribution, which, in turn, affects the circulation flow rate.

Regarding the subcooling, it is important to note that the feedwater temperature is constant in the simulations, while it varies in the experiment. For this reason, the measured subcooling is higher than the calculated subcooling.

The qualitative behaviour of the in-core two-phase flow velocity is correctly calculated. The magnitudes of the calculated and measured velocity, however, show a large discrepancy, especially at low power. The calculated velocity is very sensitive to

axially distributed parameters, like e.g. the power. An accurate estimation of the two-phase flow velocity cannot be expected from the model presented in chapter 5.

Variation of feedwater temperature

Introduction

Measurements at various feedwater temperatures were performed by Nissen (1988), with the primary objective of studying the response of the feedwater temperature to the shut-down of the feedwater heaters. In this study, the circulation flow rate and the in-core two-phase flow velocity were not measured. The physics involved in the feedwater temperature variation experiment has much lower complexity than the physics of the water level variation experiment or the pressure variation experiment discussed in the next sections. This makes the feedwater temperature variation experiment more suitable for validation of theoretical models. For this reason, extensive measurements at various feedwater temperatures should be performed.

Two kinds of simulations are performed. Both simulations have a fixed pressure and water level, and a feedwater temperature ranging from 373 K to 423 K. In the first simulation the power is fixed. In this simulation the base reactivity is calculated. In the second simulation the base reactivity is fixed at a value which is calculated from a base condition. An iteration on the power is performed in order to obtain a constant base reactivity. In this way, fixed positions of the control rods are simulated.

Simulation at fixed power

The result of a simulation with $P=185$ MWth, $p=75.5$ bar, $h=0.55$ m, and $T_{fw}=373..423$ K is given in Table 3. The base reactivity, the circulation flow rate, the subcooling and the in-core two-phase flow velocity are plotted in Fig. 6. The (simulated) axially displaced in-core neutron detectors for measuring the local two-phase flow velocity were positioned half-way the core. The table and the figure show that, with increasing feedwater temperature the circulation flow and the subcooling decrease, while the base reactivity and the two-phase flow velocity increase. The fact that the circulation flow decreases while the two-phase flow velocity increases is interesting, because this implies that the velocity measured with the downcomer thermocouples (see chapters 2 and 3) decreases, while the velocity measured with the in-core neutron detectors increases.

Figure 7 shows the main cause and effect relations involved in this feedwater temperature variation simulation. An increase in the feedwater temperature has an

Table 6-3. Simulation of feedwater temperature variation at constant power

| T_{fw} K | $\Delta\rho_0$ 10^{-5} | ϕ_t kg/s | $T_{sat}-T_{ci}$ K | f_b % | χ_{co} % | $\langle\alpha_c\rangle$ % | $v_{2\phi}$ m/s |
|---------------|-----------------------------|------------------|-----------------------|------------|------------------|-------------------------------|--------------------|
| 373 | 0 | 1308 | 5.444 | 72.47 | 7.56 | 27.69 | 2.201 |
| 383 | 123 | 1306 | 5.092 | 73.62 | 7.71 | 28.44 | 2.232 |
| 393 | 255 | 1304 | 4.725 | 74.85 | 7.87 | 29.24 | 2.266 |
| 403 | 398 | 1301 | 4.343 | 76.18 | 8.03 | 30.11 | 2.301 |
| 408 | 474 | 1300 | 4.145 | 76.90 | 8.11 | 30.57 | 2.320 |
| 413 | 553 | 1298 | 3.943 | 77.64 | 8.20 | 31.05 | 2.339 |
| 423 | 723 | 1295 | 3.523 | 79.23 | 8.39 | 32.08 | 2.380 |

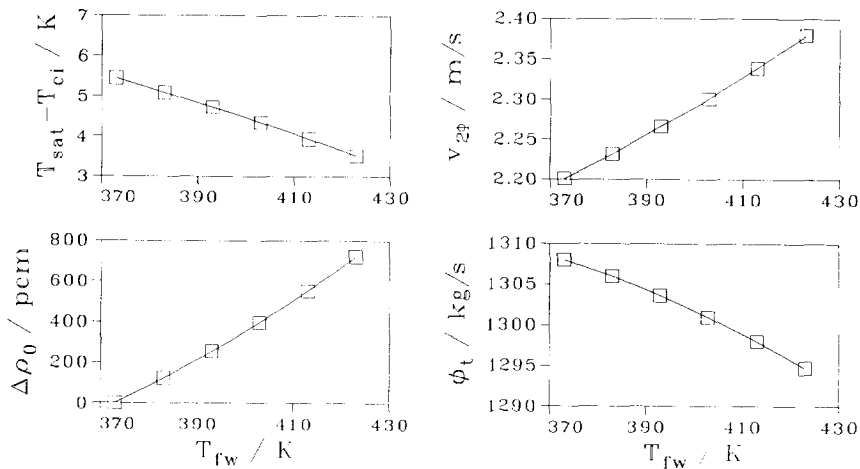


Figure 6-6. Simulation of feedwater temperature variation at constant power

increasing effect on the boiling length fraction through the increase of the core inlet enthalpy. The higher boiling length fraction causes a higher base reactivity through the increase of the negative void reactivity due to the higher core average void fraction.

The driving pressure for the circulation flow increases because the average void fraction in the core and in the riser increases. On the other hand, the increase of the core flow quality and the boiling length fraction causes an increase of the two-phase flow friction in the core. Apparently, the increase of the friction is larger than the

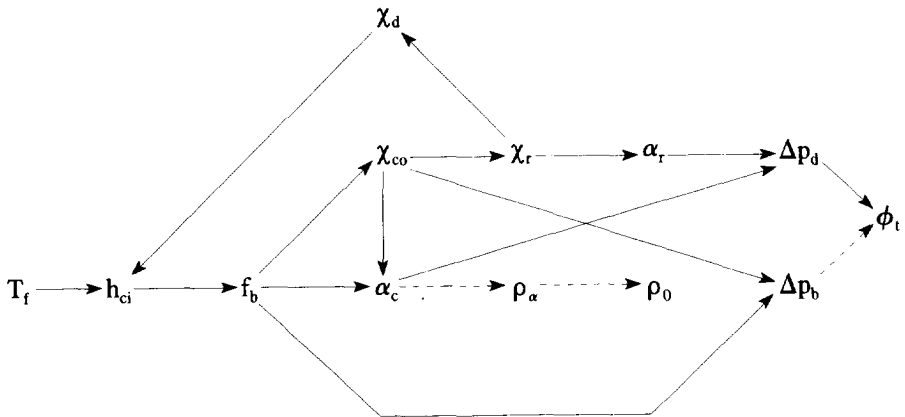


Figure 6-7. Main cause effect relationships involved in the feedwater temperature variation (constant power)

increase of the driving pressure, as the circulation flow decreases. The net result depends on the operating conditions. If the simulation is performed at lower power, the influence of a change in the core flow quality on the driving pressure is higher, as the void-quality relation is steeper at lower quality (Fig. 4). Simulations show that the circulation flow as a function of the feedwater temperature is nearly constant if the power is 100 MWth, and increases if the power is 50 MWth.

The influence of the change in the feedwater temperature on the system parameters is amplified by the positive feedback loop through the carry under. The result of a simulation without carry under is presented further on in this chapter.

The fact that the two-phase flow velocity increases with increasing feedwater temperature, in spite of the fact that the circulation flow decreases, is due to the increase of the boiling length fraction, which increases the flow quality at the height of the detector. The resulting increasing effect on the two-phase flow velocity is larger than the decreasing effect of the circulation flow.

Simulation at fixed base reactivity

In this simulation, with the power as a dependent variable, the feedwater temperature was also varied from 373 K to 423 K. The simulation was started at $P=210$ MWth, $p=75.5$ bar, $h=0.55$ m, and $T_{fw}=373$ K. At this condition, the base reactivity was calculated. At other feedwater temperature levels, an iteration on the power was performed in order to obtain the same base reactivity. In this way, fixed control rod positions were simulated. The (simulated) axially displaced in-core neutron detectors for measuring the local two-phase flow velocity were positioned half-way the core. The

Table 6-4. Simulation of feedwater temperature variation at constant base reactivity

| T_{fw} K | P MW | ϕ_t kg/s | $T_{sat}-T_{ci}$ K | f_b % | χ_{co} % | $\langle \alpha_c \rangle$ % | $v_{2\phi}$ m/s |
|---------------|-----------|------------------|-----------------------|------------|------------------|---------------------------------|--------------------|
| 373 | 210.0 | 1307 | 6.233 | 72.33 | 8.57 | 29.63 | 2.281 |
| 383 | 202.9 | 1305 | 5.624 | 73.51 | 8.45 | 29.88 | 2.293 |
| 393 | 195.8 | 1303 | 5.025 | 74.78 | 8.32 | 30.15 | 2.304 |
| 403 | 188.6 | 1301 | 4.436 | 76.16 | 8.19 | 30.43 | 2.315 |
| 408 | 185.0 | 1300 | 4.145 | 76.89 | 8.12 | 30.57 | 2.320 |
| 413 | 181.4 | 1298 | 3.858 | 77.66 | 8.04 | 30.73 | 2.325 |
| 423 | 174.1 | 1295 | 3.291 | 79.32 | 7.89 | 31.05 | 2.334 |

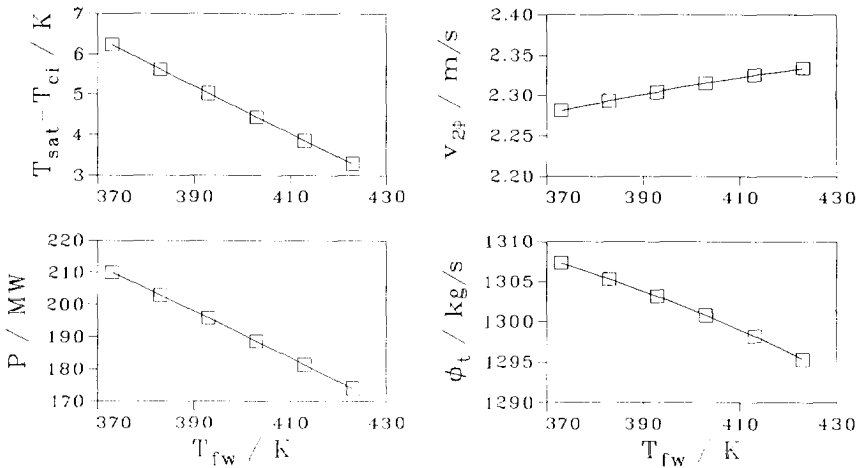


Figure 6-8. Simulation of feedwater temperature variation at constant base reactivity

result of the simulation is shown in Table 4 and Fig. 8. The starting power of 210 MWth was chosen because this leads to conditions close to the full power operating conditions ($P=183$ MWth, $p=75.5$ bar, $h=0.55$ m, $T_{fw}=408$ K). The table and the figure show that, with increasing feedwater temperature, the power, the circulation flow and the subcooling decrease, and the two-phase flow velocity increases.

Figure 9 shows the main cause and effect relations involved in this feedwater temperature variation simulation. The diagram closely resembles the diagram in Fig. 7,

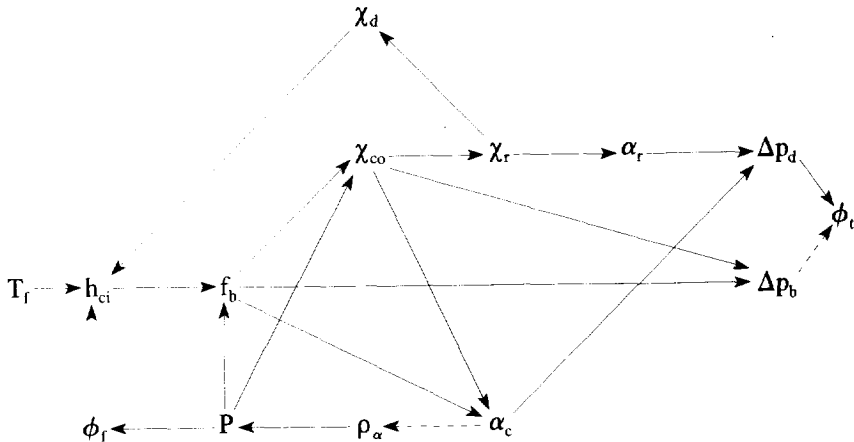


Figure 6-9. Main cause effect relationships involved in the feedwater temperature variation (constant base reactivity)

but now the power, instead of the base reactivity, is affected by the void reactivity. The effect on the power is very large, and this, in turn, has a large influence on the core exit flow quality. In the previous simulation, the core exit quality increased with increasing feedwater temperature. In this simulation it decreases.

The net effect of the power change on the circulation flow is small for the cases considered here, as already discussed in the section **Variation of power**. Because of the large change in power, there is a large change in the feedwater flow rate, which causes a larger change in the subcooling than with the simulation at fixed power.

Because of the increasing boiling length and the decreasing core exit flow quality, the flow quality, and thus the two-phase flow velocity, increases at low level in the core, and decreases at high level. The calculated two-phase flow velocity slightly increases. A simulation with the detector positioned at the top of the core indeed shows that the velocity decreases.

With these calculations, the model possibly suffers from the problem of the relative insensitivity of the circulation flow to a change in power, as already encountered in the section **Variation of power**. The feedwater temperature variation experiment offers the possibility to study the circulation flow rate as a function of the reactor power, for a global perturbation of the reactor, and in an experiment with a relatively low complexity of the physical processes involved.

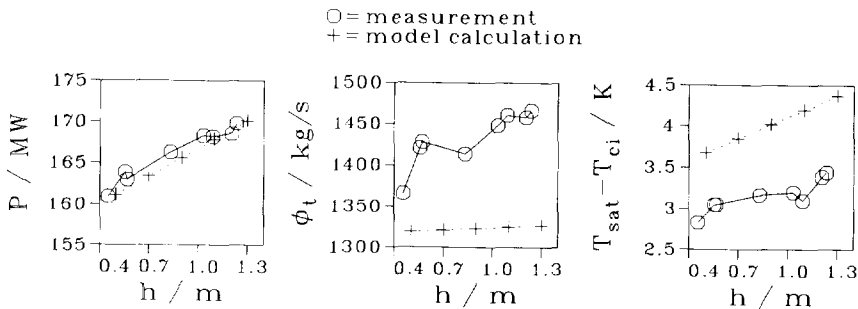


Figure 6-10. Water level variation: measurement and simulation

Variation of water level

Measurements and simulations

On 14 June, 1989, measurements were performed at nine values of the water level (Wouters *et al.*, 1992b, 1992c; Van der Hagen, 1991). During the experiment, the pressure was fixed at 69.7 bar (except for the measurement at 0.555 m and 165.3 MWth, for which the pressure was 69.9 bar), the feedwater temperature was approximately 408 K, and the control rod positions were not altered. In Table 5-2, a summary of the conditions and the measurement data is presented. The values connected with the carry under (the flow qualities and the entrainment ratio) are different from those given by Wouters *et al.* (1992b) because of the different model applied (see chapter 2, **Model parameters**). The measured power, circulation flow rate and the subcooling are plotted in Fig. 10. It can be seen that the power, circulation flow rate and the subcooling increase with increasing water level. For this reason, the water level is used in practice for controlling the power in a small range.

The water level experiment was simulated first by calculating the base reactivity at $p=70$ bar, $P=160$ MWth, $h=0.40$ m and $T_{fw}=408$ K. For other cases (p and T_{fw} fixed; h ranging from 0.5 m to 1.3 m) the power was calculated by performing an iteration on the power in order to obtain the same base reactivity. In this way, the fixed positions of the control rods during the experiment are simulated. Table 5 shows the simulation results, and Fig. 10 shows the calculated power, circulation flow and subcooling. The data on the calculated and measured power agree very well. The amplitude of the change in subcooling is reasonably well predicted. The calculated circulation flow shows qualitatively the same behaviour as the measured circulation flow, but the magnitude of the change is different.

Table 6-5. Simulation of water level variation

| h | P | ϕ_t | $T_{sat}-T_{ci}$ | f_b | χ_{co} | $\langle \alpha_c \rangle$ | Ψ |
|-----|-------|----------|------------------|-------|-------------|----------------------------|--------|
| m | MW | kg/s | K | % | % | % | % |
| 0.4 | 160.0 | 1318 | 3.589 | 76.95 | 6.76 | 29.11 | 19.55 |
| 0.5 | 161.1 | 1319 | 3.674 | 76.69 | 6.78 | 29.06 | 19.27 |
| 0.6 | 162.2 | 1320 | 3.760 | 76.44 | 6.80 | 29.01 | 18.98 |
| 0.7 | 163.4 | 1321 | 3.846 | 76.19 | 6.82 | 28.96 | 18.70 |
| 0.8 | 164.5 | 1322 | 3.933 | 75.95 | 6.84 | 28.92 | 18.42 |
| 0.9 | 165.6 | 1323 | 4.019 | 75.71 | 6.86 | 28.87 | 18.13 |
| 1.0 | 166.7 | 1324 | 4.106 | 75.47 | 6.88 | 28.83 | 17.85 |
| 1.1 | 167.9 | 1325 | 4.193 | 75.24 | 6.89 | 28.78 | 17.57 |
| 1.2 | 169.0 | 1326 | 4.281 | 75.01 | 6.91 | 28.74 | 17.28 |
| 1.3 | 170.1 | 1327 | 4.368 | 74.78 | 6.93 | 28.69 | 17.00 |

Discussion

The main cause and effect relations relevant to the water level experiment are depicted in Fig. 11. An increase in water level influences the system through a decrease in the entrainment ratio. This is due to the lower radial flow velocity in the upper plenum at higher water level, which increases the steam escape probability (Wouters *et al.*, 1992b, 1992c; Van der Hagen, 1991). As a result, the downcomer flow quality decreases. This has a positive effect on the circulation flow through the change in the driving force due to the decrease of the downcomer void fraction. Also, the decrease of the downcomer flow quality increases the subcooling. The effect of this is a decrease of the boiling length fraction.

The lower boiling length fraction decreases the core frictional pressure drop, which, in turn, increases the circulation flow. On the other hand, the decrease in boiling length fraction also leads to a decrease of the driving pressure through a decrease of the void fraction in the core and in the riser. The decrease of the core average void fraction also causes a less negative void reactivity, which increases the power. The power has a positive feedback effect on the boiling length fraction and the core flow quality. Also, a higher power leads to a higher feedwater flow rate. This increase decreases the subcooling even more.

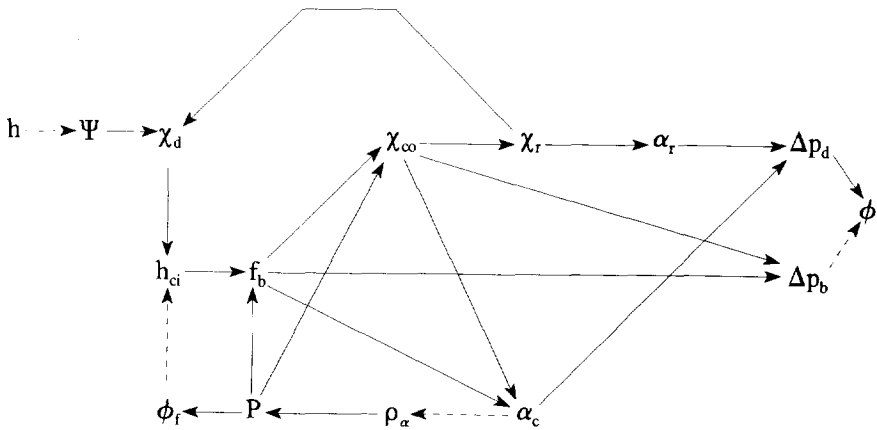


Figure 6-11. Main cause and effect relationships involved in the water level variation

As can be seen from the experimental and calculational results, the net effect of both the decrease of the driving pressure and the reduced frictional pressure drop on the circulation flow rate is positive. The effect is underestimated in the simulations. The increased circulation flow rate has feedback effects on the flow qualities and the pressure drops.

An increase in the water level also decreases the turn-around pressure drop Δp_{up} in the upper plenum for the flow from the riser to the downcomer channel (Lützow and Wegner, 1990; Wouters *et al.*, 1992b, 1992c). This effect, which is not taken into account in the theoretical model presented in chapter 5, has a positive effect on the circulation flow rate. Including this effect in the model will lower the discrepancy between the experimental and the calculational results.

Influence of pressure, power and feedwater temperature

In the water level experiment described above, the lowest water level is 0.453 m, and the power at this level is 160 MWth. The pressure is fixed at 69.7 bar, and the feedwater temperature at approximately 408 K (see Table 5-2). The influence of the pressure, the feedwater temperature, and the power at the lowest water level on the result of the water level experiment was examined by performing simulations of the experiment at 50 bar and 90 bar, with $T_f=398$ K and 418 K, and with initial power 140 MW and 180 MW. These conditions are spread around the condition of the simulation for which the results are listed in Table 5 and are plotted in Fig. 10.

For all simulation cases, the calculated power, subcooling and circulation flow are

Table 6-6. Sensitivity study of the water level variation

| p bar | P MW | T_{fw} K | $\partial(T_{sar}-T_{ci})/\partial h$ K/m | $\partial P/\partial h$ MW/m |
|------------|-----------|---------------|--|---------------------------------|
| 50 | 160 | 408 | 0.814 | 10.63 |
| 70 | 160 | 408 | 0.865 | 11.25 |
| 90 | 160 | 408 | 0.944 | 12.50 |
| 70 | 140 | 408 | 0.758 | 9.75 |
| 70 | 160 | 408 | 0.865 | 11.25 |
| 70 | 180 | 408 | 0.973 | 12.75 |
| 70 | 160 | 398 | 0.866 | 11.00 |
| 70 | 160 | 408 | 0.865 | 11.25 |
| 70 | 160 | 418 | 0.973 | 11.50 |

(approximately) linear functions of the water level (just like in Fig. 10). The change in the circulation flow with respect to the water level is approximately $10 \text{ kg s}^{-1} \text{ m}^{-1}$ for all cases. The results for the power and the subcooling are given in Table 6. The table shows that the rate of change of both the power and the subcooling increases with increasing pressure, power and feedwater temperature. This is caused by the fact that at higher values of these three quantities, the core exit quality is higher. For higher core exit flow quality, a change in the entrainment ratio has a larger influence on the system. The origin of the higher flow quality is the higher power, or the smaller subcooling due to the higher feedwater temperature. The effect of the pressure on the system is analyzed in the next section.

Variation of pressure

Measurements and simulations

On 15 September, 1992 (middle of reactor fuel cycle 23), measurements were performed at six pressure levels, ranging from 59.9 bar to 75.5 bar (Van der Hagen *et al.*, 1993a). The first measurement was performed at 75.5 bar, after the reactor was brought to 164.5 MWth from full power. The pressure was decreased in five steps of approximately 3 bar by controlling the steam flow valve. The positions of the control rods were not altered. The water level varied some 0.12 m only. Table 7 presents the

Table 6-7. Measurement data of the pressure variation experiment

| p N/m ² | T_{fw} K | P MW | ϕ_t kg/s | $T_{sat}-T_{ci}$ K | $v_{2\phi}$ m/s | Ψ % |
|-------------------------|---------------|-----------|------------------|-----------------------|--------------------|-------------|
| 59.9 | 405.0 | 166.2 | 1276 | 4.48 | 3.601 | 13.6 |
| 63.8 | 407.9 | 167.0 | 1285 | 4.25 | 3.522 | 15.1 |
| 66.7 | 410.0 | 166.7 | 1260 | 4.13 | 3.457 | 16.4 |
| 69.5 | 410.7 | 166.6 | 1275 | 4.00 | 3.396 | 17.2 |
| 72.5 | 410.8 | 165.9 | 1234 | 3.90 | 3.329 | 18.9 |
| 75.5 | 410.8 | 164.5 | 1232 | 3.76 | 3.269 | 20.1 |

conditions and the measurement results. Some of the data in this table are also listed in Table 5-3. The two axially displaced neutron detectors, which were used to measure the local in-core two-phase flow velocity were positioned approximately half-way the core. In Fig. 12 the power, the circulation flow, the subcooling and the two-phase flow velocity are plotted. The table and the figure show that the subcooling and the in-core velocity increase with decreasing pressure. The circulation flow rate varies erratically with pressure due to the measurement statistics (the $\pm 2\sigma$ -interval is $\pm 1.3\%$), but on an average, the circulation flow increases with decreasing pressure. The power first increases strongly with decreasing pressure, reaches a maximum value, and decreases at lower pressure.

As with the water level experiments presented above, the pressure variation experiment was simulated by firstly calculating the base reactivity for the condition of the first measurement: $p=75.5$ bar, $P=164.5$ MWth, $h=0.55$ m and $T_{fw}=408$ K. For other cases (h and T_{fw} fixed; p ranging from 72.5 m to 57.5 bar) the power was calculated by performing an iteration on the power in order to obtain the same base reactivity. Table 8 and Fig. 12 show the results of the calculations. The calculated circulation flow rate and the in-core velocity roughly show the same behaviour as in the measurements. The calculated power, however, shows a decrease with decreasing pressure, as opposed to the increase of the measured power (Table 7 and Fig. 12). The slightly non-linear shape of the calculated power as a function of the pressure suggest a maximum at higher pressure. Instead of showing the same linear behaviour as the measured subcooling, the calculated subcooling reaches a maximum value near 61 bar.

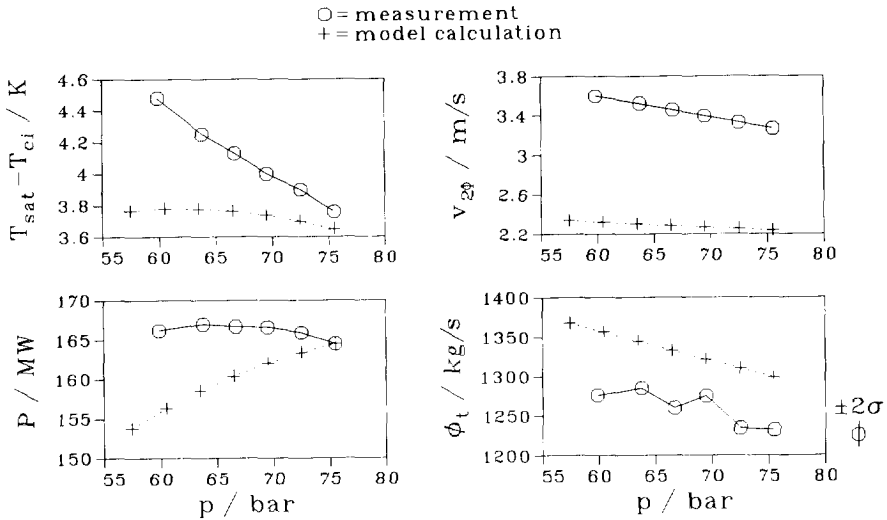


Figure 6-12. Pressure variation: measurement and simulation

Table 6-8. Simulation of pressure variation

| p bar | P MW | ϕ_t kg/s | $T_{sat}-T_{ci}$ K | f_b % | χ_{co} % | $\langle \alpha_r \rangle$ % | $v_{2\phi}$ m/s | Ψ % |
|------------|-----------|------------------|-----------------------|------------|------------------|---------------------------------|--------------------|-------------|
| 57.5 | 153.8 | 1368 | 3.767 | 75.72 | 5.84 | 30.16 | 2.341 | 13.90 |
| 60.5 | 156.3 | 1357 | 3.780 | 75.89 | 6.08 | 29.88 | 2.322 | 15.15 |
| 63.5 | 158.5 | 1345 | 3.778 | 76.08 | 6.31 | 29.62 | 2.304 | 16.41 |
| 66.5 | 160.4 | 1333 | 3.764 | 76.29 | 6.55 | 29.37 | 2.286 | 17.66 |
| 69.5 | 162.0 | 1322 | 3.737 | 76.52 | 6.78 | 29.13 | 2.270 | 18.91 |
| 72.5 | 163.4 | 1310 | 3.699 | 76.77 | 7.01 | 28.91 | 2.254 | 20.17 |
| 75.5 | 164.5 | 1299 | 3.650 | 77.04 | 7.23 | 28.69 | 2.238 | 21.42 |

Discussion

The main cause and effect relations relevant to the pressure variation experiment are depicted in Fig. 13. A change in the pressure influences the system through a change in the properties of water and steam. The main effect of a change in the properties is a change in the two-phase flow in the core, the riser, the upper plenum, and the upper part of the downcomer channel. At lower pressure, the steam density is lower, which

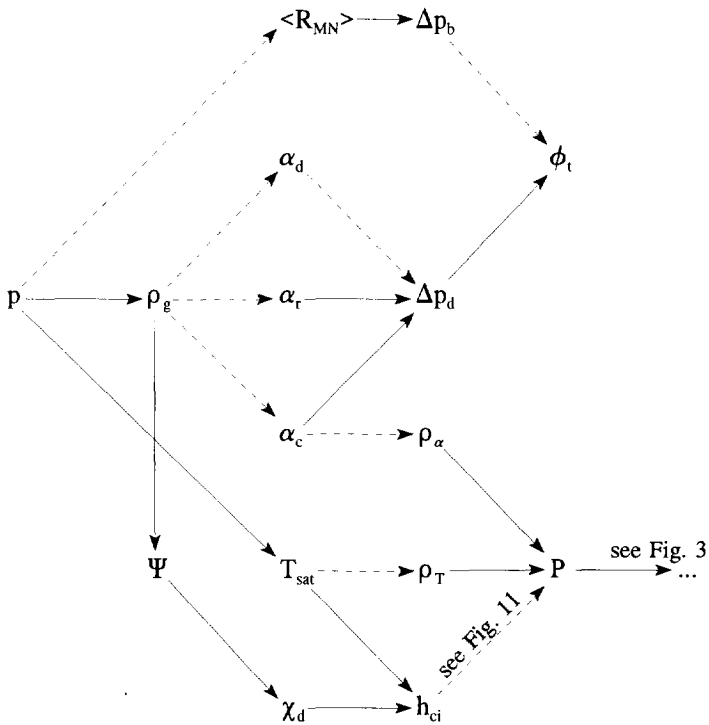


Figure 6-13. Main cause and effect relationships involved in the pressure variation

leads to a higher void fraction. Apparently, although a reduction of the pressure increases the two-phase flow friction, the net result of the pressure reduction is an increase of the circulation flow. The higher core void fraction causes an increase of the negative void reactivity, which, in turn, has a decreasing effect on the power.

The pressure also influences the entrainment ratio through the change in the properties of steam and water. At lower pressure, the density difference between water and steam increases, which increases the bubble rise velocity and thus increases the steam escape probability. In this way, lowering the pressure has the same effect as increasing the water level.

Furthermore, a decrease of the pressure has an increasing effect on the temperature reactivity. For the power and the subcooling, the effect of the pressure through the change in carry under (and, for the power, also through the temperature reactivity) is opposite to the effect through the increase of the void fraction. For the understanding of the behaviour of both the subcooling and the power as a function of the pressure, it is important to know through which path the pressure has the largest influence, and how

the gain depends on the conditions.

- *temperature reactivity*. Through the direct coupling in the model of the temperature reactivity to the saturation temperature, the change in the temperature reactivity with respect to the pressure changes from 16.3 pcm/bar (1 pcm=10⁻⁵) at 75.5 bar to 19.3 pcm/bar at 57.5 bar;
- *carry under*. As the circulation flow decreases with increasing pressure through the path: steam density→void fraction→driving pressure, the core exit flow quality is higher at higher pressure. This implies that the importance of a change in the entrainment is higher at higher pressure. The influence of the carry under on the power also depends on the sensitivity of the void reactivity;
- *void reactivity*. The effect of a change in the void fraction on the void reactivity is larger if the void fraction is larger, because the void reactivity is a quadratic function of the void fraction (Eq. (5-6)). Furthermore, the sensitivity of the void fraction to a change in the steam density depends on the conditions, through the relation according to the homogeneous equilibrium model (Todreas and Kazimi, 1990a)

$$\frac{\partial \alpha}{\partial \rho_g} = \frac{-\alpha^2}{\rho_l} \frac{1-\chi}{\chi} \quad (6-1)$$

From the discussion above, it is clear that setting up general rules for the behaviour is not an easy task. Regarding the subcooling and the power, some conclusions can be drawn from the simulations and the measurements:

- At lower pressure, the change in the circulation flow has a more important effect on the subcooling than the change in the entrainment ratio. This can be seen from the behaviour of the calculated subcooling (Fig. 12). This effect is also present in the measurements, but it is obscured by the decreasing feedwater temperature at lower pressure (see Table 7). Simulating the condition in the calculations at 57.5 bar with $T_{fw}=405$ K instead of $T_{fw}=408$ K results in a subcooling of 3.865 K, which is much higher than the subcooling of 3.767 K calculated with $T_{fw}=408$ K. The effect of the feedwater temperature is discussed in further detail in the section **Variation of feedwater temperature**¹;
- The measured power as a function of the pressure (Fig. 12) shows that the carry

¹For clarity of the results of the calculations, the change in both the feedwater temperature and the water level during the pressure variation experiment was not taken into account in the simulations. A simulation of the experiment with varying feedwater temperature and water level does not show the behaviour of the measured power as shown in Fig. 12.

under and the temperature reactivity effect are larger than the void reactivity effect at higher pressure, and smaller at lower pressure. This behaviour would be even more extreme if the feedwater temperature was 408 K during all measurements, because the higher feedwater temperature lowers the power (see the section **Variation of feedwater temperature**).

The maximum of the calculated power is outside the pressure interval studied with the simulations presented in this section. In the next section, the behaviour at higher pressure is studied, as well as the influence of other parameters.

Qualitatively, the increase of the in-core velocity is correctly calculated. The amplitude of the increase of the velocity and the magnitude of the velocity itself, however, are underestimated. An accurate estimation of the in-core velocity cannot be expected from the simple model presented in chapter 5.

Simulation at higher pressure, and with altered model parameters

A simulation of the pressure variation experiment was performed with initial pressure 100 bar, initial power 160 MWth, water level 0.55 m, and feedwater temperature 408 K. In Fig. 14 the relative power change, $(P-160 \text{ MW}) \times 100/160 \text{ MW}$, is plotted. For the pressure range of the measurements, and the higher pressure range considered in these simulations, the calculated power and the measured power (Fig. 12) roughly show the same behaviour.

The influence of the conditions and the model parameters is examined by simulating the pressure variation experiment with modified parameters. Table 9 shows the result of the calculations. The table shows the maximum relative power change and the pressure at which the maximum is reached. Of the parameters which are modified both the standard value (see also Table 5-1) as well as the modified value are shown in the table.

The results show that the magnitude of the parameters affects the value and the

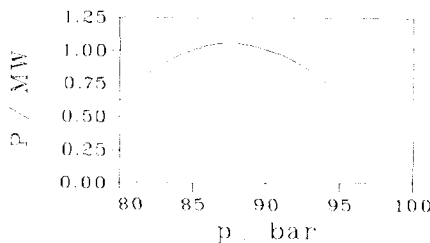


Figure 6-14. Simulation of pressure variation at higher pressure

Table 6-9. Parameter study of pressure variation

| parameter | | max. rel. ΔP | p at max. P |
|--|--|----------------------|-----------------|
| standard value | altered value | % | bar |
| all | - | 1.054 | 87.5 |
| $P=160$ MW | $P=155$ MW | 1.245 | 86.5 |
| $h=0.55$ m | $h=0.25$ m | 1.138 | 87.2 |
| $T_{fw}=408$ K | $T_{fw}=393$ K | 1.165 | 86.8 |
| $c_{cf}=2.5$ m ⁻⁴ | $c_{cf}=2.3$ m ⁻⁴ | 1.229 | 86.8 |
| $c_{cu}=-0.0858$ | $c_{cu}=-0.08$ | 1.110 | 87.3 |
| $c_{cup}=4.18 \times 10^{-8}$ m ² N ⁻¹ | $c_{cup}=4.22 \times 10^{-8}$ m ² N ⁻¹ | 1.233 | 86.7 |
| $f_p=1.4$ | $f_p=1.5$ | 1.090 | 87.2 |
| $r_T=-1.75 \times 10^{-4}$ K ⁻¹ | $r_T=-1.80 \times 10^{-4}$ K ⁻¹ | 1.208 | 86.8 |
| $r_{\alpha 1}=-0.014$ | $r_{\alpha 1}=-0.007$ | 1.211 | 86.7 |
| $r_{\alpha 2}=-0.24$ | $r_{\alpha 2}=-0.23$ | 1.297 | 86.3 |

location of the maximum power. The result is very sensitive to changes in the pressure parameter of the carry under model, the temperature reactivity, and the void reactivity. This can be understood from the fact that the effect of the pressure through the change in carry under and through the temperature reactivity is opposite to the effect through the void reactivity (see above). Furthermore, the power, which influences the void fraction, has a large effect on the result.

The model parameters c_{cup} , $r_{\alpha 2}$ and r_T , which have a large influence on the result of the pressure variation simulation, show a great uncertainty, or depend on parameters like the burn-up or the power distribution. Further research on the magnitude of these parameters is needed. Possibly the model can be tuned, within the uncertainty boundaries of the model parameters, to force the calculations to match the measurements.

The experiment as well as the simulations show that the inherent load following capability (see the introduction to this chapter), as far as stationary reactor behaviour is concerned, is restricted to high pressure. Dynamical aspects of load following are discussed in chapter 7.

System behaviour without carry under

The experimental and calculational results show that carry under is an important effect in the behaviour of the Dodewaard reactor. In a BWR with steam/water separators, like GE's SBWR design (McCandless and Redding, 1989), carry under plays a minor role. In this section, the behaviour of a natural circulation cooled BWR without carry under is discussed.

In the simulations without carry under, the subcooling is higher for all conditions. For this reason, the flow quality, and the void fraction in the core and the riser are lower. Hence, the driving pressure for the circulation flow is lower. Due to the smaller boiling length, the lower flow quality, and the much lower void fraction in the downcomer channel above the feedwater sparger, in most cases, the net effect, however, is a larger circulation flow.

As to the power variation experiment, there is little change in the behaviour. As expected for the boiling length, the change in the feedwater flow rate exactly compensates for the change in the power, which results in a constant boiling length.

For the feedwater temperature experiment with fixed power, the circulation flow rate hardly varies. Due to the absence of the feedback of the core exit flow quality on the core inlet enthalpy through the carry under, the variation in the subcooling, the boiling length, the flow qualities, the void fraction, and the base reactivity are much smaller without carry under. The base reactivity sweep is almost halved. The effect is similar for the feedwater variation calculations with fixed base reactivity. The power sweep for $T_{fw}=373.423$ K is 29.0 MWth instead of 35.9 MWth.

In the simulations without carry under, the water level has no effect on the results. In GE's SBWR design, the water level has a positive effect on the driving pressure, and thus on the circulation flow (Yokobori *et al.*, 1992). This results in a positive effect on the reactivity, and thus on the power.

In the pressure decrease experiment, at high power, the effect of the temperature reactivity alone (without the effect of the changing entrainment ratio) is too small to compensate for the increasing negative void reactivity due to the increasing core average void fraction. As a result, the power decreases monotonously with decreasing pressure. The behaviour of the subcooling and the boiling length without carry under is opposite to the behaviour with carry under. At lower power, at which the core void fraction is lower, the sensitivity of the void reactivity to a change in the void fraction is lower. Near 100 MWth, the power shows a similar behaviour as plotted in Fig. 12. This indicates that the load following capability of a natural circulation cooled BWR with steam/water separators depends on the operating conditions, and on the design (for

example on the void and temperature reactivity coefficients).

Concluding remarks

From the comparison of the model calculations and the measurements, it follows that the theoretical model presented in chapter 5 predicts the reactor parameters for various stationary conditions reasonably well. The simulator program is a very helpful tool for gaining insight into the physics of the stationary reactor behaviour.

Stationary conditions are studied with the use of the measurement data and the simulations. The simulations provide information on reactor parameters which cannot be measured. Furthermore, the influence of the reactor conditions and several model parameters on the reactor behaviour is studied.

The measurements and the simulations show that carry under is an important effect. Both the power and the circulation flow are influenced by the change in the core average void fraction due to a change in the core inlet enthalpy, through a change in the carry under. The core average void fraction is very sensitive to the boiling length. For the power, the calculational results are strongly dependent on the temperature and void reactivity coefficients, and the pressure parameter in the carry under model.

For clarity, the independent variables were varied one at a time in the calculations. In practice, several parameters change at a time. This is one of the reasons that the actual behaviour differs from the calculated behaviour presented in this chapter. As the modelling is limited to the processes inside the reactor vessel (plus the feedwater and steam flow rate), the feedwater temperature is assumed to be an independent variable. The actual feedwater temperature is a result of the characteristics of the feedwater heater system. The load following property can be enhanced by designing this system in such a way that the feedwater temperature decreases passively with decreasing pressure. This is already the case in the Dodewaard reactor as can be seen from the measurements at various pressures (Table 7) and the layout of the feedwater heater system (Nissen, 1988).

In the diagrams shown in Figs. 3, 7, 9, 11 and 13, only the sign of the main cause and effect relations is indicated. Analytical and numerical studies (like Eq. (1) and similar to Table 6) can be performed in order to obtain the gain of the relations. This helps in separating the primary effects from the secondary influences, which, in turn, increases the insight into the behaviour of a natural circulation BWR.

chapter 7

Measurement and simulation of reactor dynamics

Introduction

In chapter 6, the physics of stationary reactor conditions is discussed. In this chapter, the study of the behaviour of the Dodewaard natural circulation cooled BWR is extended to dynamical problems. With the use of measurements, and simulations with the computer program presented in chapter 5, dynamical characteristics of the Dodewaard reactor are examined.

Measurements of the system dynamics were performed by Kleiss and Van der Hagen (Kleiss, 1983; Kleiss and Van der Hagen, 1985a; Van der Hagen 1986, 1989; Van der Hagen *et al.*, 1988b). The experiments comprise control rod step response experiments and steam flow valve step response experiments; both at various operating conditions near full power conditions. Originally, the measurements were performed in order to estimate the reactivity-to-power transfer function and to study the stability of the system.

The reactor can also be perturbed by changing the opening of the feedwater flow valve or varying the feedwater temperature. An extensive experimental analysis of these perturbations has not yet been performed.

The following simulations are considered in this chapter:

- *Short-term response to a reactivity step.* This simulation illustrates the void reactivity feedback and the resulting resonance;
- *Steam flow valve step response.* A change in the setting of the steam flow valve affects the pressure. As all perturbations of the reactor lead to an imbalance in the production and the removal of steam and water, and thus lead to a change in the

pressure, the physics of this experiment is of fundamental importance to all other experiments;

- *Long-term response to a reactivity step;*
- *Feedwater temperature step response;*
- *Feedwater flow valve step response;*
- *Dynamics at low power and low pressure.* Theoretical and experimental studies show that natural circulation systems can exhibit a low-frequency circulation flow resonance at low power and low pressure (Wu *et al.*, 1988; Chiang *et al.*, 1992; Yokobori *et al.*, 1992; Van der Hagen *et al.*, 1993c). This effect is illustrated with the use of measurements and simulations at low power and low pressure.

As shown in chapter 6, carry under is an important effect in the stationary conditions of the Dodewaard reactor. In that chapter, also the behaviour of a natural circulation cooled BWR with steam/water separators, for which carry under plays a minor role, is briefly discussed. In this chapter, it is shown that carry under has a large influence on the long-term stability of the reactor. The dynamics of a reactor without carry under is also discussed in this chapter.

Transient behaviour near full-power conditions

Short-term response to a reactivity step

Generally, a perturbation of the system causes a change in the reactivity of the reactor. For the understanding of the response of the system to the perturbations discussed further on in this chapter, the physics of the short term response of the reactor to a change in the reactivity is of fundamental importance.

As can be seen from Eqs. (5-2) and (5-3), a positive step in the reactivity causes a prompt jump in the power. The increase in the power causes an increase in the fuel temperature, and thus an increase of the heat transferred from the fuel to the water. This, in turn, causes an increase of the boiling length and the flow quality. Both effects result in an increase of the average void fraction, and thus an increase of the negative void reactivity, which provides feedback on the power. The combination of the gains and phases of the various transfer functions in the complete loop determines the dynamics of the system (Lewins, 1978). The response of processes outside the core is too slow to cause an interference on the time scale of a few seconds.

Typically, in a BWR at a high power level, the response of the power to a reactivity impulse is a damped oscillation (Van der Hagen, 1989). By applying a step in the

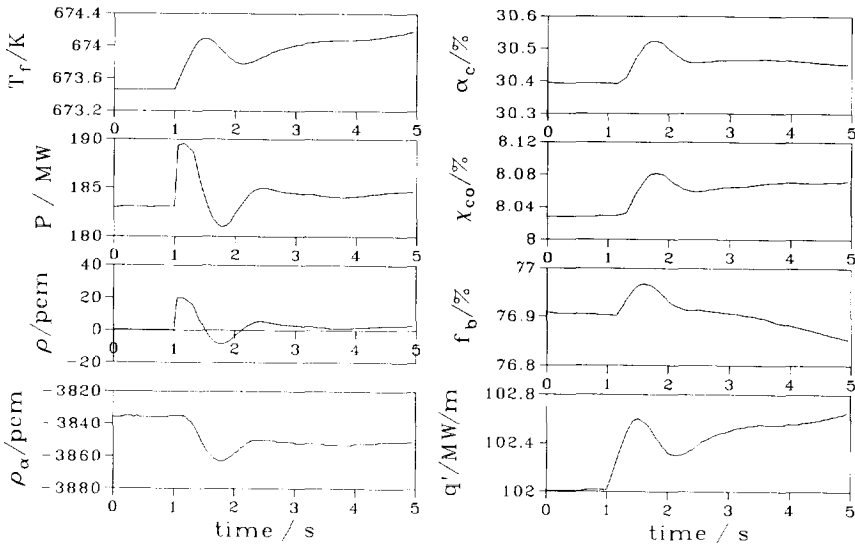


Figure 7-1. Calculated short-term response to a reactivity step of 20 pcm at $t=1$ s

external reactivity of 20 pcm, it is tested if the simulator program shows the same behaviour. Figure 1 shows the result of the simulation (full power conditions). The step in reactivity is applied at $t=1$ s. The power indeed shows a damped oscillation. It can be seen that the system almost balances the reactivity step in a few seconds, and that the power level after the damped oscillation is higher than the initial power, and still increases.

The extra energy released during the first 0.5 s after the step is limited to a few MJ. This causes a minor increase of the fuel temperature. For this reason, the Doppler reactivity is not important in this simulation. The Doppler reactivity is important for much larger steps in the external reactivity, as these result in a larger amplitude of the power, consequently a larger amount of energy released, and thus a larger increase of the fuel temperature.

In practice, fast reactivity increases cannot be realized in the Dodewaard reactor, which implies that the simulated effects cannot be measured directly. The effects can be measured indirectly, for instance, by applying noise analysis techniques. With these techniques, the period of the damped oscillation is found to be approximately 1 s (Van der Hagen, 1989). This value is smaller than the period of the oscillation in the simulation (≈ 1.4 s). As the system dynamics depends on the build-up and transport of steam in the core, the one-dimensional, two-node model is not well suited for providing

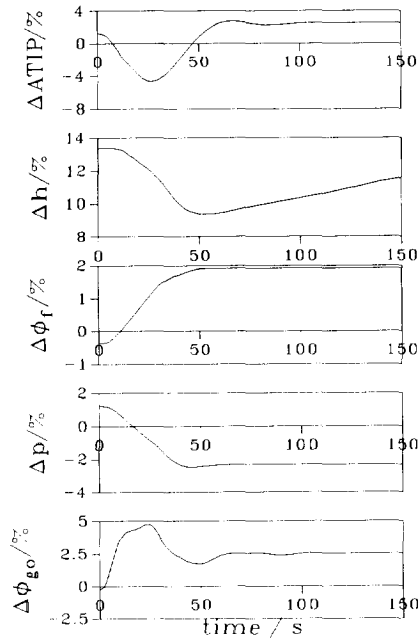


Figure 7-2. Measured response to a steam valve opening

accurate estimations of this phenomenon.

Steam flow valve step response

Measurements of the response of the system to a step in the steam flow valve opening were performed by Kleiss and Van der Hagen (Kleiss, 1983; Kleiss and Van der Hagen, 1985a; Van der Hagen, 1986, 1989; Van der Hagen *et al.*, 1988b). Figure 2 shows the measured response to an opening of a steam valve (Van der Hagen, 1986). It can be seen that the signal of the in-core neutron detector (ATIP), which approximately represents the power, levels off at a higher value, after an initial decrease. The measurements were performed at an initial power of 173.5 MW and an initial pressure of 74.5 bar. The pressure and the water level were not automatically controlled during the measurements.

Figure 3 shows the results of a simulation with initial conditions $p=74.5$ bar, $P=173.5$ MW, $h=0.55$ m, and $T_{fv}=408$ K. The steam flow valve opening was increased from 93.0 % to 93.6 % at $t=1$ s. The step increase of the steam flow valve opening causes a step increase of the vessel exit steam flow rate. Because of the

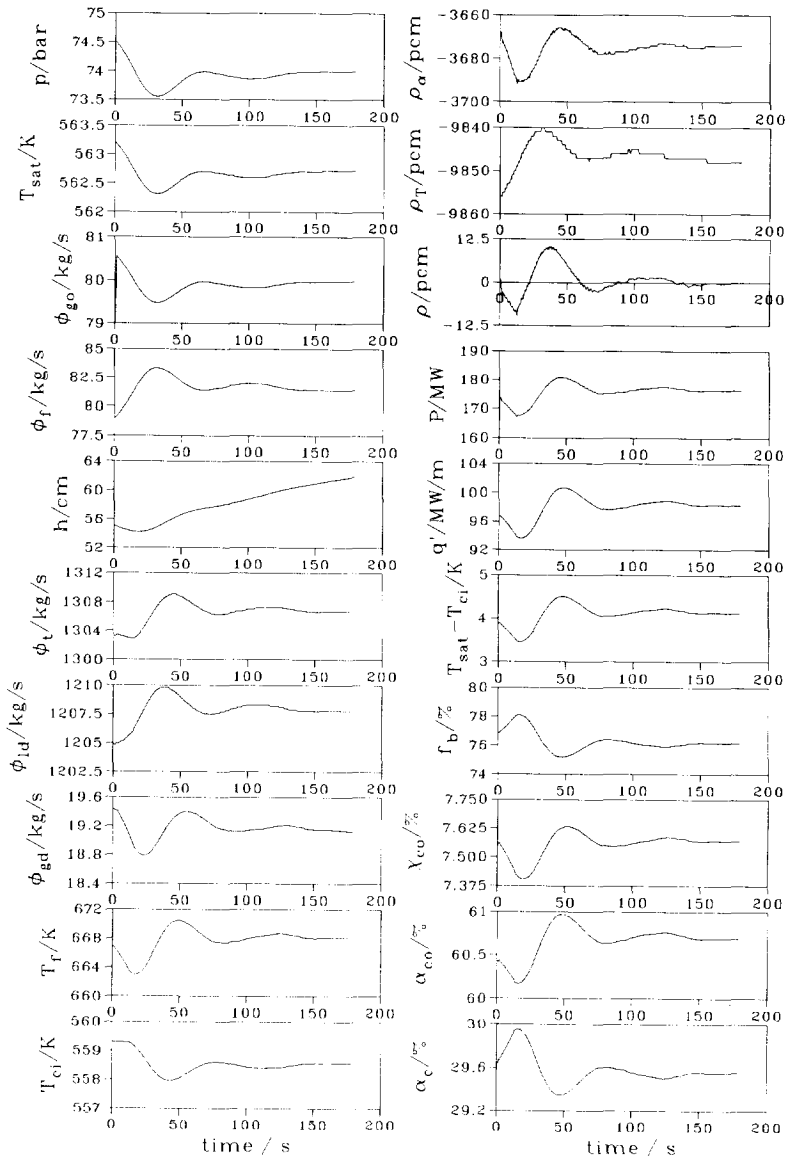


Figure 7-3. Simulation of the response to a step in the steam valve opening of 0.6 % at $t=1$ s

increased steam flow rate, the vessel pressure drops. The lower pressure results in a lower steam density, and thus in a higher in-core void fraction. The higher void fraction, in turn, lowers the power through the negative void reactivity effect.

Because the pressure decreases, also the saturation temperature decreases. As, for the first few seconds, the lower plenum and the lower part of the downcomer channel still contain water from before the step, the core inlet temperature is constant, and the subcooling follows the decrease in the saturation temperature. This leads to an even larger negative reactivity effect. This can be seen from the variation of the subcooling, the boiling length fraction, and the core average void fraction, which all show a close resemblance.

The decreasing saturation temperature increases the temperature reactivity, thus lowering the effect of the other negative reactivity influences. This effect, however, is small.

The lower pressure results in a higher feedwater flow rate, colder water in the upper plenum due to the decrease of the saturation temperature, and a decrease of the entrainment ratio. These three effects result in a decrease of the specific enthalpy of the downcomer flow. The colder downcomer flow takes some time to arrive at the inlet of the core (13 s). Once at the core, it changes the decreasing trend of the power to an increasing trend. The resulting increase of the steam production rate slows down the decrease of the pressure, and eventually, after 30 s, causes the pressure to increase.

This inverts all processes discussed above, which leads to an oscillatory behaviour. The measurements show a strongly damped oscillation, and the simulations show a less well damped oscillation. Simulations at other conditions and with altered model parameters show that the magnitudes of the pressure, the carry under model parameters, and the temperature and void reactivity coefficients have little influence on the damping. Lowering the power and increasing the pressure of the feedwater pump increases the damping. From this, it can be concluded that the variation of the feedwater flow rate has a large influence on the transient.

The damping is also affected by a change in the transit times in the downcomer channel and the lower plenum. A 10 % reduction in the total transit time from the sparger to the inlet of the core leads to a strongly damped oscillation. This can be understood by noting that with a shorter transit time, the direct effect of a pressure change through the negative void reactivity is sooner compensated for by the positive reactivity effect of the change in the feedwater flow rate. In the model, a uniform velocity profile (plug flow) is assumed in the downcomer channel, while in reality a non-uniform velocity profile exists (see chapter 3). For this reason, the transit time for the downcomer channel is overestimated. In view of the complex geometry of the lower plenum, with control rods and TIP-tubes, the transit time for this section in the model shows a great uncertainty.

With the measurements, the opening of the steam flow valve takes some time, and the steam in the steam line shows some inertia. This is another source of difference between the measurement and the simulation.

The simulations only show a small variation of the circulation flow rate. Fast response measurements of the circulation flow rate cannot be performed (see chapter 2). From the small variation in the simulations, it can be concluded that the circulation flow does not have to play an active role in the transient, for obtaining the main measured effects.

Summarizing, the variation of the feedwater flow rate, as a result of the change in the pressure, is important in this transient. The cold feedwater provides the reactivity that is needed to compensate the negative reactivity effect of the increased core void fraction. In this respect, the dynamic load following experiment is different from the static load following behaviour discussed in chapter 6 (see the introduction to chapter 6 for a short explanation of load following). For the stationary conditions discussed in chapter 6, the positive reactivity is provided by the decrease of the carry under and the temperature reactivity effect. The transient in the steam valve opening step reponse discussed here is not finished after 180 s. For instance, the feedwater flow is larger than the steam flow, which leads to an increase of the water level. For this reason, the results concerning load-following presented in chapter 6 cannot be applied to the situation in this transient at $t=180$ s. Eventually, the system levels off at $p=74.2$ bar, $P=176.33$ MW, and $h=0.790$ m after some 30 minutes. Asymptotic behaviour is discussed in further detail in the concluding remarks of this section.

Long-term response to a reactivity step

In the section *Short-term response to a reactivity step*, the response of the system to a step change in the external reactivity up to a few seconds is discussed. After the fast-developing transient that takes place in the core, the system is not stationary (see Fig. 1). Figure 4 shows the long-term reactivity step response with initial conditions $p=74.5$ bar, $P=173.5$ MW, $h=0.55$ m, and $T_{f,w}=408$ K. The step in the reactivity is $+20$ pcm, and is applied at $t=1$ s. For the plot, the output of the simulator program was sampled at 0.5 s intervals. For this reason, the short-term behaviour is obscured. Figure 5 shows the response of the Dodewaard reactor to a control rod step (Van der Hagen, 1986). The pressure and the water level were not automatically controlled during the experiment.

After the short-term transient, the behaviour is similar to the response of the system

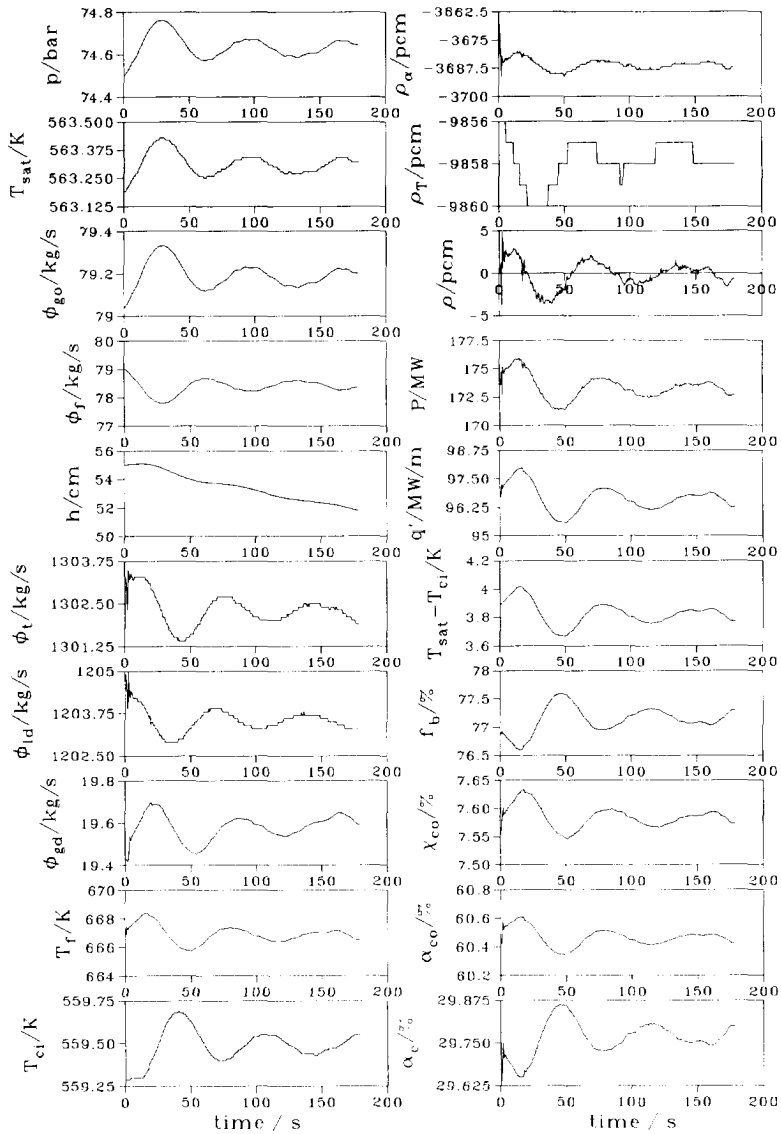


Figure 7-4. Simulation of the long-term response to a step in the reactivity of 20 pcm at $t=1$ s

to a decrease of the steam valve opening. As the power after the short term transient is higher than the initial power, the steam production rate is larger than the steam removal rate. This increases the pressure. Because of the increase in pressure, the feedwater flow rate decreases, which leads to a decreased subcooling after a delay of

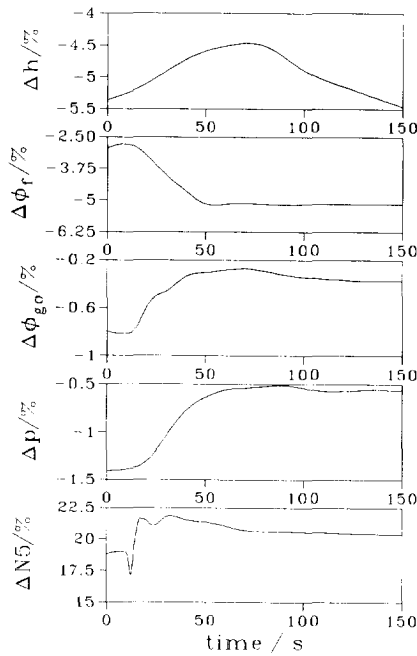


Figure 7-5. Measured long-term response to a control rod step

approximately 13 s (see *Steam flow valve step response*). This, in turn, decreases the reactivity, which results in a decrease of the power. With the decreasing power, the steam production rate decreases, which, at $t=30$ s, leads to a decrease of the pressure. This inverts all the processes.

As with the response to the steam valve opening, the response to the step in the reactivity is a damped oscillation. The general trend in the simulated response resembles the measured response. The oscillations are not clearly visible in the measurements. After 145 s, the pressure is higher than the initial pressure. For this reason, the feedwater flow rate is lower, which has a negative reactivity effect. In the measurements, this effect is smaller than the reactivity effect of the control rod step, because the power after 180 s is larger than the initial power. In the simulations, however, the negative reactivity effect is larger than 20 pcm - the power at $t=180$ s is 173.4 MW. Both the oscillatory behaviour, and the negative influence of the pressure increase, are overestimated in the simulations. As with the steam valve step response, a higher pressure of the feedwater pump increases the damping of the oscillations in the simulations.

Eventually, the system levels off at $p=74.5$ bar, $P=173.5$ MW, and $h=0.477$ m after some 30 minutes; i.e. at the same pressure and power as at the initial condition! When, through automatic or manual control of the feedwater and steam flow valves, the water level and the pressure are brought back to their initial values, a positive reactivity effect of 20 pcm results, which leads to a power of 174.41 MW. Asymptotic behaviour is discussed in further detail in the concluding remarks at the end of this section.

The step in the control rod position causes a large perturbation of the three-dimensional power distribution. In spite of the fact that the power distribution is assumed to be constant in the model, the general trend in the simulations resembles the measured response. In the following transients (and in the steam flow valve step response), global perturbations are applied to the reactor.

Feedwater transients

In the past, some feedwater temperature step responses were performed for estimation of the circulation flow rate (Oosterkamp, 1983). Also, during tests of the feedwater heater, measurements of several thermocouple signals and ex-vessel neutron flux levels were performed (Nissen, 1988). At the date of this thesis, no detailed measurements of feedwater temperature step responses have been performed yet.

In Fig. 6 the response of the system to a perturbation of -2 K in the feedwater temperature, at $t=1$ s, is plotted. The initial condition is $p=74.5$ bar, $P=173.5$ MW, $h=0.55$ m, $T_{fw}=408$ K. The plots show that 13 s after the change in the feedwater temperature, the colder water reaches the inlet of the core. The subcooling increases drastically, leading to a sudden decrease of the boiling length. This has a direct effect on the negative void reactivity, and thus on the power. The reactivity effect is much larger than indicated in the figure - the sampling of the output of the simulator program obscures the fast transients. Simulations with a high time resolution indicate a maximum void reactivity change of 46 pcm. From this point, the transient resembles the response to a step in the reactivity. The simulation result is somewhat different, especially regarding the oscillations. The variation of the circulation flow is larger. Long-term simulation of the response shows that the system levels off at $p=74.5$ bar, $P=174.4$ MW, $h=0.51$ m, with $T_{fw}=406$ K.

The response of the system to an increase of the feedwater valve opening resembles the response to an decrease of the feedwater temperature, as both transients have the strong effect of a lower core inlet temperature. With the feedwater flow rate transient, however, the water level increases at the beginning of the transient. Figure 7 shows the

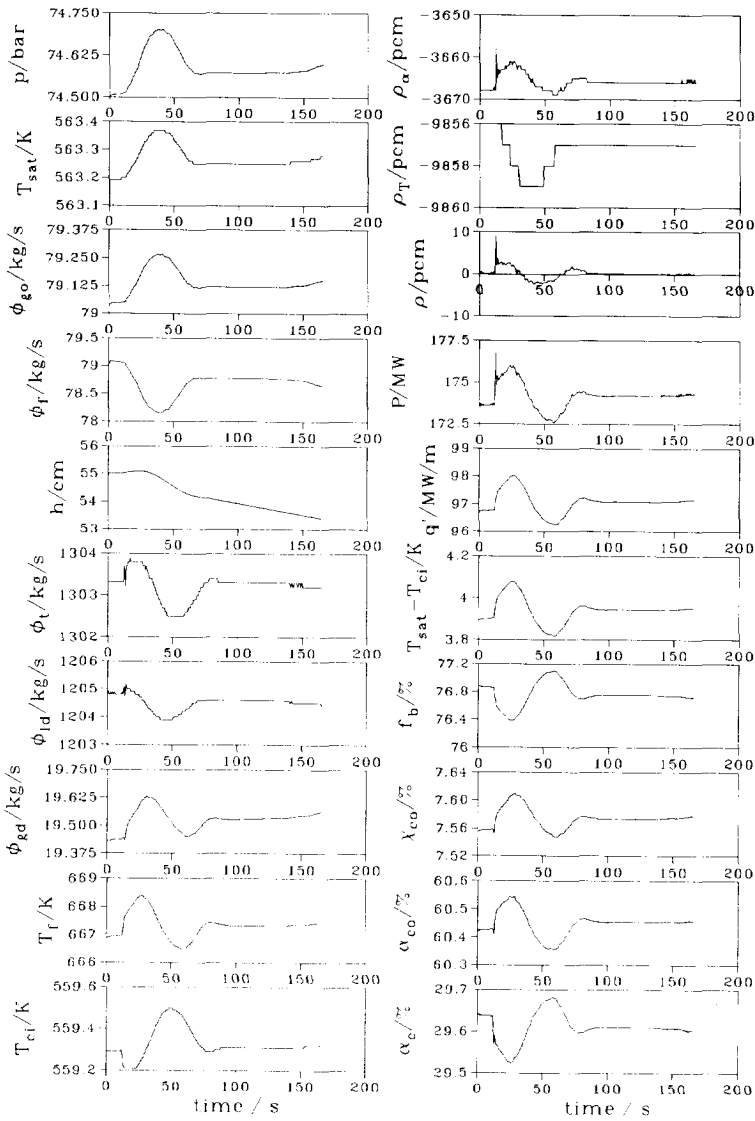


Figure 7-6. Simulation of the response to a step in the feedwater temperature of -2 K at $t=1$ s

response of the system to a increase of 0.2 % of the feedwater flow valve at $t=1$ s. Again, the initial condition is $p=74.5$ bar, $P=173.5$ MW, $h=0.55$ m, $T_{fw}=408$ K. After 140 s, the increase of the water level continues, leading to a long-term increase of the power and the pressure. Eventually, the system levels off at $p=74.6$ bar, $P=173.85$ MW, and $h=0.577$ m.

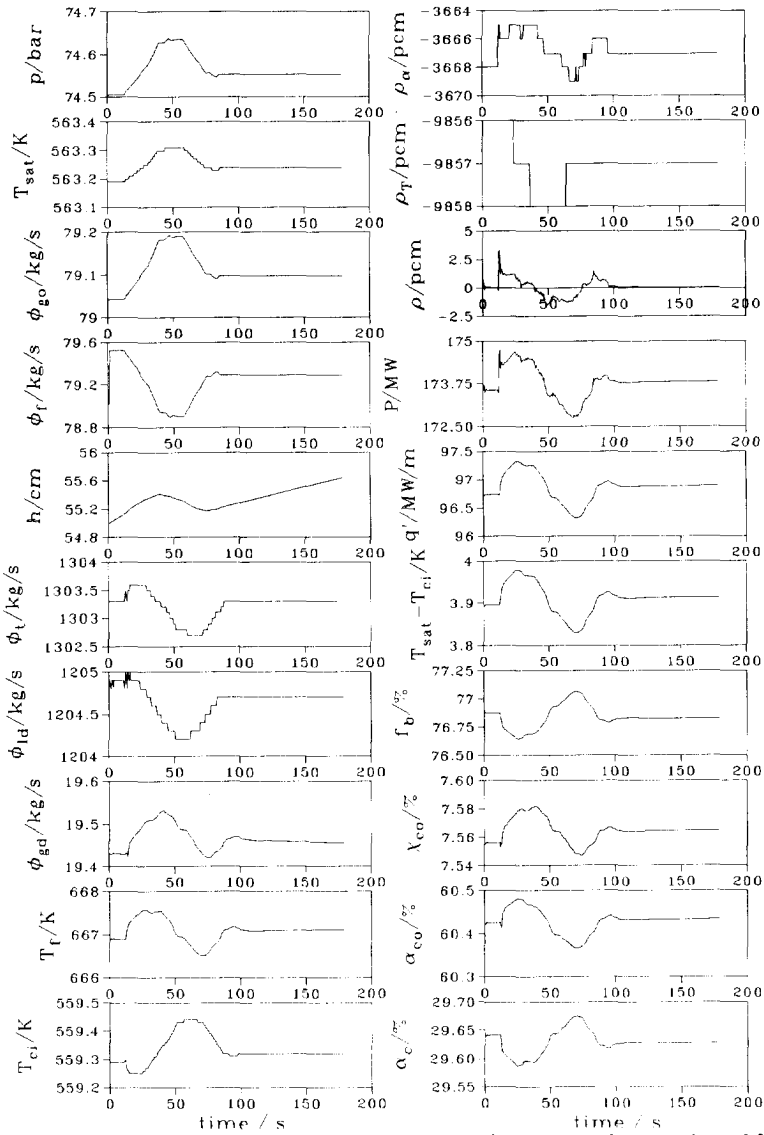


Figure 7-7. Simulation of the response to a step in the feedwater valve opening of 0.2 % at $t=1$ s

Concluding remarks

In the discussions of the transients presented above, the following effects, with a characteristic time period of operation, are important:

- The void reactivity feedback (within seconds);
- The temperature reactivity through the pressure (several seconds);
- The void reactivity through the effect of the pressure on the properties of steam and water (several seconds);
- The void reactivity through the effect of the pressure on the feedwater flow (several seconds and delayed);
- The void reactivity through the effect of the pressure on the carry under (several seconds and delayed);
- The void reactivity through the effect of the water level on the carry under (several minutes).

A fast effect, which is of minor importance to the transients discussed above, is the Doppler reactivity effect.

In chapter 6, stationary conditions were investigated with the pressure, the power, the water level and the feedwater temperature as independent variables. In a transient, the pressure, the power and the water level are dependent variables. For possible stationary conditions, (asymptotically) following a transient, the resulting pressure can be calculated by equating Eq. (5-71) and (5-72). As ϕ_{go} increases, and ϕ_f decreases with increasing pressure, only one solution for the pressure exists. The resulting power can be calculated by inverting Eq. (5-77). The remaining dependent variable, which is the water level, has such a value that the net reactivity is zero. This implies that for all transients, for which all variables stay within reasonable bounds, an asymptotically stationary condition exists. If, and how the system reaches the stationary condition is determined by the above-mentioned dynamical effects.

If the pressure is higher than the pressure of the stationary condition, the power becomes lower, thus reducing the steam production and thus the pressure. Similarly, if the pressure is too low, the power is higher, and thus the pressure will increase. On a longer time scale, the water level dynamics is important. If the water level is too high, the lower entrainment ratio causes a power which is too high. The steam production and the pressure are too high, and the steam flow is larger than the feedwater flow, which reduces the water level. Similarly, a water level which is too low causes the situation $\phi_f > \phi_{go}$, and thus a water level increase.

With respect to the dynamics, it is important to note that the time scale of the water level dynamics is larger than the time scale of the pressure dynamics. Also, the changes in the system conditions are smaller with the long-term water level dynamics than with the pressure dynamics. In this way, the system delicately uses the pressure dynamics

to bring the water level to the final value.

The discussion of the long-term behaviour presented here is not a solid proof of the stability of the system, but makes the stability of the system plausible.

System dynamics without carry under

In the simulations discussed above, the pressure affects the core inlet enthalpy through the change in both the feedwater flow rate as well as the carry under in the same way. For this reason, the influence of the pressure on the development of the transient is smaller for a system without carry under than for a system with carry under. Simulations show that this increases the damping of the oscillations in the steam valve setting step response and the reactivity step response. For the feedwater transients, the shape of the oscillations changes.

In the simulations without carry under, the water level provides no feedback on the system. This implies that there is no long-term stabilizing effect, as sketched above. Therefore, a few minutes after a transient, a system without carry under shows (nearly) constant pressure, power, flow rates, etc., but a linearly varying water level.

With GE's SBWR design (McCandless and Redding, 1989), a natural circulation cooled BWR with steam/water separators, the water level has a positive effect on the circulation flow rate, and thus on the reactivity (Yokobori *et al.*, 1992). This might provide the necessary feedback for ensuring passive long-term stability.

Dynamics at low power and low pressure

Introduction

Due to the low steam density at low pressure, the void fraction as a function of the flow quality shows a large gradient at low quality (see Fig. 6-4). This implies that, at low pressure and low quality, a fluctuation in the circulation flow rate, which causes a fluctuation of the flow quality, results in a large fluctuation of the void fraction. As the void fraction provides the driving force of the circulation flow, the large negative gain of the feedback loop from and to the circulation flow, via the void fraction, can cause stability problems. In literature, both experimental and theoretical studies of this effect are presented (Wu *et al.*, 1988; Chiang *et al.*, 1992; Yokobori *et al.*, 1992). In short, in most cases, the stability of the phenomenon described above is improved by increasing the power, by increasing the pressure, and, at low subcooling, by decreasing the subcooling even more. This can be understood by noting that all these changes decrease the gradient of the void-quality relationship. For further detail, the reader is

Table 7-1. Measurements during start-up

| p bar | P MW | $T_{sat}-T_{ci}$ K | ϕ_i kg/s |
|------------|-----------|-----------------------|------------------|
| 2.9 | 0.9 | 7.3 | 466 |
| 4.2 | 0.9 | 7.5 | 616 |
| 5.6 | 1.4 | 7.2 | 746 |

referred to literature.

Measurements

As the stability of the circulation flow is highest at high power and high pressure, the start-up phase of a natural circulation cooled BWR is important. During start-up, the reactor is brought from a low power and low pressure condition to a high power and high pressure condition.

In order to investigate the circulation flow dynamics at the Dodewaard reactor, measurements were performed in the beginning of the start-up phase (Van der Hagen *et al.*, 1993c). Table 1 presents some of the measurement results. The power is calculated from the relative readings of the ex-vessel neutron detectors. As the calibration curve for the circulation flow measurements, presented in chapter 3, is applied for pressures which are much lower than the pressure for which the calibration was performed, the measurements only give a rough indication of the magnitude of the circulation flow rate.

The table shows that the circulation flow rate is high for very low power: 35 % of the circulation flow rate at full power conditions at a relative power of 0.5 %. The response time of the circulation flow measurement technique is too large to measure the fluctuations (or possible oscillations) of the circulation flow. Flow fluctuations, however, affect the power through the fluctuations of the negative void reactivity caused by the resulting core void fraction fluctuations. In this way, flow fluctuations can be detected by analyzing the signals of neutron detectors.

Figure 8 shows the noise signal of the ex-vessel neutron detector N5 for $p=2.9$ bar, 4.2 bar and 5.6 bar. The noise signal for the lowest pressure shows a resonance with a period of 7-8 s. For $p=4.2$ bar, the signal still shows much low-frequency noise, but the noise level is lower. For the highest pressure, the noise is more white and the noise level is even lower. This behaviour can also be seen in the frequency domain. Figure 9

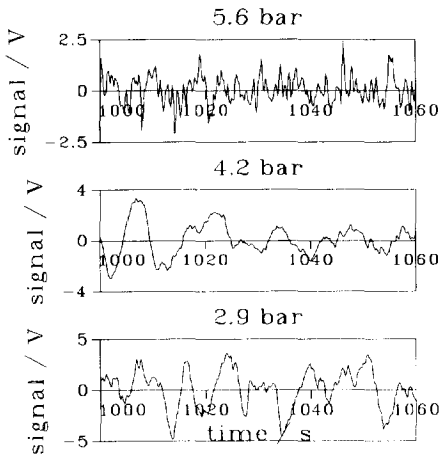


Figure 7-8. Noise signal of the ex-vessel neutron detector N5 during start-up

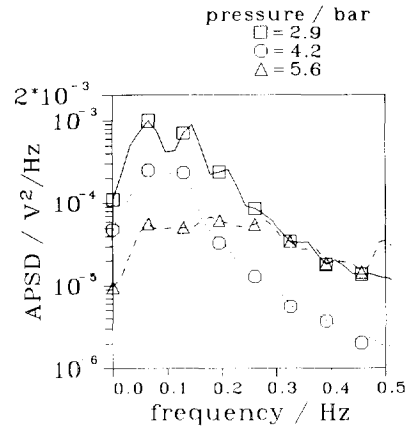


Figure 7-9. Auto-power spectral density of the noise signal of the ex-vessel neutron detector N5 during start-up

shows the normalized auto-power spectral density of N5 for the same pressures. Clearly, the low-frequency content of the spectrum decreases at higher pressure.

The noise signal of the neutron detector is not only affected by the circulation flow fluctuations, but also by fluctuations of the feedwater flow and the pressure. By cross-correlating the noise signals of several sensors, it was found that the fluctuations of the neutron detector noise signal are caused by fluctuations of the circulation flow rate.

Simulations

At $p=2.9$ bar during the start-up measurements, the reactor cooling and heating system for the shut-down period (RAS; *Reactor Afkoel Systeem*) is still in operation. With the RAS, water is extracted from the vessel above the feedwater sparger, cooled or heated, and injected with the feedwater flow in the vessel through the feedwater sparger. Furthermore, the reactor is not stationary, as the water level decreases during the measurement. Finally, many of the model parameters presented in chapter 5 are only valid for reactor conditions near full power conditions. In a preliminary study, however, the circulation flow dynamics was simulated at low power and low pressure with unaltered model parameters. A model for the RAS was included in the simulator.

Figure 10 shows the result of a simulation with initial condition $p=3$ bar, $P=1$ MW, $h=0.55$ m, $T_{fw}=353$ K and RAS-flow 2.5 kg/s. During the simulation, no perturbations were applied - the system is excited by numerical inaccuracies in the initial conditions and in the integration of the differential equations. The result shows

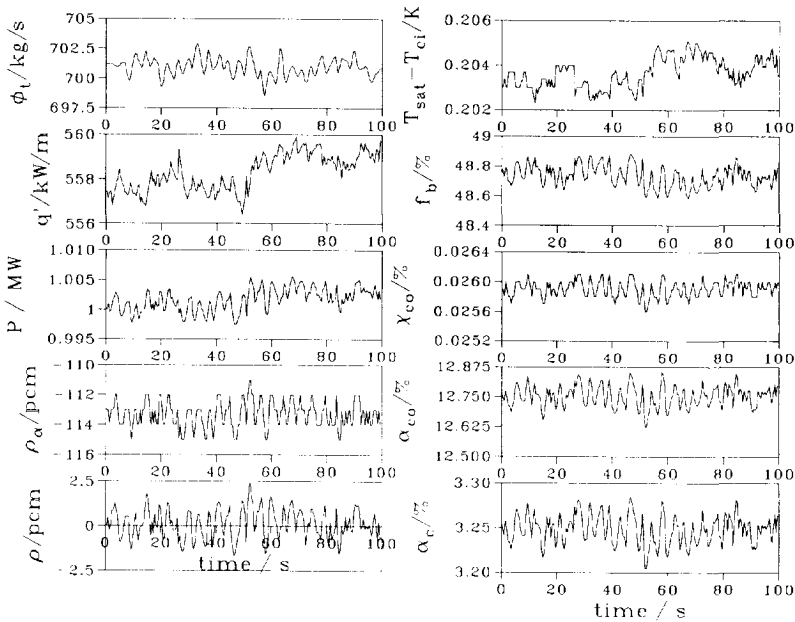


Figure 7-10. Simulation of the circulation flow dynamics at low power and low pressure. Simulation with feedback on the power.

a resonance with a period of approximately 4 s.

As discussed in the introduction to this section, the circulation flow resonance is a purely thermal hydraulic effect. In order to examine the function of the power in the simulation results in Fig. 10, the simulator program was altered in such a way that the power remained constant. Figure 11 shows the result of the same simulation as in Fig. 10, but with constant power. The plots show a growing oscillation with a period of approximately 11 s.

Other simulations show that the result is strongly dependent on the pressure and on the variables which determine the flow quality in the core, i.e. the power, the feedwater temperature and the RAS-flow rate. Also, different types of dynamical behaviour are encountered: noise, noise with a distinct resonance, (nearly) harmonic oscillations, etc.

The results show that the simulation program based on the model presented in chapter 5 in principle offers the possibility of simulating the dynamical effects at low power and pressure. For a thorough study of these complex phenomena, however, both the model, and the model parameters will have to be adapted to the reactor start-up conditions.

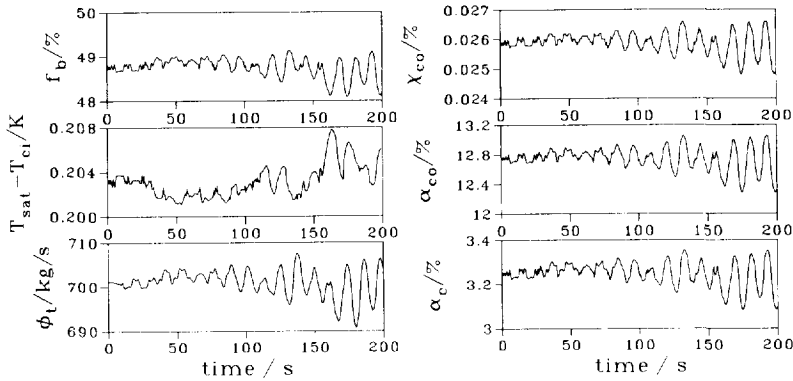


Figure 7-11. Simulation of the circulation flow dynamics at low power and low pressure. Simulation at fixed power.

Concluding remarks

From the comparison of the simulations and the step response measurements, it follows that the model presented in chapter 5 predicts the general trend in the measurements reasonably well. The damping in the simulated responses, however, is lower than the damping in the experiments. This is possibly due to the variation of the feedwater flow rate in the simulations, the transit time for the downcomer channel and the lower plenum, or the fact that in the simulations step changes are applied, while in the experiments step changes are not possible.

In chapter 6, in which stationary reactor conditions are discussed, it is concluded that carry under is an important effect. In the dynamical problems considered in this chapter, the variation of the feedwater flow rate, due to changes in the pressure, proves to be an important effect on the time scale of several seconds. On a larger time scale, carry under is important through the effect of both the pressure and the water level on the entrainment ratio. Passive stability of the system is plausible.

Measurements at low power and low pressure show that a resonance of the circulation flow exist. In principle, the measured effect can be calculated by the simulator program. For a thorough study of the circulation flow resonance, both the model, and the model parameters will have to be adapted to the reactor start-up conditions.

General conclusions and recommendations for future research

The physics of the Dodewaard natural circulation cooled boiling water reactor was investigated successfully. The study resulted in large amount of information on the physics of the statical and dynamical behaviour of the reactor.

The method to measure the circulation flow rate (see chapters 1, 2 and 3) was developed successfully. This tool proves to be very useful in the experimental study of the reactor behaviour. The theoretically predicted standard deviation of the measured transit time shows good agreement with the measured standard deviation. In the turbulent flow calculations, performed to calibrate the circulation flow measurement technique, the three-dimensional domain was confidently collapsed into two dimensions. The propagation of a temperature fluctuation was simulated by two-dimensional calculations of stationary flow with a transient temperature field.

The literature study on the methods to monitor the in-core two-phase flow with the use of in-core neutron detector noise signals shows that further research in this field is needed. Especially the physics of the fluctuations of the local void fraction that are the cause of the neutron noise should be studied in greater detail. With the use of measurements that were performed at the Dodewaard reactor it is demonstrated that the noise signal of an in-core neutron detector contains valuable information on the local in-core two-phase flow conditions.

The theoretical model presented in chapter 5 consists of elements which are simplified and approximate representations of the processes that take place inside the reactor

vessel. The strength of the model lies in the interaction of the many subprocesses. The simulations provide a useful prediction of the general trend in the behaviour of the reactor.

In chapter 6, it is shown that carry under is an important effect in the stationary conditions of the reactor. It is shown that for the stationary conditions the inherent load following capability is restricted to high pressure. The void reactivity, through the core averaged void fraction, is very sensitive to a change in the length of the boiling section of the core.

For transient behaviour, discussed in chapter 7, the variation of the feedwater flow rate, caused by changes in the system pressure, is important. On a larger time scale, the water level and the pressure provide stabilizing feedback on the system through carry under. Measurements during start-up of the reactor indicate a resonance of the circulation flow at low power and low pressure.

Some of the parameters in the theoretical model which have a large influence on the reactor behaviour show a great uncertainty. To increase the reliability of the simulations, more research on these parameters is required.

All the models of the subprocesses in the reactor vessel can be improved, but two models are very approximate relative to their importance:

- *the carry under model.* An empirical model was applied. The model parameters were obtained from a poor collection of measurements. A theoretical model should be drawn up, and more measurements should be performed;
- *the model for the void reactivity.* The void fraction has a large influence on the void reactivity, and consequently on the power. Changes in the void fraction are often strongly space-dependent. The space dependence can in a limited sense be included in the lumped parameter model by taking the space dependent importance of the local changes of the void fraction into account.

Automatic control of the vessel water level and the reactor pressure can be implemented in the simulator program. The dynamics of the feedwater heaters can be included in the model.

With the use of the model, the reactor system can be analyzed in different ways. In this investigation, primarily numerical simulations were performed. The study can be extended to theoretical and practical system analysis. On the one hand, the set of

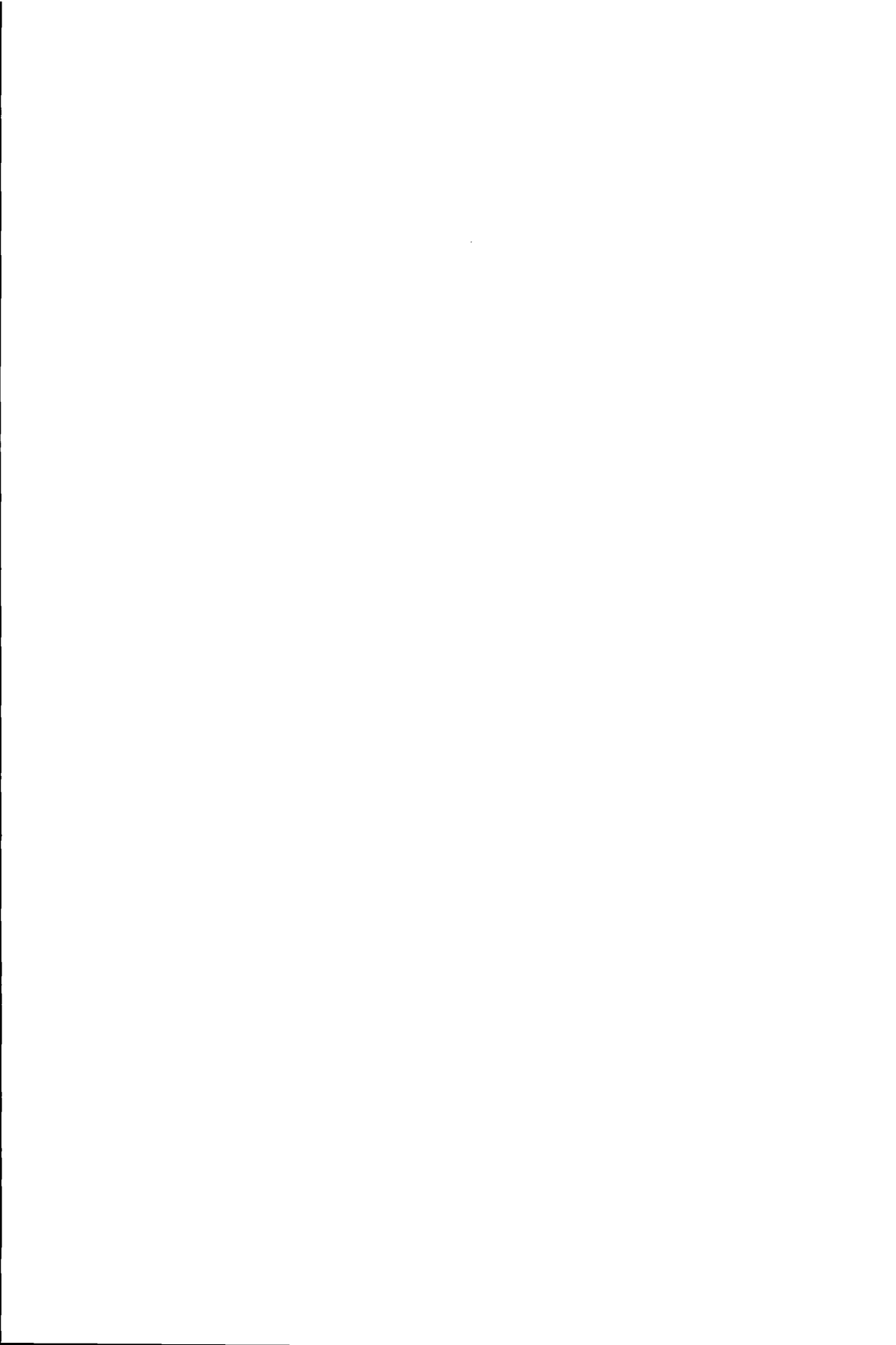
differential equations describing the system can be analyzed analytically or numerically. On the other hand, by adding noise signals or deterministic signals to various variables during a simulation, the relation between the variables can be investigated.

The feedwater temperature and the feedwater flow rate have a direct influence on the subcooling. Furthermore, the complexity of the physics involved in feedwater experiments is low, and such experiments provide basic information on reactor behaviour. Therefore, extensive measurements at various feedwater temperatures (stationary conditions), and step response experiments of the feedwater flow valve and the feedwater temperature should be performed.

The attention, which was primarily focused on the Dodewaard reactor in this investigation, can be shifted to natural circulation cooled boiling water reactors with steam/water separators, like General Electric's SBWR design. As in a BWR with steam/water separators carry under is of minor importance, the stabilizing effect of carry under is not present, and long-term passive stability is not guaranteed through this effect.

Furthermore, as carry under has a positive effect on the inherent load following capability of the reactor, passive load following can be difficult to achieve without this effect.

The circulation flow resonance at low power and low pressure is a property of all natural circulation cooled systems. System-specific investigations should be performed in order to ensure the safety of the reactor during the start-up phase.



appendix

Measurements on the Dodewaard natural circulation cooled BWR

Measurement techniques

The last few years, the experimental research on the Dodewaard-reactor has been intensified. New measurement techniques have been developed, existing techniques have been improved, and the number of parameters measured during the experiments has been increased. Furthermore, the scope of the experimental study has been broadened and experiments are performed more frequently.

The measurements are performed by a team of specialists from GKN, IRI and KEMA. GKN provides general information on the operating condition, like neutron flux levels, vessel pressure, thermal power, and steam and feedwater flow rates. IRI measures the circulation flow rate, the in-core two-phase flow velocity and monitors the system dynamics. A short description of the procedure of the noise measurements involved is given below. KEMA measures the core inlet subcooling, downcomer channel pressure drops and water temperatures, and in-core water temperatures (Wouters *et al.*, 1992a).

Noise measurements

Noise signals are used to measure the circulation flow rate (see chapter 1, 2 and 3) and the in-core two-phase flow velocity (see chapter 4). Furthermore, the system dynamics and the in-core two-phase flow conditions are monitored with the use of noise signals (see Van der Hagen, 1989, for a report on stability monitoring).

During the experiments, the signals of in-core and ex-vessel neutron detectors, downcomer thermocouples, system pressure transducer, feedwater and steam flow rate sensors, and the water level transducer are high-pass filtered for DC elimination, amplified, and recorded on magnetic tape with an FM-recorder. After the experiment, the tape is analyzed at IRI. The noise signals from tape are conditioned (anti-aliasing filtering and amplification), and digitized at a sampling rate which corresponds with the frequency range of interest. The noise signals are analyzed in the time and frequency domain with the use of noise analysis and visualization software (FFT, correlation, auto-regressive time series analysis, etc.) developed at IRI.

List of measurements

The following extensive measurements were performed in the period 1989-1993:

- Start-up - wide pressure range (pressure increase from 2 bar to 75.5 bar; Van der Hagen *et al.*, 1992a);
- Start-up - focusing on the dynamics at low pressure and low power (pressure increase from 2 bar to 10 bar; Van der Hagen *et al.*, 1993c);
- Shut-down (power decrease from 183 MW to 30 MW at a constant pressure of 75.5 bar; Van der Hagen *et al.*, 1993b);
- System pressure variation (pressure decrease from 75.5 bar to 60 bar, starting with a power of 166 MW at 75.5 bar; Van der Hagen *et al.*, 1993a).
- Vessel water level variation (water level variation between 0.45 m and 1.24 m, starting with a power of 163 MW at 0.57 m; Wouters *et al.*, 1992b, 1992c; Van der Hagen, 1991);
- Full load conditions at four instants spread over one fuel cycle.

For the near future, the following measurements are planned:

- Shut-down at 60 bar (power decrease from 183 MW to 30 MW at a constant pressure of 60 bar; due January 1994);
- Start-up - focusing on the dynamics at low pressure and low power (pressure increase from 2 bar to 5 bar, and a power variation at each pressure point; due February 1994).

Summary

In this thesis, the statics and dynamics of natural circulation cooled boiling water reactors (BWR) are discussed. The physics governing the reactor behaviour is analyzed with the use of experiments and simulations. Primarily, the behaviour of the Dodewaard natural circulation cooled BWR (The Netherlands) is studied, but more general results are presented also.

In natural circulation BWRs, the circulation flow depends on the density difference between the water in the downcomer channel (the channel between the vessel wall and the core/riser), and the two-phase flow in the core and the riser. In this respect, compared to forced circulation BWRs, natural circulation cooled BWRs have an additional dependent variable. Moreover, in the Dodewaard reactor free surface steam-water separation takes place in the upper plenum. The separation is not perfect - some steam is dragged into the downcomer channel. This effect, called carry under, influences the driving force of the circulation flow and the level of subcooling of the core inlet flow.

Because of the above-mentioned complications, it is very difficult to predict the behaviour of the Dodewaard reactor by a simple deduction with the use of the laws of physics. In order to gain insight into the complex of physical processes governing the reactor behaviour, stationary conditions and transients are studied both experimentally and with the use of model calculations.

For the experimental study, a tool to measure the circulation flow rate is developed. The method is based on the cross-correlation flow measurement technique. Theoretical and practical aspects of the noise analysis methods involved in this technique are discussed. The technique is calibrated by performing calculations on turbulent flow.

These calculations comprise two- and three-dimensional calculations of stationary flow, and two-dimensional calculations with stationary flow and transient thermal characteristics. With the latter calculations, the transportation of a temperature fluctuation is simulated.

Possibilities of monitoring the in-core two-phase flow with the use of the noise signal of in-core neutron detectors are studied. A literature survey on this subject is included in this thesis. It is concluded that the neutronic processes involved in the neutron noise are quite well understood. However, more research on the origin and the characteristics of the density fluctuations that cause the noise is needed. The technique of monitoring the in-core two-phase flow with the use of a single in-core neutron detector is illustrated by measurements performed on the Dodewaard reactor.

For the theoretical study, a model for the main physical processes in the reactor vessel is drawn up. The model consists of elements of neutronics, thermodynamics, and hydraulics. Simple models are applied - the strength of the complete set of models lies in the interaction of the various processes. The model is designed to simulate stationary conditions and slow transients. For the stationary conditions, the pressure, the power (or the excess reactivity of the core), the water level and the feedwater temperature are taken as the independent variables. For the transients, the external reactivity, the feedwater temperature and the opening of the steam and feedwater flow valve are taken as the independent variables. The general trend in the measurements is reasonably well simulated.

Both the measurements and the simulations show that carry under is an important effect. For stationary conditions at various pressures, the carry under and the moderator temperature reactivity have an influence on the reactivity that is opposite to influence of the steam density. As the importance of these three effects changes as a function of the pressure, the load following capability is restricted to high pressure. For transient behaviour, the variation of the feedwater flow rate, caused by changes in the pressure, is important. Measurements during start-up of the reactor indicate a resonance of the circulation flow at low power and low pressure.

It is demonstrated that the Dodewaard reactor is passively stable on all time-scales.

Samenvatting

In dit proefschrift worden de statica en de dynamica van natuurlijke-circulatie kokend-waterreactoren (BWR) besproken. De fysica achter het gedrag wordt bestudeerd aan de hand van experimenten en simulaties. In de eerste plaats wordt het gedrag van de natuurlijke-circulatie BWR in Dodewaard (Nederland) geanalyseerd, maar meer algemeen geldige resultaten worden ook gepresenteerd.

Bij natuurlijke-circulatie BWR's hangt het circulatiedebiet af van het dichtheidsverschil tussen het water in het valkanaal (het kanaal tussen de wand van het reactorvat en de schoorsteen/kern) en de tweefasenstroming in de kern en de schoorsteen. In dit opzicht heeft een natuurlijke-circulatie BWR één afhankelijke variabele meer dan een BWR met geforceerde koeling. Hier komt nog bij dat in de Dodewaard-reactor stoom/water-scheiding plaatsvindt aan een vrij oppervlak. Deze scheiding is niet perfect - een deel van de stoom wordt meegesleurd in het valkanaal. Dit effect, dat *carry under* wordt genoemd, beïnvloedt de drijvende kracht van de circulatiestroming en de mate van onderkoeling van het koelwater aan de inlaat van de kern.

Door de bovenstaande complicerende factoren is het erg moeilijk om, uitgaande van eenvoudige afleidingen met behulp van de wetten van de fysica, het gedrag van de Dodewaard-reactor te voorspellen. Om inzicht te verkrijgen in het netwerk van fysische processen dat het gedrag van de reactor bepaalt, zijn stationaire toestanden en het tijdsafhankelijk gedrag bestudeerd met behulp van metingen en numerieke simulaties.

Voor het experimentele gedeelte van de studie is een meetmethode ontwikkeld om het circulatiedebiet te meten. Deze methode is gebaseerd op de kruiscorrelatie-debietmeetmethode. Theoretische en praktische aspecten van de ruisanalysetechnieken die gebruikt worden bij deze methode worden behandeld in dit proefschrift. De meetmethode is gekalibreerd door numerieke simulaties van turbulente stroming uit te

voeren. Deze simulaties omvatten twee- en driedimensionale berekeningen van stationaire stromingen en tweedimensionale berekeningen van stationaire stromingen met een tijdsafhankelijk temperatuurveld. Met de laatstgenoemde berekeningen wordt het transport van een temperatuurfluctuatie gesimuleerd.

De mogelijkheden om de tweefasenstroming die in de kern optreedt te bestuderen, uitgaande van het ruissignaal van een neutronendetector die zich in de kern bevindt, worden besproken. Een literatuurstudie over deze toepassing wordt behandeld in dit proefschrift. Er wordt geconcludeerd dat de neutronenfysische processen die van belang zijn bij neutronendetectorruis goed worden begrepen. Er is echter meer onderzoek nodig naar de oorsprong en de aard van de dichtheidsfluctuaties die de neutronenruis veroorzaken. De techniek van het bestuderen van de tweefasenstroming in de kern uitgaande van het ruissignaal van een neutronendetector die zich in de kern bevindt wordt toegelicht met metingen die gedaan zijn aan de Dodewaard-reactor.

Voor het theoretische gedeelte van de studie is een model voor de belangrijkste fysische processen in het reactorvat opgesteld. Het model bestaat uit elementen uit de neutronica, thermodynamica en stromingsleer. Eenvoudige modellen zijn toegepast - de kracht van de volledige set van modellen vloeit voort uit de interactie van de verschillende processen. Het model is ontworpen om stationaire toestanden en langzaam tijdsafhankelijk gedrag te simuleren. In het model zijn voor de stationaire toestanden de druk, het vermogen (of de toegevoegde reactiviteit van de reactorkern), het waterniveau en de voedingswatertemperatuur de onafhankelijke variabelen. Voor de tijdsafhankelijke simulaties zijn de externe reactiviteit, de voedingswatertemperatuur en de openingen van de stoom- en de voedingswaterklep de onafhankelijke variabelen. Het globale gedrag dat volgt uit de metingen wordt redelijk goed gesimuleerd.

Uit zowel de metingen als uit de simulaties volgt dat *carry under* een belangrijk effect is. Bij stationaire toestanden bij verschillende druk hebben *carry under* en het reactiviteitseffect van de moderator temperatuur een invloed op de reactiviteit die tegengesteld is aan de invloed van de stoomdichtheid. Omdat de grootte van de invloed van deze drie effecten van de druk afhangt, is de *load following* mogelijkheid van de reactor beperkt tot hoge druk. Bij het tijdsafhankelijk gedrag is de verandering van het voedingswaterdebiet, dat wordt veroorzaakt door de verandering van de druk, belangrijk. Metingen die gedaan zijn tijdens de opstartfase van de reactor wijzen op een resonantie van het circulatiedebiet bij laag vermogen en lage druk.

Er wordt gedemonstreerd dat de Dodewaard-reactor een passief-stabiel systeem is op alle tijdschalen.

Nomenclature

List of symbols

| | | |
|-------------|--|----------------------------------|
| a | constant in the model for the integrated linear power | W m^{-1} |
| A | operator in the field-of-view analysis | |
| | valve opening | |
| | area | m^2 |
| A_{gv} | constant in the gate valve model | |
| b | constant in the model for the integrated linear power | W |
| c | constant in the two-phase flow friction model | m^{-5} |
| c_1 | constant in the feedwater injection model | kg s^{-1} |
| c_2 | constant in the feedwater injection model | |
| c_{cf} | constant in the two-phase flow friction model | m^{-4} |
| c_{cu} | constant in the carry under model | |
| c_{cuh} | constant in the carry under model | m^{-1} |
| c_{cup} | constant in the carry under model | $\text{m}^2 \text{N}^{-1}$ |
| c_{pf} | specific heat of the fuel | $\text{J kg}^{-1} \text{K}^{-1}$ |
| C | constant in the model for flow around support rings | m^{-1} |
| | constant in the two-phase flow noise model | |
| | constant in the valve flow rate model | m^{-4} |
| C_{gv} | constant in the gate valve model | |
| C_i | 'concentration' of the neutron precursors in group i | W |
| C_w | drag coefficient for flow around objects | |
| D | transit time | s |
| e | mathematical constant; $e \approx 2.7182818$ | |
| E | neutron energy | J |
| f | frequency | Hz |
| | form factor for the flow distribution | |
| | fraction of the core length | |
| f_p | axial peaking factor | |
| g | constant in the two-phase flow noise model | |
| | gravitational acceleration | m s^{-2} |
| $G_{ii}(f)$ | auto-power spectral density of signal i | |
| $G_{ij}(f)$ | cross-power spectral density of signals i, j | |

| | | |
|-----------------|---|--------------------|
| h | water level | m |
| | specific enthalpy | J kg ⁻¹ |
| Δh_{gt} | heat of evaporation | J kg ⁻¹ |
| I | integral of the linear power | W |
| j | imaginary unit; $j^2 = -1$ | |
| K | valve friction coefficient | |
| l | length | m |
| m | constant in the two-phase flow noise model | |
| | vessel mass content | kg |
| $n_i(t)$ | temperature noise influence i | K |
| p | pressure | N m ⁻² |
| Δp | pressure drop | N m ⁻² |
| P | nuclear power | W |
| | average heat rate | W |
| q' | linear heat rate | W m ⁻¹ |
| q'_0 | coefficient for the shape of the linear heat rate | W m ⁻¹ |
| q'_1 | coefficient for the shape of the linear heat rate | W m ⁻¹ |
| Q | work | J |
| r | position vector | m |
| r | reactivity coefficient | -, K ⁻¹ |
| | radial position | m |
| $R(\omega)$ | spectrum of the detector count rate | |
| $R_y(\tau)$ | cross-covariance function of signals i, j | |
| R_f | radius of the fuel pins | m |
| R_{MN} | two-phase flow friction multiplier | |
| s | standard deviation | |
| $s(t)$ | common signal in the thermocouple noise model | |
| S | slip factor for two-phase flow | |
| t | time | s |
| T | measurement time | s |
| | temperature | K |
| u | velocity component in the fluid flow calculations | m s ⁻¹ |
| u | specific internal energy | J kg ⁻¹ |
| U_{sat} | internal energy of the saturated water/steam system | J |
| v | velocity vector | m s ⁻¹ |
| v | velocity component in the fluid flow calculations | m s ⁻¹ |
| | velocity | m s ⁻¹ |
| V | volume | m ³ |
| w | velocity component in the fluid flow calculations | m s ⁻¹ |
| $w(r, \omega)$ | weight function | |
| x_i | thermocouple noise signal i | K |
| z | axial position | m |

| | | |
|------------------------------|--|----------------------------------|
| α | attenuation factor in the thermocouple signal model void fraction | |
| α_{fc} | fuel-to-coolant heat transfer coefficient | $\text{W m}^{-2} \text{K}^{-1}$ |
| β | total fraction of delayed neutrons | |
| β_i | fraction of delayed neutrons of group i | |
| $\gamma_{ij}^2(f)$ | coherence function for signals i, j | |
| θ | azimuthal angle | rad |
| λ_i | decay constant of neutron precursor group i | s^{-1} |
| Λ | neutron generation time | s |
| π | mathematical constant; $\pi \approx 3.1415927$ | |
| ρ | density reactivity | kg m^{-3} |
| σ | standard deviation | |
| $\Sigma_d(r, \omega)$ | macroscopic detector cross-section | m^{-1} |
| τ | time shift in the cross-covariance function transit time | s s |
| τ_f | effective time constant of the fuel | s |
| ϕ | mass flow rate | kg s^{-1} |
| ϕ'' | downcomer water mass flux | $\text{kg m}^{-2} \text{s}^{-1}$ |
| φ | neutron flux density | $\text{m}^{-2} \text{s}^{-1}$ |
| χ | flow quality | |
| Ψ | entrainment ratio | |
| $\psi(f)$ | weight function | |
| $\psi(r, \omega, E, \Omega)$ | importance function | |
| ω | angular frequency | rad s^{-1} |
| Ω | direction vector | |

Superscripts

| | |
|----------|--|
| ' | per unit length |
| " | per unit area |
| * | complex conjugate new value |
| d | detector |
| (g) | generalized formulation |
| HT | according to the Hannan-Thomson processing |
| α | void fraction |

Subscripts

| | |
|---------|---|
| 0 | normalized base |
| 2ϕ | two-phase flow |
| b | with water at saturation conditions (boiling) |
| c | core calculated circulating |
| ca | flow acceleration in the core |

| | |
|-------------|---|
| <i>cf</i> | flow friction in the core |
| <i>ci</i> | core inlet |
| <i>co</i> | core outlet |
| <i>d</i> | downcomer driving |
| <i>dc</i> | downcomer, next to the core |
| <i>di</i> | downcomer inlet |
| <i>dr</i> | downcomer, next to the riser |
| <i>ds</i> | downcomer, at sparger level downcomer, from inlet to sparger |
| <i>D</i> | Doppler |
| <i>ext</i> | external |
| <i>f</i> | feedwater fuel |
| <i>fw</i> | feedwater |
| <i>g</i> | steam |
| <i>gd</i> | steam in the downcomer channel above the feedwater sparger |
| <i>gdi</i> | steam at the downcomer inlet |
| <i>gds</i> | steam in the downcomer at the feedwater sparger level |
| <i>go</i> | steam out of the vessel |
| <i>gv</i> | gate valve |
| <i>h=0</i> | at zero water level |
| <i>i</i> | group index of delayed neutrons index of flow sections in the circulation flow loop |
| <i>l</i> | water |
| <i>ld</i> | water in the downcomer channel above the feedwater sparger |
| <i>ldi</i> | water at the downcomer inlet |
| <i>lds</i> | water in the downcomer at the feedwater sparger level |
| <i>lp</i> | lower plenum |
| <i>lsat</i> | water at saturation conditions |
| <i>m</i> | measured |
| <i>nb</i> | with subcooled water (non-boiling) |
| <i>p</i> | predicted |
| <i>r</i> | riser |
| <i>rc</i> | downcomer, at the top core/bottom riser level downcomer, from the sparger to the top of the core |
| <i>rc/p</i> | downcomer, from the top of the core to the lower plenum |
| <i>ro</i> | riser outlet |
| <i>sat</i> | at saturation conditions |
| <i>t</i> | total |
| <i>T</i> | temperature |
| <i>u</i> | uniform |
| <i>up</i> | upper plenum |
| <i>v</i> | vessel valve |
| α | void fraction |

Operators

| | |
|---------------------|---------------------------------|
| A | transport or diffusion operator |
| $E[x]$ | expected value of x |
| \hat{x} | estimation of x |
| $var[x]$ | variance of x |
| x^* | complex conjugate of x |
| $\langle x \rangle$ | average value of x |
| δx | fluctuating part of x |
| Δx | change of x |

List of abbreviations

| | |
|-------|--|
| APSD | auto-power spectral density |
| ATIP | automatically traversing in-core probe |
| BORAX | boiling reactor experiments |
| BWR | boiling water reactor |
| CCF | cross-covariance function |
| CPSD | cross-power spectral density |
| CPU | central processing unit |
| DNB | departure from nuclear boiling |
| EBWR | experimental boiling water reactor |
| FFT | fast Fourier transform |
| FM | frequency modulation |
| GE | General Electric |
| GKN | Gemeenschappelijke Kernenergiecentrale Nederland N.V. |
| IRI | Interfaculty Reactor Institute |
| KEMA | N.V. tot Keuring van Elektrotechnische Materialen |
| NA | not available |
| NRMS | normalized root mean square |
| pcm | 10^{-5} |
| QUICK | quadratic upwind scheme |
| RAS | <i>reactor afkoel systeem</i> (reactor cooling system) |
| RMS | root mean square |
| SBWR | simplified boiling water reactor |
| SPERT | special power excursion reactor test |
| TIP | traversing in-core probe |
| VBWR | Vallecitos boiling water reactor |



References

- Albrecht R.W., Crowe R.D., Dailey D.J. and Kosály G. (1981) *Advances in Test Measurement* 1-I, 335
- Albrecht R.W., Crowe R.D., Dailey D.J., Damborg M.J. and Kosály G. (1982) *Prog. Nucl. Energy* **9**, 37
- Analytis G.Th. (1980) *Ann. Nucl. Energy* **7**, 685
- Analytis G.Th. (1981) *Ann. Nucl. Energy* **8**, 349
- Analytis G.Th. (1982a) *Ann. Nucl. Energy* **9**, 53
- Analytis G.Th. (1982b) *Ann. Nucl. Energy* **9**, 417
- Analytis G.Th. (1982c) *Ann. Nucl. Energy* **9**, 591
- Analytis G.Th. (1982d) *Ann. Nucl. Energy* **9**, 601
- Analytis G.Th. (1983a) *Ann. Nucl. Energy* **10**, 101
- Analytis G.Th. (1983b) *Ann. Nucl. Energy* **10**, 379
- Analytis G.Th. and Lübbsmeyer D. (1983c) *Trans. Am. Nucl. Soc.* **45**, 845
- Analytis G.Th. and Lübbsmeyer D. (1983d) *Trans. Am. Nucl. Soc.* **45**, 846
- Analytis G.Th. and Lübbsmeyer D. (1984a) *Trans. Am. Nucl. Soc.* **47**, 522
- Analytis G.Th. and Lübbsmeyer D. (1984b) *Trans. Am. Nucl. Soc.* **47**, 524
- Analytis G.Th. and Lübbsmeyer D. (1984c) *Prog. Nucl. Energy* **14**, 95
- Analytis G.Th. and Lübbsmeyer D. (1985) *Prog. Nucl. Energy* **15**, 621
- Ando Y., Naito N., Tanabe A. and Kitamura N. (1975) *J. Nucl. Sci. Technol.* **12**, 597
- Beck M.S. and Płaskowski A. (1987) *Cross correlation flowmeters - their design and application*, Adam Hilger, Bristol, England
- Behringer K., Kosály G. and Kostić Lj. (1977) *Nucl. Sci. Engng* **63**, 306
- Behringer K., Kosály G. and Pázsit I. (1979) *Nucl. Sci. Engng* **72**, 304
- Behringer K. and Crowe R. (1981) *Atomkernenergie* **38**, 47
- Behringer K. (1983) *Ann. Nucl. Energy* **10**, 433
- Behringer K., Spiekerman G. and Yadigaroglu G. (1985) *Prog. Nucl. Energy* **15**, 95
- Bell G.I. and Glasstone S. (1970) *Nuclear reactor theory*, Van Nostrand Reinhold Company, New York, USA
- Bernard P., Cloue J. and Messainguiral C. (1982) *Prog. Nucl. Energy* **9**, 581

- Bertora F., Braccini C., Gambardella G. and Musso G. (1975) *Study on the use of the fast Fourier transform in spectral analysis*, report ESA(ESRO)CR-468, vol. 2, European Space Agency, Genova, Italy
- Biesheuvel A. and Gorissen W.C.M. (1990) *Int. J. Multiphase Flow* **16**, 211
- Bouré J.A., Bergles A.E. and Tong L.S. (1973) *Nucl. Eng. and Design* **25**, 165
- Boyd L.R. (1959) *Nucleonics* **17-3**, 96
- Burden R.L. and Faires J.D. (1985) *Numerical Analysis*, PWS-Kent, Boston, USA
- Ceelen D., Gebureck P. and Stegemann D. (1976) *Atomkernenergie* **27**, 239
- Chiang J.H., Aritomi M., Inoue R. and Mori M. (1992) *proc. of NURETH-5, 5th International topical meeting on reactor thermal hydraulics*, 21-24 September, 1992, Salt Lake City, UT, USA
- Cohen K. and Zebroski E. (1959) *Nucleonics* **17-3**, 63
- Colenbrander G.W. (1991) *Applied Scientific Research* **48**, 211, or: Oliemans R.V.A. (ed.), *Computational fluid dynamics for the petrochemical process industry*, p. 1-35, Kluwer Academic Publishers, The Netherlands
- Cortzen F.W. (1988) *H2OTP computer program*, RISOE
- Defloor J. and Baeyens R. (1988) *Prog. Nucl. Energy* **21**, 547
- Difilippo F.C. and Otaduy P.J. (1980a) *Nucl. Sci. Engng* **75**, 258
- Difilippo F.C. (1980b) *Trans. Am. Nucl. Soc.* **35**, 592
- Difilippo F.C. (1982) *Nucl. Sci. Engng* **80**, 211
- Difilippo F.C. (1984) *Ann. Nucl. Energy* **11**, 89
- Dolgov V.V., Sergeyev Yu.A., Kochetkov L.A., Malamud V.A., Samoylov O.B., Flyorov L.N., Mityaev Yu.I., Mihan V.I. and Cherkashov Yu.M. (1990) *proc. of ENC-90*, 23-28 September, 1990, Lyon, France, ENS/ANS-Foratom
- Duderstadt J.J. and Hamilton L.J. (1976) *Nuclear reactor analysis*, John Wiley & sons, New York, USA
- El-Wakil M.M. (1978) *Nuclear heat transport*, American Nuclear Society, Illinois, USA
- Federico A., Galli C., Parmeggiani C., Ragona R. and Tosi V. (1982) *Prog. Nucl. Energy* **9**, 631
- FLUENT User's Manual (1990) create.x Incorporated, Hanover, New Hampshire, England
- Fuge R., Valkó J., Czibók T., Kätzmer D. and Vasilescu M. (1977) *Ann. Nucl. Energy* **4**, 161
- Gebureck P., Singh O.P. and Stegemann D. (1977) *Prog. Nucl. Energy* **1**, 187
- George W.K. and Arndt R. (1989) *Advances in Turbulence*, Hemisphere publishing corporation, New York, USA
- GKN (1965) *Inspectie reactorvat stomp N20*, drawing 51W-1-09601 page 7, GKN, Dodewaard, The Netherlands
- Goldstein R. and Shotkin L.M. (1969) *Nucl. Sci. Engng* **38**, 94
- Haghighat A. and Kosály G. (1985) *Ann. Nucl. Energy* **12**, 357
- Haghighat A. (1986) *Determination of the sensitivity volume of a BWR incore detector*, PhD thesis, University of Washington, Washington, USA
- Haghighat A. and Kosály G. (1989) *Nucl. Sci. Engng* **101**, 8
- Hoogenboom J.E., Van Meulenbroek B.H., Van Dam H. and Kleiss E.B.J. (1985) *Prog. Nucl. Energy* **15**, 771

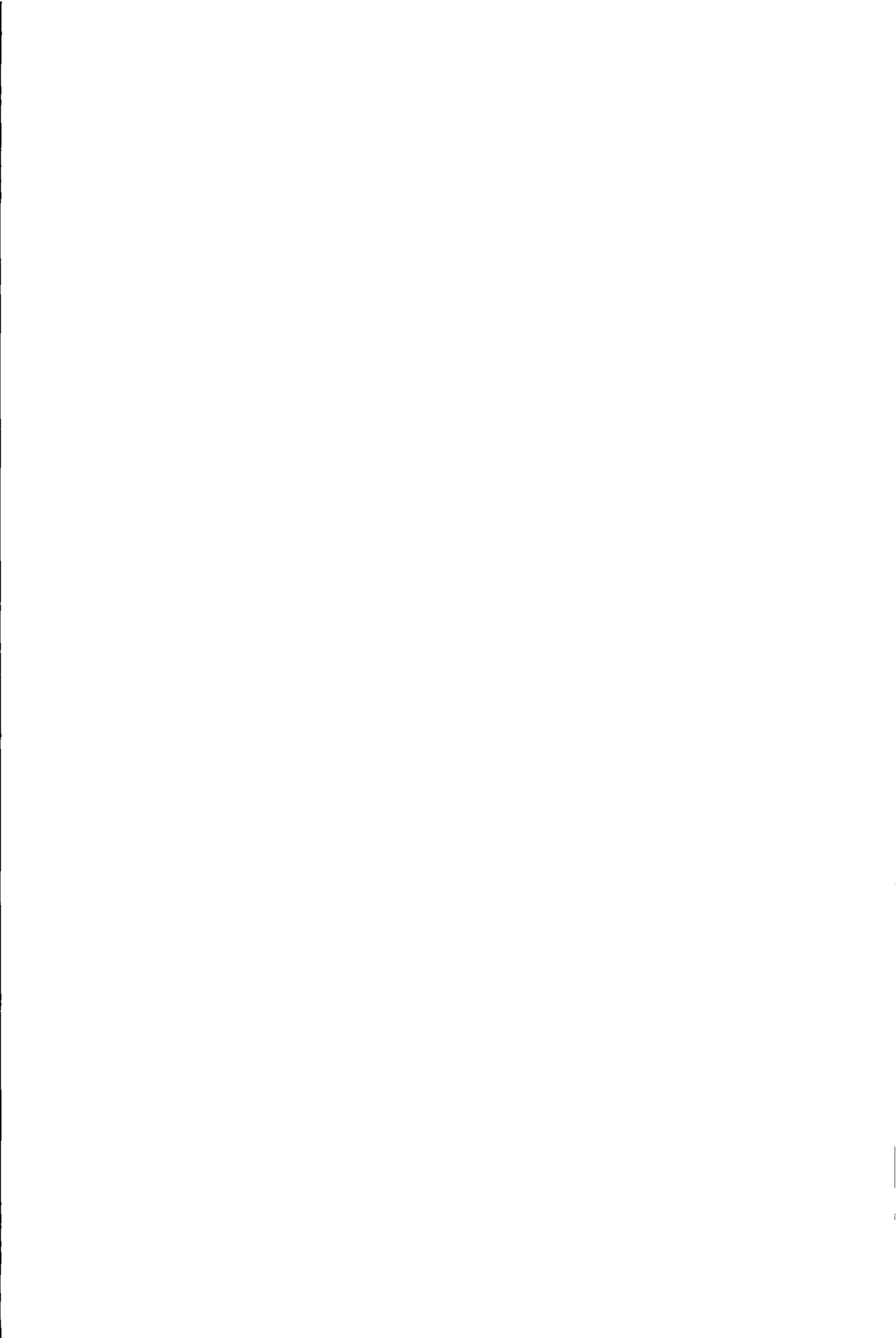
- Hummel R. and Wesser U. (1988) *Prog. Nucl. Energy* **21**, 333
- Janssen L.P.B.M. and Warmoeskerken M.M.C.G. (1987) *Transport phenomena data companion*, Edward Arnold, London / Delftse uitgevers maatschappij, Delft, The Netherlands
- John T.M. and Singh O.P. (1980) *Ann. Nucl. Energy* **7**, 569
- John T.M. and Singh O.P. (1983) *Ann. Nucl. Energy* **10**, 643
- Jones O.W. Jr. and Zuber N. (1975) *Int. J. Multiphase flow* **2**, 273
- Kanemoto S., Tsunoyama S., Andoh Y., Yamamoto F. and Sandoz S.A. (1984) *Nucl. Technol.* **67**, 23
- Katona T. (1985) *Prog. Nucl. Energy* **15**, 685
- Katona T. and Kozma R. (1988) *Prog. Nucl. Energy* **21**, 431
- Khan H.J. and Kosály G. (1984) *Ann. Nucl. Energy* **11**, 477
- King C.H., Ouyang M.S., Pei B.S. and Wang Y.W. (1988) *Nucl. Technol.* **82**, 211
- King C.H., Ouyang M.S., Pei B.S. and Lee S.C. (1989) *Nucl. Technol.* **86**, 70
- Kitamura M., Matsubara K. and Oguma R. (1977) *Prog. Nucl. Energy* **1**, 231
- Kleiss E.B.J. and Van Dam H. (1979) *Ann. Nucl. Energy* **6**, 385
- Kleiss E.B.J. and Van Dam H. (1981) *Nucl. Technol.* **53**, 250
- Kleiss E.B.J. (1982) private communication
- Kleiss E.B.J. (1983) *On the determination of boiling water characteristics by noise analysis*, PhD thesis, Delft University of Technology, Delftse Universitaire Pers, Delft, The Netherlands
- Kleiss E.B.J. (1984) *Resultaten van analyse van thermokoppel-ruissignalen in het valkanaal van de Dodewaard reactor*, report IRI-131-84-02, Delft University of Technology, Delft, The Netherlands (in Dutch)
- Kleiss E.B.J. and Van der Hagen T.H.J.J. (1985a) *Analysis and evaluation of stability experiments performed in the Dodewaard reactor on December 5 and 6, 1984*, report IRI-131-85-02, Delft University of Technology, Delft, The Netherlands
- Kleiss E.B.J. and Van Dam (1985b) *Ann. Nucl. Energy* **12**, 233
- Knapp C.H. and Carter G.C. (1976) *IEEE Trans. Acoust., Speech, Signal Processing*, **24-4**, 320
- Kosály G., Maróti L. and Meskó L. (1975) *Ann. Nucl. Energy* **2**, 315
- Kosály G. and Meskó L. (1976) *Ann. Nucl. Energy* **3**, 233
- Kosály G., Kostić Lj., Miteff L., Varadi G. and Behringer K. (1977) *Prog. Nucl. Energy* **1**, 99
- Kosály G. (1980) *Prog. Nucl. Energy* **5**, 145
- Kosály G., Albrecht R.W., Crowe R.D. and Dailey D.J. (1982a) *Prog. Nucl. Energy* **9**, 23
- Kosály G. and Sanchez R. (1982b) *Trans. Am. Nucl. Soc.* **41**, 620
- Kosály G. (1983) *Ann. Nucl. Energy* **10**, 675
- Kosály G. and Sanchez R. (1985) *Prog. Nucl. Energy* **15**, 611
- Kozma R. (1991) *proc. of SMORN VI - A symposium on nuclear reactor surveillance and diagnostics* (ed. Kryter R.C. and Upadhyaya B.R.) 19-24 May, 1991, Gatlinburg, Tennessee, U.S.A., **1**, 38.01, Oak Ridge National Laboratory / The University of Tennessee, Knoxville, USA

- Kozma R. (1992a) *Nuclear noise investigations on boiling effects in a simulated MTR-type fuel assembly*, PhD thesis, Delft University of Technology, Delft, The Netherlands
- Kozma R., van Dam H. and Hoogenboom J.E. (1992b) *Nucl. Technol.* **100**, 97
- Kramer A.W. (1958) *Boiling water reactors*, Addison-Wesley Publishing Company, Reading, Massachusetts, USA
- Lahey R.T. and Moody F.J. (1977) *The thermal-hydraulics of a boiling water nuclear reactor*, American Nuclear Society, USA
- Lauder B.E. (1991) *Applied Scientific Research* **48**, 247, or: Oliemans R.V.A. (ed.), *Computational fluid dynamics for the petrochemical process industry*, p. 37-59, Kluwer Academic Publishers, The Netherlands
- Lewins J. (1978) *Nuclear reactor kinetics and control*, Pergamon press, Oxford, England
- Lübbesmeyer D. (1983a) *Ann. Nucl. Energy* **10**, 233
- Lübbesmeyer D. (1983b) *Ann. Nucl. Energy* **10**, 421
- Lübbesmeyer D. (1983c) *Ann. Nucl. Energy* **10**, 677
- Lübbesmeyer D. and Leoni B. (1983d) *Int. J. Multiphase flow* **9**, 665
- Lübbesmeyer D. (1984) *Prog. Nucl. Energy* **14**, 41
- Lübbesmeyer D. and Analytis G.Th. (1985) *Prog. Nucl. Energy* **15**, 635
- Lützw K., Moraweg U. and Prasser H.M. (1983) *Energietechnik* **33**, 404
- Lützw K. and Stäck D. (1987a) *Kernenergie* **30**, 114
- Lützw K., Wegner D. and Gorburov V.I. (1987b) *Kernenergie* **30**, 442
- Lützw K. and Wegner D. (1990) *Kernenergie* **33**, 133
- March-Leuba J. and King W.T. (1988) *Prog. Nucl. Energy* **21**, 181
- Matsubara K., Oguma R. and Kitamura M. (1978) *Nucl. Sci Engng* **65**, 1
- Matuszkiewics A., Flamand J.C. and Bouré J.A. (1987) *Int. J. Multiphase Flow* **13**, 199
- McCandless R.J. and Redding J.R. (1989) *Nuclear Engineering International*, November 1989, 20
- Miida J. and Suda N. (1963) *Derivation of transfer functions of natural circulation boiling water reactor*, report JAERI 1044, Tokai-mura, Naka-gun, Ibaraki-ken, Japan
- Miida J. and Suda N. (1964) *Dynamic analysis of natural circulation boiling water reactor*, report JAERI 1061, Tokai-mura, Naka-gun, Ibaraki-ken, Japan
- Mingchang Z. and Gouzhen Z. (1981) *Nucl. Technol.* **54**, 9
- Miteff L. and Behringer K. (1982) *Prog. Nucl. Energy* **9**, 649
- Mitsutake T., Tsunoyama S., Kanemoto S., Namba H. and Sandoz S.A. (1984) *Nucl. Technol.* **65**, 365
- Neal L.G. and Zivi S.M. (1967) *Nucl. Sci. Engng* **30**, 25
- Nissen W.H.M. (1988) *Verslag van enkele uitgevoerde metingen tijdens de voorverwarmertest op 23 november 1988*, report Fysica 88-38, GKN, Dodewaard, The Netherlands (in Dutch)
- Nissen W.H.M. (1993) private communication Nis/ALi 93-0365
- Oosterkamp W.J. (1983) *KEMA Scientific & Technical Reports* **1** (7), 75, KEMA, Arnhem, The Netherlands

- Oosterkamp W.J. (1987) *KEMA Scientific & Technical Reports* 5, 219, KEMA, Arnhem, The Netherlands
- Pauchon C. and Bannerjee S. (1986) *Int. J. Multiphase Flow* 12, 559
- Pázsit I. (1981) *Ann. Nucl. Energy* 8, 393
- Peyret R. and Taylor T.D. (1983) *Computational methods for fluid flow*, Springer Verlag, New York, USA
- Pór G., Horányi S. and Dikanarov O.J. (1984) *Ann. Nucl. Energy* 11, 197
- Pór G., Glöckler O. and Rindelhardt U. (1988) *Prog. Nucl. Energy* 21, 555
- Priestley M.B. (1981) *Spectral analysis and time series*, Academic press, London, England
- Randall R.L. and Pekrul P.J. (1967) in: Uhrig R.E. (Coordinator) *Neutron noise, waves, and pulse propagation*, U.S. Atomic Energy Commission, USA
- Saiz-Jabardo J.M. and Bouré J.A. (1989) *Int. J. Multiphase Flow* 15, 483
- Seifritz W. (1972) *Atomkernenergie* 19, 271
- Seifritz W. and Cioli F. (1973) *Trans. Am. Nucl. Soc.* 17, 451
- Singh O.P. and Stegemann D. (1978) *Atomkernenergie* 31, 74
- Stekelenburg A.J.C., Van der Hagen T.H.J.J. and Nissen W.H.M. (1991) proc. of *SMORN VI - A symposium on nuclear reactor surveillance and diagnostics* (ed. Kryter R.C. and Upadhyaya B.R.) 19-24 May, 1991, Gatlinburg, Tennessee, U.S.A., 1, 37.01, Oak Ridge National Laboratory / The University of Tennessee, Knoxville, USA
- Stekelenburg A.J.C. and Van der Hagen T.H.J.J. (1992a) paper presented at the IAEA Technical Committee Meeting on *in-core instrumentation and in-situ measurement in connection with fuel behaviour*, 26-28 October, 1992, Petten, The Netherlands
- Stekelenburg A.J.C. (1992b) *Literature on the relation between reactor noise and two-phase flow dynamics*, report IRI-131-92-013, Delft University of Technology, Delft, The Netherlands (in Dutch)
- Suda N. (1985) *Prog. Nucl. Energy* 15, 437
- Suessbrich R. (1978) *H2O computer program (based on VDI steam tables and other improved publications)*, Uhde GmbH, Dortmund, Germany
- Sweeney F.J. (1978) *Trans. Am. Nucl. Soc.* 30, 743
- Sweeney F.J. (1979) *Trans. Am. Nucl. Soc.* 33, 854
- Sweeney F.J. and Robinson J.C. (1980) *Trans. Am. Nucl. Soc.* 34, 802
- Termaat K.P. (1969) *Theoretisch afgeleide correctiefactoren toe te passen op de meetresultaten van de kruiscorrelatiemethode ter bepaling van watersnelheden*, report GKN-FYS-69-03, GKN, Dodewaard, The Netherlands (in Dutch)
- Termaat K.P. (1970) *J. Phys.E:Sci.Instrum.* 3, 589
- Termaat K.P. (1991) private communication
- Todreas N.E. and Kazimi M.S. (1990a) *Nuclear systems I - Thermal hydraulic fundamentals*, Hemisphere publishing corporation, New York, USA
- Todreas N.E. and Kazimi M.S. (1990b) *Nuclear systems II - Elements of thermal hydraulic design*, Hemisphere publishing corporation, New York, USA
- Upadhyaya B.R. and Kitamura M. (1981) *Nucl. Sci. Engng* 77, 480
- Valkó J. and Meskó L. (1977) *Prog. Nucl. Energy* 1, 205
- Van Dam H. (1975) *Atomkernenergie* 24, 70

- Van Dam H. (1976) *Atomkernenergie* **27**, 8
- Van Dam H. (1977) *Ann. Nucl. Energy* **4**, 185
- Van Dam H. (1992) *Rep. Prog. Phys.* **7**, 2025
- Van de Graaf R. (1993) private communication
- Van de Graaf R., Van der Hagen T.H.J.J. and Mudde R.F. (1994) accepted for publication in *Nuclear Technol.*
- Van der Hagen T.H.J.J. (1986) *Stability analysis of the Dodewaard BWR concerning experiments dd 28/29-11 and 18-12, 1985*, report IRI-131-86-08, Delft University of Technology, Delft, The Netherlands
- Van der Hagen T.H.J.J. and Van der Voet J. (1988a) *Prog. Nucl. Energy* **21**, 565
- Van der Hagen T.H.J.J., W.H.M. Nissen, Oosterkamp W.J., Van Dam H. and Hoogenboom J.E. (1988b) *Prog. Nucl. Energy* **21**, 753
- Van der Hagen T.H.J.J. (1988c) *Nucl. Technol.* **83**, 171
- Van der Hagen T.H.J.J. (1989) *Stability monitoring of a natural-circulation-cooled Boiling Water Reactor*, PhD thesis, Delft University of Technology, KEMA, Arnhem, The Netherlands, ISBN 90-353-1017-9
- Van der Hagen T.H.J.J. (1991) *Reactor noise at different water levels in the Dodewaard reactor*, report IRI-131-91-013, Delft University of Technology, Delft, The Netherlands
- Van der Hagen T.H.J.J., Van der Kaa F.J., Karuza J., Nissen W.H.M., Stekelenburg A.J.C. and Wouters J.A.A. (1992a) *Startup of the Dodewaard natural circulation boiling water reactor*, GKN-report 92-017/FY/R, GKN, Dodewaard, The Netherlands
- Van der Hagen T.H.J.J., Hoogenboom J.E. and Van Dam H. (1992b) *Nucl. Sci. Engng* **110**, 237
- Van der Hagen T.H.J.J., Van der Kaa F.J., Karuza J., Nissen W.H.M., Stekelenburg A.J.C. and Wouters J.A.A. (1993a) *Measurements at various pressures at the Dodewaard natural circulation boiling water reactor*, GKN, Dodewaard, The Netherlands, to be published
- Van der Hagen T.H.J.J., Van der Kaa F.J., Karuza J., Nissen W.H.M., Stekelenburg A.J.C. and Wouters J.A.A. (1993b) GKN, Dodewaard, The Netherlands, to be published
- Van der Hagen T.H.J.J., Van der Kaa F.J., Karuza J., Nissen W.H.M., Stekelenburg A.J.C. and Wouters J.A.A. (1993c) GKN, Dodewaard, The Netherlands, to be published
- Van der Voet J. (1989) private communication
- Verweij A.J.P. (1990) *Afmetingen en volumina van het reactorvat*, report BV 90-10, GKN, Dodewaard, The Netherlands (in Dutch)
- Wach D. (1973) *Atomwirtschaft*, 580-582
- Wach D. and Kosály G. (1974) *Atomkernenergie* **23**, 244
- Wang Y.W., King C.H. and Pei B.S. (1988) *Nucl. Technol.* **83**, 56
- Wang Y.W., Pei B.S., King C.H. and Lee S.C. (1990) *Nucl. Technol.* **89**, 217
- Weast R.C. (ed.) (1981) *Handbook of chemistry and physics*, Chemical Rubber Publishing Company, USA

- Wouters J.A.A. (1989) *Beschrijving en validatie van de VOIDLOOP van het rekenprogramma LWRSIM2.4 voor Dodewaard*, report 92220-RS 89-4033, KEMA, Arnhem, The Netherlands (in Dutch)
- Wouters J.A.A., Van der Kaa F.J. and Nissen W.H.M. (1992a) proc. of the specialists' meeting on *In-core instrumentation and reactor assessment*, 1-4 October, 1991, Pittsburg, USA, OECD, Paris, France
- Wouters J.A.A., Van der Kaa F.J., Oppentocht P. and Nissen W.H.M. (1992b) *Data and analysis of two identical water level experiments at the Dodewaard natural circulation BWR*, report 14573-TFO 92-3012, KEMA, Arnhem, The Netherlands
- Wouters J.A.A., Oppentocht P., Van der Kaa F.J. and Nissen W.H.M. (1992c) *The effect of water level on the behavior of the Dodewaard natural-circulation BWR*, proc. of the *Int. conference on the Design and Safety of Advanced Nuclear Power Plants (ANP'92)*, 25-29 October, 1992, Tokyo, Japan
- Wouters J.A.A. (1992d) *Prognose flowverdeling Dodewaard cyclus 23*, note 1473-TFO 92-1150, KEMA, Arnhem, The Netherlands (in Dutch)
- Wu S.R., Yao M.S., Wang D.Z., Hofer K. and Knogliner E. (1988) *Experimental Heat Transfer, Fluid Mechanics, and Thermodynamics*, 1120
- Yokobori S., Abe N., Nagasaka H. and Tsunoyama S. (1992) proc. of *NURETH-5, 5th International topical meeting on reactor thermal hydraulics*, 21-24 September, 1992, Salt Lake City, UT, USA
- Zemansky M.W. (1968) *Heat and thermodynamics*, McGraw-Hill Kogakusha, Tokyo



Dankwoord

Velen hebben op een of andere manier bijgedragen aan het totstandkomen van dit werk. Al deze mensen wil ik graag hartelijk bedanken. In het bijzonder noem ik:

- Prof.dr.ir. H. van Dam, voor de mogelijkheid om het werk te verrichten en de uitgebreide opleiding te volgen;
- Dr.ir. Eduard Hoogenboom, voor het verschaffen van de nodige hulpmiddelen op allerlei gebieden en voor de geboden degelijke training;
- Dr.ir. Tim van der Hagen voor de begeleiding, het geven van de vrijheid om het onderzoek zelf in te vullen, de nuttige tips en discussies en het gezelschap tijdens de soms lange (nachtelijke) meetsessies in Dodewaard;
- Jelle Schut en Dick de Haas voor de goede zorgen en de *werelddetector* resp. *wereldschakelingen* (Nobelprijs volgt wellicht nog);
- Ronald Otte en Addy Hersman voor het werk aan de ruisanalyse- en visualisatieprogrammatuur en voor het opknappen van de vele klusjes;
- De andere *OPA's*: ir. Ruud van de Graaf, ir. Ard-Jan de Jong en drs. Jan Keijzer voor de discussies en de nodige afleiding;
- Alle andere leden van de afdeling voor de prettige werksfeer en de vele activiteiten;
- Prof.dr.ir. H.E.A. van den Akker voor het ter beschikking stellen van de rekenfaciliteiten van het Kramers Laboratorium voor Fysische Technologie en voor de supervisie tijdens het in hoofdstuk 3 beschreven onderzoek;
- Ir. P.J. van der Hulst, J. Karuza, ir. Jaap van der Voet en Wim Nissen van GKN voor de mogelijkheid om metingen te verrichten aan de unieke Dodewaard-reactor en voor het vrijmaken van tijd in deze drukke periode om aandacht te schenken aan het onderzoek. Wim wordt zeer bedankt voor het uitvoeren van de talloze verzoekjes die vanuit het IRI bij GKN werden gedeponneerd en voor de inspanningen met betrekking tot de metingen;
- Ir. Jacorien Wouters, Freek van der Kaa en drs. Dante Killian van KEMA voor de prettige samenwerking in het meetteam.

Tenslotte wil ik drie mensen bedanken, die het door mijn werkzaamheden soms zwaar te verduren hebben gehad: Wendy Karlas voor de trouwe steun en mijn ouders voor hun voortdurende interesse in mijn werk en de liefdevolle, brede en dikke basis die ze mij hebben gegeven.



Curriculum vitae

- 25 May, 1967 : born at Bergen op Zoom, The Netherlands
- 1979-1985 : high school *Rijksscholengemeenschap* at Bergen op Zoom (Atheneum)
- Sept. 1985-Nov. 1989 : MSc study: applied physics at the Delft University of Technology
MSc topic: a computer simulator for a pumped gaseous core fission reactor; performed at the Department of Reactor Physics of Prof.Dr.Ir. H. van Dam, Interfaculty Reactor Institute, Delft University of Technology
- Dec. 1989-Dec. 1993 : PhD study: statics and dynamics of natural circulation cooled boiling water reactors; performed at the above-mentioned department
- Dec. 1993- : post-doc at the above-mentioned department